Design Optimization and Performance Improvement of Synchronous Reluctance Machines

by

Indula Prasad Abeyrathne Hunuhene Gedara

A thesis submitted to the Faculty of Graduate Studies of
The University of Manitoba
in partial fulfillment of the requirements for the degree of

MASTER OF SCIENCE

Department of Electrical and Computer Engineering
University of Manitoba
Winnipeg.

Abstract

The performance capability of a four pole Synchronous Reluctance Machine (SynRM) is improved using an optimized coordinate based four flux barrier hyperbolic rotor structure. Firstly, a study is conducted to compare and improve the operating performance of 36 slot four-pole SynRMs optimally designed based on three distinct Objective Functions (OFs) for (i) torque ripple minimization (RM), (ii) saliency ratio maximization (SM), and (iii) combined objective function (COF) optimization to simultaneously minimize the torque ripple and maximize the saliency ratio while supporting the required torque. For the optimized SynRMs, a normal round rotor and a rotor with a cut-off are used in the Finite Element (FE)-based rotor design optimization, while the stators are identically designed using classical electric and magnetic loading principles. The SynRMs' dimensions and efficiencies are based on IEC-90S frame size limitations and IE3 efficiency standards, respectively. Secondly, two additional SynRMs with 24 slots and 48 slots are considered with normal and cut-off rotors. Four new SynRMs are optimized using appropriate COFs to minimize the torque ripple and maximize the saliency ratio of the machines while also supporting the desired developed torque. Performance of each optimized SynRM is compared to introduce a final design. Finally to further improve performance capabilities such as developed torque, power factor and wide speed range, addition of low-cost ferrite magnet is considered along q-axis. A different COF is used to maximize the developed torque and reduce torque ripple simultaneously for the design optimization of PM assisted SynRMs (PMaSynRMs). A comparative electromagnetic study and mechanical stress and deformation analysis are carried out to predict the performance capabilities and operating limits of the designed SynRM and PMaSynRMs. The optimally designed SynRM and PMaSynRM are fabricated and tested to verify the theoretical expectations.

Use of Copyrighted Material

The author would like to acknowledge the use of the following IEEE papers in preparation of this thesis.

© 2018 IEEE. Reprinted, with permission, from I. P. Abeyrathne, M. S. Toulabi and S. Filizadeh, "A Comparative Study of Optimally Designed Synchronous Reluctance Machines," *International Conference on Electrical Machines (ICEM)*, Alexandroupoli, 2018,

© 2018 IEEE. Reprinted, with permission, from I. P. Abeyrathne, M. S. Toulabi and S. Filizadeh, "Design Optimization and Performance Prediction of Synchronous Reluctance Motors," *International Conference on Electrical Machines and Systems (ICEMS)*, 2018.

In reference to IEEE copyrighted material which is used with permission in this thesis, the IEEE does not endorse any of University of Manitoba's products or services. Internal or personal use of this material is permitted. If interested in reprinting/republishing IEEE copyrighted material for advertising or promotional purposes or for creating new collective works for resale or redistribution, please go to http://www.ieee.org/publications_standards/publications/rights/rights_link.html to learn how to obtain a License from RightsLink.

Acknowledgement

This thesis becomes a reality with the kind guidance and immense support of many individuals and I would like to show my deepest gratitude to each one of them.

First and foremost I would like to express my sincere gratitude to my supervisor Prof. Shaahin Filizadeh for accepting me as a student and his continuous guidance and support throughout the research.

On a sincere note, I would also like to express my equal gratitude to Dr. Mohammad Sedigh Toulabi for his tremendous guidance and support from the inception. I`ve learnt a lot from him both to my academic and personal lives.

I would also extend my gratitude to the examination committee consisting Dr. A. Gole and Dr. A. Rajapakse for spending time to review my thesis.

I would also like to acknowledge the support provided by academic and non-academic staff of Department of Electrical and Computer Engineering, all the colleagues and friends especially Mr. Cory Smit for helping me during the fabrication process and my friend Mr. Gayan Watthewaduge for his valuable support. Furthermore I would also like to express my gratitude to the Faculty of Graduate Studies, University of Manitoba and Natural Science and Engineering Research Council (NSERC) of Canada for providing me financial support.

Last but not least, I would like to complement each and every person who shared their knowledge and experience with me during this endeavor.

In dedication to

My Loving Wife and Parents,

Brother,

All My Teachers

And Friends

Contents

Front Matter

Abstract i

Copyright Forms ii

Acknowledgement iii

Contents v

List of Tables viii

List of Figures ix

List of Abbreviations xiii

Nomenclature xv

1 : Introduction 1

1.1 Background and Thesis Motivations 1

1.2 Thesis Outline 4

2 : Operating Principles and Characteristics of a SynRM 6

2.1 Reluctance and Motion Theory 6

2.2 Stator Structure, Number of Poles, and Winding Layout 7

2.3 Rotor Structure 9

2.4 Modelling of SynRM in d-q Reference Frame 11

2.5 Advantages and Challenges in Using SynRMs 15

2.6 Summary 17

3 : Optimization for a 36 Slot 4 Pole Synchronous Reluctance Machine 18

3.1 Design Specifications and Parameters 18

3.2 Stator Design 19

3.3 Rotor Design and Design Variables 27

3.4 Objective Functions (OFs) 32

3.5 Selecting Candidates, Related Design Variables Dimensions, and Machines Structures 34

3.6 Finite Element (FE) Based Comparative Study 37

3.6.1 Saliency Ratio 38

3.6.2 Torque Ripple 39
3.6.3 Maximum Output Power 40
3.6.4 Power Factor and Efficiency 43
3.7 Summary 44
4 : Performance Prediction of SynRM with Various SPP Values 46
4.1 Combined Objective Function Based Candidates 46
4.2 SynRMs` Dimensions and Structures 49
4.3 Finite Element (FE) Based Comparative Study 51
4.3.1 Inductance Analysis and Torque Profiles 51
4.3.2 Air-gap Flux Density and Harmonic Analysis 53
4.3.3 Maximum Output Power 54
4.3.4 Core and Copper Losses 55
4.3.5 Efficiencies at Maximum Developed Powers 56
4.3.6 Power Factor Values at Maximum Output Powers 56
4.4 Mechanical Considerations of the Finally Selected SynRM 57
4.5 Summary 58
5 : Permanent Magnet-Assisted Synchronous Reluctance Machines 60
5.1 Theory, Advantages and Challenges 60
5.2 Proposing Methodology to Obtain Optimal Magnet Dimensions 63
5.2.1 Non-Optimized PMaSynRM 63
5.2.2 Model for Optimization 65
5.2.3 Optimized PMaSynRMs 66
5.3 Finite Element (FE) Based Comparative Study of SynRM and PMaSynRMs 69
5.3.1 Maximum Output Power 69
5.3.2 Efficiencies at Maximum Output Powers 70
5.3.3 Power Factors at Maximum Output Powers 71
5.3.4 Saliency Ratio and Torque Ripple 72

5.4 Mechanical Considerations of the Finally Selected PMaSynRM 73
5.5 Summary 75
6 : Machine Fabrication and Experimental Analysis 77
6.1 Stator, Rotor, and Fabricated SynRM and PMaSynRM 77
6.1.1 Performance Sensitivity towards a Manufacturing Error 78
6.2 Experimental Test Rig 79
6.2.1 Back-EMF Analysis 80
6.3 Field Oriented Control of SynRM and PMaSynRM 81
6.3.1 Encoder Calibration 84
6.3.2 PI Controller Tuning 85
6.3.3 Starting, Speed Transition and Steady State Performance of the Closed Loop Control System 85
6.4 Experimental Analysis and Evaluation 88
6.4.1 Maximum Output Power 88
6.4.2 Efficiencies at Maximum Output Powers 89
6.4.3 Power Factors at Maximum Output Powers 90
6.5 Summary 91
7 : Contributions, Conclusions and Future Work 92
7.1 Contributions and Conclusions 92
7.2 Limitations and Future Work 95
7.3 Publications 96
References 97
Appendix A 108

List of Tables

Table 3-1: Design parameters of the SynRM. 18

Table 3-2 : Calculated Stator dimensions and winding parameters. 27

Table 3-3 : Design variables ranges. 34

Table 3-4 : Optimized design variable. 35

Table 3-5 : Operating properties of the selected SynRMs. 37

Table 3-6 : I_{pk} and θ variations versus speed changes. 41

Table 4-1 : Optimized design variables. 50

Table 4-2 : Inductances and saliency ratios of the SynRMs. 51

Table 5-1 : Operating characteristics of PMaSynRM-1 at rated speed. 64

Table 5-2 : Magnet length ranges. 66

Table 5-3 : Design variables and parameters of optimized PMaSynRMs. 68

Table 6-1 : Tuned gain values of PI controllers. 85

List of Figures

Figure 1-1 : (a) Axially laminated anisotropic (ALA) rotor, (b) Transversally laminated anisotropic (TLA) rotor. 3

Figure 2-1 : Excreted force on (a) isotropic (b) anisotropic objects in a constant field flux. 7

Figure 2-2 : Stator structure and the distributed winding arrangement for a 36-slot four-pole SynRM. 9

Figure 2-3 : One quarter of a 36-slot four-pole SynRM with a (a) normal rotor and (b) cut-off rotor. 11

Figure 2-4 : Reference frame transformation. 11

Figure 3-1 : Stator dimensions. 22

Figure 3-2 : Voltage-current phasor vector diagram for a SynRM. 26

Figure 3-3 : SynRM's rotor structure (a) normal rotor and (b) cut off rotor. 28

Figure 3-4 : Rotor structure, design variables, and important coordinates. 29

Figure 3-5 : Coordinates of the 1st barrier fillet. 31

Figure 3-6 : Saliency ratio (ξ), average torque (T_{avg}), and torque ripple (T_{rip}) variations at rated operating point for the generated solutions in (a) RM (normal rotor), (b) SM (normal rotor), (c) COF (normal rotor), (d) RM (cut off rotor), (e) SM (cut off rotor), (f) COF (cut off rotor). 35

Figure 3-7 : The structure, flux lines and flux density distribution in rated operating condition for (a) RM-normal rotor, (b) SM-normal rotor, (c) COF-normal rotor, (d) RM-cut off rotor, (b) SM-cut off rotor, (f) COF-cut off rotor, and (g) Non-optimized preliminary designed SynRMs. 36

Figure 3-8 : Saliency ratio evaluation with respect to I_{pk} and θ variations for (a) RM-normal rotor (b) SM-normal rotor, (c) COF-normal rotor, (d) RM-cut off rotor, (e) SM-cut off rotor, (f) COF-cut off rotor, and (g) Non-optimized preliminary designed SynRMs. 38

Figure 3-9 : Torque ripple evaluation with respect to I_{pk} and θ variations for (a) RM-normal rotor (b) SM-normal rotor, (c) COF-normal rotor, (d) RM-cut off rotor, (e) SM-cut off rotor, (f) COF-cut off rotor, and (g) Non-optimized preliminary designed SynRMs. 40

Figure 3-10 : (a) Average torque and (b) maximum developed power comparison. 42

Figure 3-11 : (a) Power factor variations in the maximum developed powers (b) efficiency versus speed profiles in the maximum developed powers. 43

Figure 4-1 : Saliency ratio (ξ), average torque (T_{avg}), and torque ripple (T_{rip}) variations at rated operating point for the generated solutions in (a) normal rotor (SPP=2), (b) cut off rotor (SPP=2), (c) normal rotor (SPP=3), (d) cut off rotor (SPP=3), (e) normal rotor (SPP=4) and (f) cut off rotor (SPP = 4). 48

Figure 4-2 : SynRM structures for (a) normal rotor (SPP=2), (b) cut off rotor (SPP=2), (c) normal rotor (SPP=3), (d) cut off rotor (SPP=3), (e) normal rotor (SPP = 4), and (f) cut off rotor (SPP=4). 50

Figure 4-3 : Torque profile versus rotor position in rated current for (a) SPP=2 rotor structures, (b) SPP=3 rotor structures, and (c) SPP=4 rotor structures. 52

Figure 4-4 : $B_{air\text{-}gap}$ versus rotor position in rated conditions for (a) SPP=2 rotor structures, (b) SPP=3 rotor structures, and (c) SPP=4 rotor structures. 53

Figure 4-5 : (a) Average torque and (b) maximum developed power comparison. 55

Figure 4-6 : Core losses versus speed in the maximum developed powers. 55
Figure 4-7 : Efficiency versus speed in maximum developed powers. 56
Figure 4-8 : Power factor versus speed in maximum developed powers. 57
Figure 4-9 : Exaggerated view (×1800) of (a) deformation and (b) von-Mises stress distribution for the final design in 2700 rpm. 58
Figure 5-1 : Voltage-current vector diagram of a PMaSynRM. 61
Figure 5-2 : The structure of a non-optimized PMaSynRM (PMaSynRM-1). 64
Figure 5-3 : Torque profiles of optimized SynRM and PMaSynRM-1 versus rotor position. 64
Figure 5-4 : Optimized PMaSynRM's structure including the design variables. 65
Figure 5-5: Saliency ratio, torque ripple, and average developed torque of the generated solutions in the rated operating point. 67
Figure 5-6 : Structure of the optimized PMaSynRMs, (a) PMaSynRM-2, and (b) PMaSynRM-3. 67
Figure 5-7 : Torque profiles of PMaSynRM-2 and PMaSynRM-3 versus rotor position. 68
Figure 5-8 : (a) Average torque and (b) maximum developed power comparison. 69
Figure 5-9 : Efficiency comparison in a wide speed range. 70
Figure 5-10 : Power factor comparison in a wide speed range. 71
Figure 5-11 : Saliency ratio and torque ripple comparison, (a) R_{sal}, and (b) R_{rip}. 72
Figure 5-12 : Maximum Von-Mises stress and deformation analysis versus speed changes for the designed SynRM and PMaSynRM-2. 74
Figure 5-13 : Exaggerated mechanical stress and deformation distribution, (a) Von-Mises stress-SynRM, (b) Deformation-SynRM, (c) Von-Mises stress-PMaSynRM-2, and (d) Deformation-PMaSynRM-2. 75

Figure 6-1 : Machines' parts, (a) Wound stator, (b) SynRM's rotor, and (c) PMaSynRM-2's rotor. 78
Figure 6-2 : Average developed torque, saliency ratio, and power factor variations versus air-gap length changes. 79
Figure 6-3 : Experimental test rig 80
Figure 6-4 : Back-EMF voltage waveform for PMaSynRM-2 at 900 rpm..... 80
Figure 6-5 : Variable frequency motor drives classification. 82
Figure 6-6 : FOC of SynRM with decoupled current controllers. 83
Figure 6-7 : Rotor position after calibration. 84
Figure 6-8 : PMaSynRM-2 starting (a) speed response, and (b) phase currents. 86
Figure 6-9 : Speed transition of PMaSynRM-2 from 450 rpm to 600 rpm under full load condition. 87
Figure 6-10 : PMaSynRM-2 steady state variations of (a) speed, (b) i_d and i_q and, (c) V_d and V_q at the rated operation. 87
Figure 6-11 : Output power capabilities for the designed SynRM and PMaSynRM-2 88
Figure 6-12 : Efficiency evaluations for (a) SynRM and (b) PMaSynRM-2. 90
Figure 6-13 : Power factor variations for designed SynRM and PMaSynRM-2. 90

List of Abbreviations

ALA	Axially Laminated Anisotropic
AWG	American Wire Gauge
BEMF	Back Electromotive Force
BLDCM	Brushless DC Machine
COF	Combined Objective Function
CPR	Counts per Revolution
DTC-FVM	Direct Torque Control - Field Vector Modulation
DTC-SVM	Direct Torque Control - Space Vector Modulation
FE	Finite Element
FEA	Finite Element Analysis
FFT	Fast Fourier Transform
FOC	Field Oriented Control
FW	Field Weakening
GA	Genetic Algorithm
GTAI	Giga-Transceiver Analogue Input Card
GTDI	Giga-Transceiver Digital Input Card
GTDO	Giga-Transceiver Digital Output Card
IEC	International Electromechanical Commission
IM	Induction Machine
IPMSM	Interior Permanent Magnet Synchronous Machine
MMF	Magneto Motive Force
MPF	Maximum Power Factor

NdFeB	Neodymium Iron Boron
OF	Objective Function
PI	Proportional Integral
PM	Permanent Magnet
PMaSynRM	Permanent Magnet Assisted Synchronous Reluctance Machine
PMSM	Permanent Magnet Synchronous Machine
PWM	Pulse Width Modulation
RM	Ripple Minimization
RTDS	Real Time Digital Simulator
SM	Saliency Maximization
SPP	Slots per Pole per Phase
SRM	Switched Reluctance Motor
SynRM	Synchronous Reluctance Machine
THD	Total Harmonic Distortion
TLA	Transversally Laminated Anisotropic
VCLMT	Voltage Current Limited Maximum Torque

Nomenclature

B_{1dm}	d-axis air gap flux density	(T)
$B_{1g\text{-}max}$	Maximum air gap flux density	(T)
b_{s1}, b_{s2}	Inner and outer slot widths	(mm)
b_{ss}, b_{ts}	Stator slot opening and stator tooth width	(mm)
D_r	Rotor diameter	(mm)
d^r, q^r	Rotor reference frame d- and q- axes	
d^s, q^s	Stator reference frame d- and q- axes	
g	Air-gap length	(mm)
h_s, h_{ss}	Stator slot and back iron heights	(mm)
h_{s1}, h_{s2}	Tooth tip thickness and height	(mm)
$i_d{}^r$, $i_q{}^r$	d- and q- axis currents in rotor reference frame	(A)
$i_d{}^s$, $i_q{}^s$	d- and q- axis currents in stator reference frame	(A)
i_{dm}, i_{qm}	d- and q-axis magnetizing currents	(A)
I_{pk}	Peak stator current	(A)
k	d-axis barrier angle control parameter	
k_c, k_s	Carter and saturation coefficients	
kd_{m1}	Stator d-axis magnetizing inductance ratio	
kq_{m1}	Stator q-axis magnetizing inductance ratio	
kw_1	Fundamental winding factor	
k_{wq}	q-axis insulation ratio	
L	Stator stack length	(mm)

$L_{aa}(\theta_r)$	Self-inductance of phase A	(H)
$L_{ab}(\theta_r)$	Mutual inductance between phase A and phase B	(H)
$L_{ac}(\theta_r)$	Mutual inductance between phase A and phase C	(H)
$L_{bb}(\theta_r)$	Self-inductance of phase B	(H)
$L_{ac}(\theta_r)$	Mutual inductance between phase B and phase C	(H)
$L_{cc}(\theta_r)$	Self-inductance of phase C	(H)
L_d, L_q	Rotor d- and q-axis inductances	(H)
L_m	Magnetizing inductance	(H)
m	Rotor d-axis barrier slope	
n_s	Number of turns per slot	
P	Pole pair number	
P_{cu}	Copper losses	(W)
P_{core}	Core loss	(W)
P_{out}	Output power	(W)
P_n	q-axis interception coordinates of n^{th} barrier	
q	Number of slots per pole per phase	
R_0	Effective rotor radius	(mm)
R_s	Per phase resistance	(Ω)
S_{nd}, S_{nq}	Rotor d- and q- axis n^{th} flux carrier width	(mm)
T_{avg}	Average torque	(Nm)
T_{max}	Maximum torque	(Nm)
T_{min}	Minimum torque	(Nm)
T_{rip}	Torque ripple	

V_{dm}, V_{qm}	Stator d- and q- axis magnetizing voltages	(V)
V_{pk}	Rated phase voltage (peak)	(V)
W_{nd}, W_{nq}	Rotor d- and q- axis n^{th} flux barrier width	(mm)
β	Rotor slot pitch controller angle	(deg)
γ	Flux barrier angle	(deg)
δ	Power factor angle	(deg)
θ	Stator current angle with respect to q-axis	(deg)
λ_a	Phase A flux linkage	(Wb-turns)
λ_b	Phase B flux linkage	(Wb-turns)
λ_c	Phase C flux linkage	(Wb-turns)
λ_d^r, λ_q^r	d- and q- axis flux linkages in rotor reference frame	(Wb-turns)
λ_d^s, λ_q^s	d- and q- axis flux linkages in stator reference frame	(Wb-turns)
μ_0	Air permeability	(H/m)
ξ	Saliency ratio	
τ, τ_s	Stator pole pitch and stator slot pitch	(mm)
ω_b	Rated electrical frequency	(rad/s)

Chapter 1

Introduction

In this chapter, the historical background and structural characteristics of Synchronous Reluctance Machines (SynRMs) accompanied with the advantages and motivations to use these machines in industrial applications are discussed.

1.1 Background and Thesis Motivations

Due to the unexpected rise in the price of rare earth magnets, e.g., neodymium iron boron (NdFeB), in early 2010 to mid-2011 [1], industries and research facilities started to further look for alternative Permanent Magnet (PM)-free electric machinery solutions to replace PM machines such as Permanent Magnet Synchronous Machines (PMSMs) and Brushless DC Machines (BLDCMs). Accordingly, PM-free machines including Synchronous Reluctance Machines (SynRMs) or inexpensive ferrite magnet-assisted machines have been widely investigated as possible competitive candidates. Fast development of power electronic controllers, sophisticated machine design optimization techniques, and reliable electromagnetic simulation software have been the principal motivations for the renewed attention given to SynRMs in recent years.

The concept of reluctance torque development dates back to 1913 and soon after the d-q reference frame theory was introduced for a salient pole synchronous machine by Blondel [2]. This d-q reference frame concept was well supported by Doherty and Nickel [3] who showed the operation of a salient pole synchronous machine in the absence of a field winding on its rotor in 1926. However, the first recorded attempt for designing and performance analysis of a purely

reluctance based motor was done by J. K. Kostko in 1923 [4]. His motor was named a polyphase reaction synchronous motor at that time and later called a SynRM. Kostko also recognized that having a larger saliency ratio is a necessity to achieve improved performance indicators such as higher power factor and efficiency. The presented rotor was broken into multiple sections and the insulation layers were introduced in between the layers to support a high saliency ratio characteristic for the designed SynRM. The rotor structure was called a Transversally Laminated Anisotropic (TLA) rotor since the punched laminations were stacked axially. Although SynRMs showed a competitive edge in theory over existing motor technologies, optimal placement of the insulation (flux) barriers was impractical due to the high electromagnetic nonlinearities of the machine and lack of a means to precisely define the flux barrier arrangements and sizes. As a result, during the first half of 20^{th} century, SynRMs were not chosen in electromechanical energy conversion systems as their power factor and developed power capabilities were still not on par with their DC and induction machine (IM) counterparts due to lack of a well-designed rotor structure, thus eventually lacking high enough saliency ratio and desirable torque capability characteristics. However, four decades after proposing the TLA rotor structure, Axially Laminated Anisotropic (ALA) rotor structure was introduced in 1966 based on the same concept but with a different approach to obtain a higher saliency ratio [5]. A large number of steel laminations were stacked axially with the insulating layers in between laminations to form the rotor of the machine. The ALA rotor structure was capable of supporting a significantly higher saliency ratio for the designed SynRM compared to a SynRM with a TLA rotor structure; however, due to the manufacturing complexities and higher iron losses, an ALA rotor structure has never been the most favorable option in SynRM applications. Figure 1-1(a) shows an ALA rotor and Figure 1-1(b) shows a TLA rotor. On the other hand, the stator of a SynRM is exactly

identical to that of an IM and the dimensions and characteristics of the stator, including the winding arrangements, could be defined using conventional magnetic and electric loading principles [6].

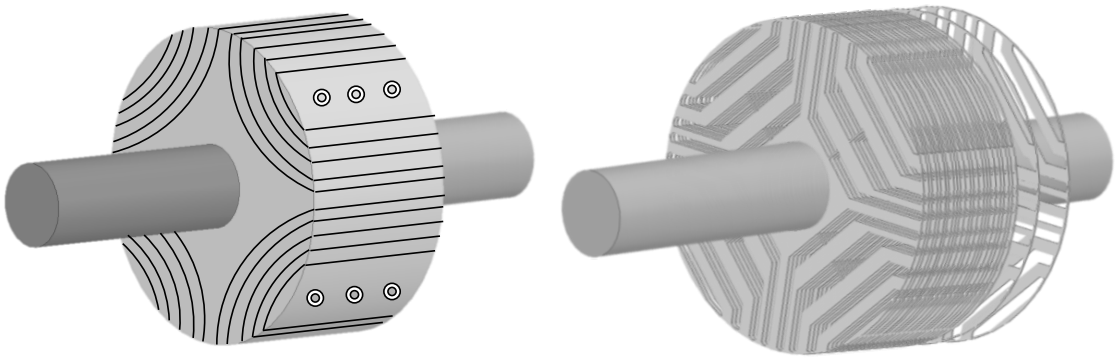

(a) (b)

Figure 1-1: (a) Axially laminated anisotropic (ALA) rotor, (b) Transversally laminated anisotropic (TLA) rotor (adopted from [7]).

Due to the advancements in optimization techniques and computing technology, Finite Element (FE)-based design optimization has become a favorable method for accurate design optimization and performance improvement of electric machines [8] especially for the ones possessing a highly anisotropic rotor structure such as SynRMs [9], [10]. Rotor design optimization and performance improvement of SynRMs may focus on either a single performance indicator, e.g., torque ripple, saliency ratio, and developed torque, or a combination of two or more [11], [12]. Only considering one specific performance indicator in design steps may negatively affect the machine's performance from other perspectives. For instance, minimizing the torque ripple will reduce mechanical fatigue on shaft and bearings but does not necessarily contribute to the saliency ratio or developed torque betterment. Although the complexity of optimization grows with the addition of more performance indicators and design variables, the optimized machine may fulfill competing requirements at a same time. However, a compromise between different performance indicators should always be considered.

In this thesis, various design variables including flux barrier and carrier widths and flux barrier angles are considered during the FE-based design optimization process to find the optimal d- and q-axis flux paths for improving the performance of SynRMs with the TLA rotor structure. The optimized SynRM is meant to simultaneously possess low torque ripple and high saliency ratio values while the desired developed torque is always considered during optimization. To broaden the diversity of the analysis, a normal round rotor and a rotor with a cut-off are used for four pole TLA SynRMs with stators of different slot numbers to support various Slot per Pole per Phase (SPP) ratios of 2 (24 slots), 3 (36 slots), and 4 (48 slots). By adding ferrite PMs into the rotor of the best performing SynRM a further enhancement in the performance indices such as power factor, efficiency, and constant-power speed range are fulfilled by the PM-Assisted SynRM (PMaSynRM) alternative. It is worth noting that the dimensions of the PMs are also determined by conducting an FE-based design optimization considering favorable performance criteria such as high developed torque and low torque ripple at a same time. The mechanical properties of the designed rotors are simulated to prevent any potential fracture or deformation in the tangential and radial ribs prior to fabrication. Experimental results are also included to verify the simulation expectations.

1.2 Thesis Outline

Chapter 2 focuses on the principles of operation and understanding of SynRMs. Selection of the slot-pole combination and rotor structure design variables are also properly reasoned out in this chapter.

The design steps for stator and rotor of a 36-slot, four-pole SynRM are described to fulfill certain design specifications and desired requirements by introducing proper design variables in Chapter 3. Also different Objective Functions (OFs) for saliency ratio maximization, torque

ripple minimization, and a Combined Objective Function (COF) optimization are introduced for the rotor design optimization and performance comparison purposes.

In Chapter 4, and to broaden the scope of the analysis, separate design optimizations are conducted for SynRMs of different SPPs by means of a COF optimization. Mechanical stress and deformation analyses are performed for the selected best-performing SynRM candidate to ensure that the rotor of the machine can withstand the centrifugal forces at its expected maximum operating speed.

In Chapter 5, advantages and challenges of PMaSynRM over SynRM are discussed. The discussion is limited to low-cost ferrite magnet addition as it can be a viable alternative to rare earth magnets with high price fluctuations. The optimal placement of the ferrite magnets in the flux barriers of the selected best performing SynRM form Chapter 4 is fulfilled in detail incorporating the magnet dimension design variables into the already designed co-ordinate based rotor structure. Eventually, electromagnetic performance comparison between PMaSynRM versus SynRM is conducted and the rotor stress and deformation analyses of the PMaSynRM are conducted prior to fabricating a full-scale machine.

The machine fabrication steps and preparation of a full-scale test rig are discussed in Chapter 6. Field-Oriented Control (FOC) technique and experimental validation in wide speed range performance of both SynRM and PMaSynRM are also discussed in Chapter 6.

Lastly, the thesis is concluded with conclusions and suggested future directions to validate and further improve the contribution of the conducted research.

Chapter 2

Operating Principles and Characteristics of a SynRM

The operating principles of SynRMs, winding patterns, number of poles, and abc and d-q steady state models are introduced in this chapter, while the advantages and challenges in using SynRMs are highlighted at the end of the chapter.

2.1 Reluctance and Motion Theory

When the current circulates in a loop, there will be resistance to its flow and as such current tends to flow through the path of least resistance. Similarly in a magnetic circuit, magnetic flux tends to mainly pass through the minimum reluctance path, i.e., a magnetically conductive axis (commonly referred to as d-axis). Figure 2-1 shows two magnetic objects placed in a constant field flux (Ψ). Object (a) is round in shape and its reluctances in each direction is the same. Object (a) is already in a magnetically neutral position meaning that the d-axis is already aligned with the field flux (Ψ) direction, hence it is called an isotropic object. On the other hand, object (b) has different reluctances along the d- and q-axes and as such is called an anisotropic object. Since the d-axis (the axis with less reluctance) is not aligned initially with the field flux (Ψ) direction, there will be an exerted force couple (F) on this object to align its d-axis with the field flux (Ψ) direction to minimize the total reluctance. This force couple leads to creation of torque.

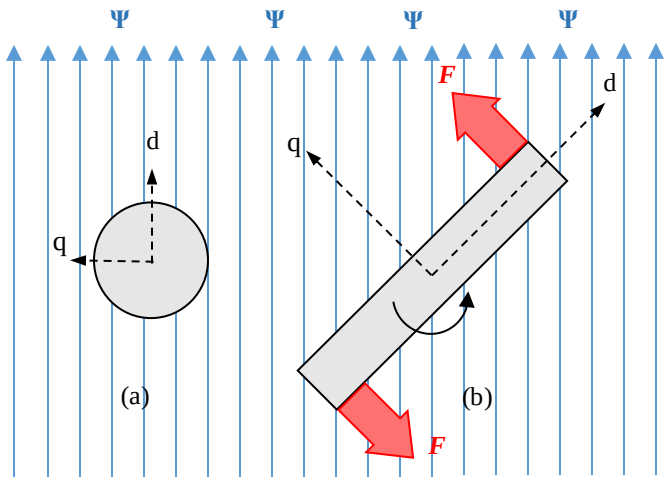

Figure 2-1: Excreted force on (a) isotropic (b) anisotropic objects in a constant field flux.

The same reluctance theory can be applied to the synchronous reluctance motor as well. When the currents exciting the stator produce a sinusoidally varying magnetic field flux in the air-gap, the anisotropic rotor will rotate to align its d-axis with the applied field due to the torque exerted on it. The continuously rotating field of the stator will cause continuous rotation of the rotor.

2.2 Stator Structure, Number of Poles, and Winding Layout

The stator of a SynRM is identical to that of an induction machine (IM). Electric and magnetic loading principles are used for the stator design of a SynRM; however SynRMs' inherent magnetic non-linearity compared to IMs necessitates a proper technique to accurately obtain its stator's dimensions. To obtain improved torque and reduced torque ripple, the number of slots plays a major role among the stator parameters. Generally speaking, a higher slot number is preferred for low torque-ripple and good heat dissipation at the expense of a more complicated winding and structurally weaker teeth [13]. Regarding the winding arrangement, the winding pattern is correlated with the expected performance of the machine. Although some studies have

introduced concentrated winding layouts for SynRMs to increase the saliency ratio and efficiency, and reduce the copper losses by lowering the end winding length [14], it is also shown that poor power factor may eventually create higher inverter losses and decrease overall drive efficiency for SynRMs with a concentrated winding [15]. Torque ripple and iron losses could also increase due to the high harmonic content in the air-gap magneto-motive force (MMF) for a SynRM equipped with a concentrated winding. Therefore, in this thesis a conventional distributed winding layout is used to improve the average toque capability and reduce the torque ripple while supporting a promising power factor by obtaining a higher saliency ratio through proper design techniques for the rotor. As the other important consideration regarding the stator design of a SynRM, reducing the slot opening can also improve the average torque by improving the air-gap flux density waveform and its harmonic contents [16]. However, it is also shown in [16] that lowering the slot opening excessively can negatively affect the average torque due to simultaneous increment of d- and q-axis inductances. Lowering the slot opening too much may introduce complications when actually winding the stator in case the conductor size is comparatively bigger than the slot opening width. Setting a slot opening width to two times the conductor's diameter is followed in this thesis to deal with the mentioned challenges. Regarding the number of poles in a SynRM, it must be noted that the pole number increment may deteriorate the rotor performance as the increment of the radial flux eventually decreases the saliency ratio [17]. For instance, pole numbers above four is strictly discouraged in [18]. Figure 2-2 shows the stator, winding pattern, and rotor geometries of a 36-slot, four-pole SynRM. In this thesis, separately designed stator structures for 24, 36, and 48 slot, four-pole SynRMs are introduced while detailed calculations are reported for a 36-slot, four-pole SynRM example.

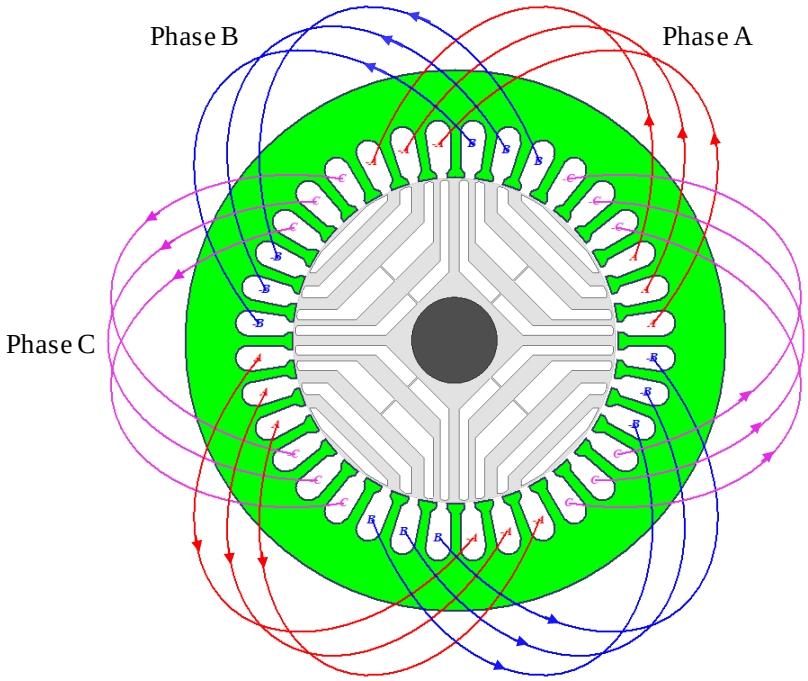

Figure 2-2: Stator structure and the distributed winding arrangement for a 36-slot, four-pole SynRM.

2.3 Rotor Structure

Rotor structure design is the most dynamic procedure in the SynRM design mainly due to the rotor's high nonlinearity. Essentially the rotor design efforts are made by taking into account the number of poles, number of flux barriers and their shapes and dimensions, and rotor type e.g., normal round rotor or a rotor with a cut off. This means that a practical rotor design for a SynRM may involve a large number of interdependent variables and as such it is quite challenging to generalize a method to analytically calculate the design variables in a straightforward way for a set of given performance criteria. Since FE-based analysis is more accurate than purely analytical methods [8], [19] the research conducted in this thesis mainly focuses on a novel coordinate based rotor structure development that can be easily incorporated into FE analysis (FEA) for possible performance improvements [9], [20] without sacrificing the calculation accuracy. FE-based design optimization and performance improvements such as

saliency ratio, average torque, torque ripple, and efficiency betterment of SynRMs have been the focus of the research reported in [21]–[27]. However, in [21] important design parameters including the rotor flux barrier angles and widths were neglected and only a parametric design of experiments was conducted to find the best possible SynRM design. In [22] and [25]–[27] saliency ratio and developed torque were ignored; in [23] saliency ratio and torque ripple were not considered, and in [24] the developed torque of the SynRM was not considered during design optimization and performance improvement. This clearly shows deficiencies in the existing research work on the SynRM design.

In order to improve the saliency ratio of the designed SynRM with a highly anisotropic rotor structure four flux barrier segments per pole are selected throughout the analysis. Although ALA rotor offers improved performance in terms of saliency ratio and power factor improvements, due to the manufacturing complexities and higher mechanical stress [13] a TLA rotor is used in this thesis. There are different types of flux barrier shapes such as circular, hyperbolic polyline (segmented), or fluid shape. Since this thesis also considers the PMaSynRM for further performance improvements, hyperbolic polyline barrier construction is considered as it offers greater flexibility when inserting the magnets.

One quarter of a SynRM with a four flux barrier TLA normal (round) rotor and a cutoff rotor structure accompanied by the d- and q-axis flux paths are shown in Figure 2-3. For the sake of rotor's mechanical rigidity, radial ribs are added and filleted flux barrier ends are considered during FE-based design optimization procedure.

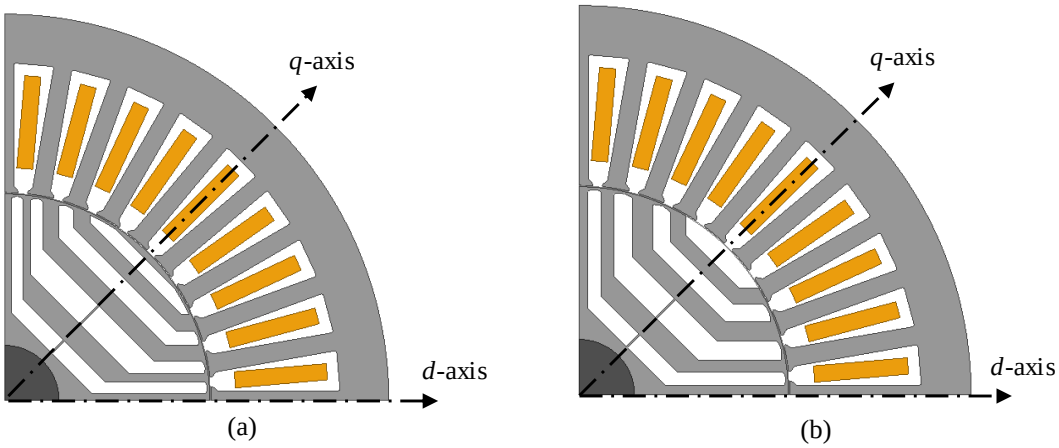

Figure 2-3: One quarter of a 36-slot, four-pole SynRM with a (a) normal rotor and (b) cut-off rotor.

2.4 Modeling of SynRM in a d-q Reference Frame

In this section, modeling of a SynRM in a d-q reference frame is described. It helps to understand the working principles and control of a SynRM from a different perspective. First, the abc stator reference frame quantities are converted to two orthogonal vectors in the same stator reference frame as any 2D vector system can be completely represented by two perpendicular vectors. Then those vectors are transformed to the rotor's d-q reference frame using the rotor position (θ_r). The mathematical relationship of the said reference frames is shown in Figure 2-4.

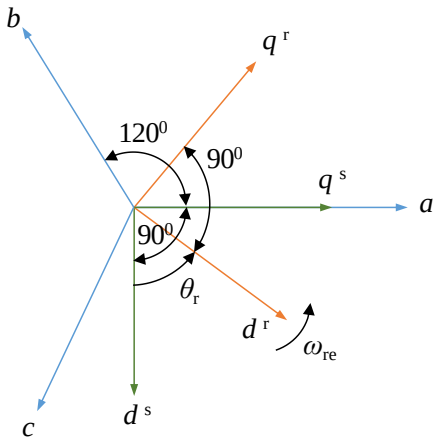

Figure 2-4 : Reference frame transformation.

For this transformation a balanced stator excitation is assumed and flux linkages in the abc domain are given in terms of self and mutual inductances according to (2.1).

$$\begin{bmatrix} \lambda_a \\ \lambda_b \\ \lambda_c \end{bmatrix} = \begin{bmatrix} L_{aa}(\theta_r) & L_{ab}(\theta_r) & L_{ac}(\theta_r) \\ L_{ba}(\theta_r) & L_{bb}(\theta_r) & L_{bc}(\theta_r) \\ L_{ca}(\theta_r) & L_{cb}(\theta_r) & L_{cc}(\theta_r) \end{bmatrix} \begin{bmatrix} i_a \\ i_b \\ i_c \end{bmatrix} \tag{2.1}$$

Self and mutual inductances can be expressed in terms of leakage inductance (L_l), and inductance coefficients (L', L'').

$$L_{aa}(\theta_r) = L_l + L'' + L'\cos(2\theta_r) \tag{2.2}$$

$$L_{ab}(\theta_r) = -0.5L'' + L'\cos(2\theta_r - 120^o) \tag{2.3}$$

$$L_{ac}(\theta_r) = -0.5L'' + L'\cos(2\theta_r + 120^o) \tag{2.4}$$

$$L_{bb}(\theta_r) = L_l + L'' + L'\cos(2\theta_r + 120^o) \tag{2.5}$$

$$L_{bc}(\theta_r) = -0.5L'' + L'\cos(2\theta_r) \tag{2.6}$$

$$L_{cc}(\theta_r) = L_l + L'' + L'\cos(2\theta_r - 120^o) \tag{2.7}$$

Parameters in the abc domain can be transformed into stator d-q reference frame by using the transformation matrix [T_{23}] given in (2.8) and inverse of [T_{23}] is denoted by [T_{32}], which can be used to convert stator d-q reference frame parameters back to the abc domain.

$$T_{23} = \begin{bmatrix} 2/3 & -1/3 & -1/3 \\ 0 & \sqrt{3}/3 & -\sqrt{3}/3 \\ 1/3 & 1/3 & 1/3 \end{bmatrix} \tag{2.8}$$

Flux linkages expressed in (2.1) can be transformed to the stator's d-q reference frame as shown in (2.9) where [$L_{abc}(\theta_r)$] is the self and mutual inductance matrix in (2.1).

$$\begin{bmatrix} \lambda_d^s \\ \lambda_q^s \\ \lambda_0^s \end{bmatrix} = T_{23} \cdot L_{abc}(\theta_r) \cdot T_{32} \begin{bmatrix} i_d^s \\ i_q^s \\ i_0^s \end{bmatrix} \tag{2.9}$$

Further simplification of $T_{23} \cdot L_{abc}(\theta_r) \cdot T_{32}$ in (2.9) yields the matrix given in (2.10).

$$T_{23}\cdot L_{abc}(\theta_r)\cdot T_{32}=\begin{bmatrix} L_l+1.5\left(L''+L'\cos(2\theta_r)\right) & 1.5L'\sin(2\theta_r) & 0 \\ 1.5L'\sin(2\theta_r) & L_l+1.5\left(L''+L'\cos(2\theta_r)\right) & 0 \\ 0 & 0 & L_l \end{bmatrix} \quad (2.10)$$

According to (2.10), the maximum self-inductance as the direct inductance (L_{sd}) occurs when (θ_r=0^0) and the minimum self-inductance as the quadrature inductance (L_{sq}) occurs when (θ_r=90^0); these are given by (2.11) and (2.12), respectively.

$$L_{sd}=1.5\left(L''+L'\right)+L_l \quad (2.11)$$

$$L_{sq}=1.5\left(L''-L'\right)+L_l \quad (2.12)$$

Under balanced conditions, zero-sequence components are all equal to zero. Hence, stator d-q flux linkage equation can be reduced as in (2.13).

$$\begin{bmatrix} \lambda_d^{\,s} \\ \lambda_q^{\,s} \end{bmatrix}=\begin{bmatrix} L_l+1.5\left(L''+L'\cos(2\theta_r)\right) & 1.5L'\sin(2\theta_r) \\ 1.5L'\sin(2\theta_r) & L_l+1.5\left(L''+L'\cos(2\theta_r)\right) \end{bmatrix}\begin{bmatrix} i_d^{\,s} \\ i_q^{\,s} \end{bmatrix} \quad (2.13)$$

Using (2.11) and (2.12), the inductance matrix in (2.13) can be expressed in terms of L_{sd} and L_{sq} as shown in (2.14).

$$L_{dq}(\theta_r)=\begin{bmatrix} 0.5\left\{(L_{sd}+L_{sq})+(L_{sd}-L_{sq})\cos(2\theta_r)\right\} & 0.5(L_{sd}-L_{sq})\sin(2\theta_r) \\ 0.5(L_{sd}-L_{sq})\sin(2\theta_r) & 0.5\left\{(L_{sd}+L_{sq})+(L_{sd}-L_{sq})\cos(2\theta_r)\right\} \end{bmatrix} \quad (2.14)$$

The flux linkage relationship given in (2.13) is derived with respect to the stator's d-q reference frame. That can be further simplified by transforming to rotor reference frame using the transformation matrix (T_{s2r}) given in (2.15) and the inverse of [T_{s2r}] is denoted by [T_{r2s}].

$$T_{s2r}=\begin{bmatrix} \cos(\theta_r) & \sin(\theta_r) \\ -\sin(\theta_r) & \cos(\theta_r) \end{bmatrix} \quad (2.15)$$

Then the flux linkage equations in the rotor reference frame can be expressed as in (2.16).

$$\begin{bmatrix} \lambda_{\mathrm{d}}{}^{\mathrm{r}} \\ \lambda_{\mathrm{q}}{}^{\mathrm{r}} \end{bmatrix} = T_{\mathrm{s2r}} \cdot L_{\mathrm{dq}}(\theta_{\mathrm{r}}) \cdot T_{\mathrm{r2s}} \begin{bmatrix} i_{\mathrm{d}}{}^{\mathrm{r}} \\ i_{\mathrm{q}}{}^{\mathrm{r}} \end{bmatrix} \tag{2.16}$$

Further simplification of $T_{\mathrm{s2r}} \cdot L_{\mathrm{dq}}(\theta_{\mathrm{r}}) \cdot T_{\mathrm{r2s}}$ in (2.16), gives an inductance matrix in terms of L_{sd} and L_{sq} as shown below.

$$L_{\mathrm{dq}}(\theta_{\mathrm{r}})^{\mathrm{r}} = \begin{bmatrix} L_{\mathrm{sd}} & 0 \\ 0 & L_{\mathrm{sq}} \end{bmatrix} \tag{2.17}$$

The co-energy of the equivalent two-phase machine is given by (2.18); note that only the final result is shown without the intermediate simplification steps.

$$\begin{aligned} W'_{\mathrm{fld}}(\theta_{\mathrm{r}}) &= \int_0^{i_{\mathrm{d}}{}^{\mathrm{s}}} \lambda_{\mathrm{d}}(i_{\mathrm{d}}{}^{\mathrm{s}\prime}, 0) di_{\mathrm{d}}{}^{\mathrm{s}\prime} + \int_0^{i_{\mathrm{q}}{}^{\mathrm{s}}} \lambda_{\mathrm{q}}(i_{\mathrm{d}}{}^{\mathrm{s}}, i_{\mathrm{q}}{}^{\mathrm{s}\prime}) di_{\mathrm{q}}{}^{\mathrm{s}\prime} \\ &= 0.25\left\{(L_{\mathrm{sd}} + L_{\mathrm{sq}}) + (L_{\mathrm{sd}} + L_{\mathrm{sq}})\cos(2\theta_{\mathrm{r}})\right\}(i_{\mathrm{d}}{}^{\mathrm{s}\,2} - i_{\mathrm{q}}{}^{\mathrm{s}\,2}) + 0.5(L_{\mathrm{sd}} + L_{\mathrm{sq}})\sin(2\theta_{\mathrm{r}}) i_{\mathrm{d}}{}^{\mathrm{s}} i_{\mathrm{q}}{}^{\mathrm{s}} \end{aligned} \tag{2.18}$$

Two-phase torque is, therefore, derived using (2.19)

$$\begin{aligned} T_{\mathrm{2ph}} &= \frac{\partial W'_{\mathrm{fld}}(\theta_{\mathrm{r}})}{\partial \theta_{\mathrm{r}}} \\ &= \frac{\partial\left[0.25\left\{(L_{\mathrm{sd}} + L_{\mathrm{sq}}) + (L_{\mathrm{sd}} + L_{\mathrm{sq}})\cos(2\theta_{\mathrm{r}})\right\}(i_{\mathrm{d}}{}^{\mathrm{s}\,2} - i_{\mathrm{q}}{}^{\mathrm{s}\,2}) + 0.5(L_{\mathrm{sd}} + L_{\mathrm{sq}})\sin(2\theta_{\mathrm{r}}) i_{\mathrm{d}}{}^{\mathrm{s}} i_{\mathrm{q}}{}^{\mathrm{s}}\right]}{\partial \theta_{\mathrm{r}}} \\ &= (L_{\mathrm{sd}} - L_{\mathrm{sq}})\left[-\sin\theta_{\mathrm{r}}\cos\theta_{\mathrm{r}}(i_{\mathrm{d}}{}^{\mathrm{s}\,2} - i_{\mathrm{q}}{}^{\mathrm{s}\,2}) + (\cos^2\theta_{\mathrm{r}} - \sin^2\theta_{\mathrm{r}}) i_{\mathrm{d}}{}^{\mathrm{s}} i_{\mathrm{q}}{}^{\mathrm{s}}\right] \\ &= (L_{\mathrm{sd}} - L_{\mathrm{sq}})\left[(i_{\mathrm{d}}{}^{\mathrm{s}}\cos\theta_{\mathrm{r}} + i_{\mathrm{q}}{}^{\mathrm{s}}\sin\theta_{\mathrm{r}})(i_{\mathrm{q}}{}^{\mathrm{s}}\cos\theta_{\mathrm{r}} - i_{\mathrm{d}}{}^{\mathrm{s}}\sin\theta_{\mathrm{r}})\right] \\ &= (L_{\mathrm{sd}} - L_{\mathrm{sq}}) i_{\mathrm{d}}{}^{\mathrm{r}} i_{\mathrm{q}}{}^{\mathrm{r}} \end{aligned} \tag{2.19}$$

It is worth noticing that stator reference frame d-q parameters can be converted to rotor reference frame using (2.15). Hence the developed torque for a 3-phase machine with P pole pairs can be expressed using (2.20).

$$T_{3ph} = \frac{3}{2} P T_{2ph} = \frac{3}{2} P (L_{sd} - L_{sq}) i_d^r i_q^r \quad (2.20)$$

2.5 Advantages and Challenges in using SynRMs

SynRMs became more popular among the other types of electric machines especially after the reported price hikes during early 2010 to mid-2011 of rare earth magnets causing degradation of the production of industry leading benchmark performer the PMSM [28]. The price of rare earth magnets was reported to increase by twenty times the usual price causing some small electric machine companies to be thrown out of the marketplace. Accordingly, industrial researchers and academic institutions were looking for possible alternatives, which do not necessarily require rare earth magnets to support a competitive performance. Since the rotor structure of a SynRM is only made out of steel without any inserted magnets, it is invulnerable to high price fluctuations of rare earth magnets [29] and also provides great mechanical rigidity [30]. In addition, the production cost of a SynRM compared to a similarly rated IM is lower due to the absence of the rotor bars or rotor winding, yet it offers higher efficiency compared to an IM [31], [33]. Moreover the efficiency gain of the multi flux barrier SynRM is said to be 1-3% over a similarly rated IM [21]. On the other hand, the power factor of a SynRM is lower by 7-8% [34], though operated at lower cost. Hence power factor improvement measures need to be considered, e.g., introducing PMs, to have a clear win against its counterparts. Compared to DC and wound rotor AC motors, SynRMs support low rotor losses [20], [35], [36] and low maintenance cost over their operating years [37]. High rotor temperatures due to the rotor losses can easily cause problems to the most vulnerable part of the motor assembly, which are bearings. Hence bearings need to be continuously inspected and changed in the electric machines that

suffer from high rotor losses. Frequent changing of the bearings can cause increased maintenance cost and more importantly frequent production shutdowns for DC and wound rotor IMs.

The magnet-free feature of SynRMs reduces the cost and most importantly avoids the demagnetization effects under impulsive overloads compared to PM motors [38]. In addition, a SynRM can be manufactured with a similar stator to an IM [21], [39], so adopting the new technology will be fast and practically feasible. When it comes to fault tolerance capability, switched reluctance motors (SRMs) are well known [40]. However, SRMs suffer from high torque ripple values and acoustic noise, which are hard to overcome. If a SynRM can be optimally designed and controlled to overcome those issues, it could be a viable alternative. A novel control method is shown in [41] to achieve a reliable fault tolerance level in a SynRM without changing the physical structure by only modifying the control algorithm. SynRMs are becoming popular for encoder less operation practices. In [42], and [43] low power SynRMs are controlled with saliency-based speed control techniques by rotor position estimation using large inductance difference between d- and q-axis.

On the other hand, SynRMs with non-optimized rotor structures can potentially have low saliency ratio values resulting low efficiencies and power factors, high harmonic content and iron losses [44], possible vibration and noise issues [45] mainly due to high torque ripple values. It is always a challenging task to develop control techniques for a SynRM in variable-speed applications as the torque and d-q axes inductances are nonlinear functions of the stator current amplitude [46].This thesis proposes a detailed investigation to mitigate most of the listed correlated disadvantages such as low saliency, low power factor, and high torque ripple of a SynRM starting from a specifically designed rotor structure for a 36-slot stator. The rotor structure offers more versatility in terms of including design parameters such as variable flux

barrier angle and variable d-axis insulation ratio to achieve more degrees of freedom to obtain an overall best design in terms of saliency ratio, average torque, and reduced torque ripple by a significant margin. To broaden the analysis further, 48-slot and 24-slot stator structures with specific rotor structures are also analyzed in terms of their COF. Low power-factor issue is also addressed by adding low-cost ferrite magnets in the q-axis while making sure other important performance indicators such as developed torque and torque ripple are maintained at a desirable level compared to the SynRM optimization. Mechanical stress and deformation analysis is also presented to verify the optimal design in terms of practicality.

2.6 Summary

The basic operating principle of a SynRM was discussed and the difference between d-q axis reluctances (inductances) were mentioned as the main characteristic of a SynRM for a continuous rotation supporting the required developed torque. Distributed winding and four-pole rotor characteristics were recommended for the design in this thesis due to the potential higher developed torque capability with lower harmonic contents in the air-gap. To broaden the analysis, various SPPs and rotor structures were shown to find a better potential design with more promising operating indicators. Torque equations of SynRMs in both abc and d-q reference frame were introduced and it was shown that the saliency ratio value or the difference between d- and q-axis inductances is the most important factor in developing a higher torque. The advantages of using SynRM in propulsion systems were described and some challenges in using these machines were discussed in further details.

Chapter 3

Optimal Design of a 36-Slot, Four-Pole Synchronous Reluctance Machine

In this chapter, sizing of a stator structure for a 1 kW, 36-slot, four-pole SynRM is presented using analytical electric and magnetic loading principles; a novel coordinate based four-flux barrier hyperbolic rotor structure construction is also presented. Proposing rotor structure is used for all optimizations and later under gone a comparative study which is conducted to compare the operating performance of optimally designed SynRMs. The optimizations are based on three distinct Objective Functions (OFs) to (i) minimize the torque ripple, (ii) maximize the saliency ratio, and (iii) simultaneously minimize the torque ripple and maximize the saliency ratio while supporting the required torque.

3.1 Design Specifications and Parameters

The ratings of the designed SynRMs and design parameters are included in Table 3-1

Table 3-1: Design parameters of the SynRM.

Parameter	**Value**	**Parameter**	**Value**
Rated power	1 kW	Power factor	0.8
Voltage (L-L)	208 V	Efficiency	85%
Rated speed	900 rpm	Air-gap (g)	0.35 mm
Slot / pole	36 / 4	Lamination	M19-29G
Desired saliency ratio	9	Carter`s coefficient (k_c)	1.23
Magnetic loading	0.85 T	Saturation coefficient (k_s)	0.4
Current density (J_c)	5 (A/mm^2)	Permeability constant (μ_0)	1.25664×10^{-6} H/m
Slot filling factor (k_{fill})	0.37	Copper resistivity ρ_{120} (@ 120^0C)	2.3×10^{-8} Ωm

In this chapter, the stator of a 36-slot, four-pole SynRMs is analytically designed based on conventional electric and magnetic loading principles and the design requirements reported in [6]. To support the maximum power factor below base speed. The IEC-90S standard frame size, IE3 efficiency standard, recommended air-gap length for a 1 kW IM, and split ratio of 0.5-0.7 are all considered during the machine design steps.

3.2 Stator Design

The methodology of accomplishing the required performance is explained and calculated step by step using a 36-slot, four-pole SynRM example. Because the calculations are purely based on analytical equations given in [6], assumptions and reasonably accurate parameter estimations need to be used. The following steps to calculate the stator dimensions are based on the required parameters and information described in Table 3-1.

SPP is given by (3.1) and has a calculated value of 3 for a three-phase, 36-slot, four-pole SynRM.

$$q = \frac{\text{slots}}{\text{poles}\times\text{phases}} \tag{3.1}$$

Fundamental winding factor (k_{w1}) is calculated by (3.2), which is equal to 0.9598 for the designed SynRM.

$$k_{w1} = \frac{\sin \pi / 6}{q \sin(\pi / 6q)} \tag{3.2}$$

For an expected air-gap of 0.35 mm and an approximated pole pitch (τ) value of 75 mm, the stator's d-axis magnetizing inductance ratio (k_{dm1}) and stator's q-axis magnetizing inductance ratio (k_{qm1}) are assigned as 0.955 and 0.055. respectively, using the graphs given in [6]. If the

saturation and stator slotting effects are ignored, k_{dm1} and k_{qm1} only depend on the τ/g and pole shoe (τ_p/g).

Leakage inductance (L_l) is assumed to be equal to the q-axis magnetizing inductance (L_{qm}). An approximate calculation for saliency ratio can be given as in (3.3) yielding a value of 9.18.

$$\left(\frac{L_d}{L_q}\right) = \frac{L_{dm} + L_l}{L_{qm} + L_l} \approx \frac{L_{dm} + L_{qm}}{2L_{qm}} \approx \frac{k_{dm1} + k_{qm1}}{2k_{qm1}} \tag{3.3}$$

where, $k_{dm1} = \dfrac{L_{dm}}{L_m}$ and $k_{qm1} = \dfrac{L_{qm}}{L_m}$

As the magnetic loading ($B_{1g\,max}$) is set to 0.85 T, the fundamental component of d- and q-axis air-gap flux densities (B_{1dm} and B_{1qm}) calculated by (3.4) and (3.5) are equal to 0.8376 T and 0.1447 T, respectively.

$$B_{1dm} = \frac{B_{1g\,max}}{\sqrt{1 + \dfrac{k^2_{qm1}}{k^2_{dm1}} \cdot \dfrac{L_d}{L_q}}} \tag{3.4}$$

$$B_{1qm} = \sqrt{B^2_{1g\,max} - B^2_{1dm}} \tag{3.5}$$

For the expected output power of 1 kW at a nominal speed of 900 rpm, the average torque is calculated by (3.6), which is equal to 10.61 Nm.

$$T_{avg} = \frac{P_{rated} \times 60}{2\pi \cdot N_{rated}} \tag{3.6}$$

The expression to calculate pole pitch (τ) as shown in (3.7) has two unknown ratios namely the pole pitch to air-gap ratio (τ/g) and the stack aspect ratio (L/τ). The reason to keep those ratios in the expression without simplifying further is to have better proportions in the actual calculated dimensions. For example, L/τ typically has a value in the range of [0.6, 3] in an IM.

τ/g and L/τ are varied in an iterative manner by looking at (3.9) to have an air-gap (g) of 0.35mm. The final values of τ/g and L/τ are 215 and 0.94, respectively, to yield a value of 75.26 mm for τ.

$$\tau = \sqrt[3]{\frac{2T_{\text{avg}} \cdot {k_{d\,\text{m1}}}^2 \cdot \mu_0 \cdot \left[\frac{\tau}{g}\right] \cdot \left[\frac{\tau}{L}\right]}{{B_{1\text{dm}}}^2 \cdot P^2 \cdot (k_{d\,\text{m1}} - k_{q\,\text{m1}}) \cdot \sqrt{\xi} \cdot k_{\text{c}} \cdot (1 + k_{\text{s}})}} \tag{3.7}$$

where $\xi = \frac{L_{\text{d}}}{L_{\text{q}}}$ and P: pole pair number

The stack length (L), g, and rotor diameter (D) are calculated using (3.8), (3.9), and (3.10), and the corresponding calculated values are equal to 70.7 mm, 0.35 mm, 95.8 mm, respectively.

$$L = \tau \cdot \frac{L}{\tau} \tag{3.8}$$

$$g = \tau \cdot \frac{g}{\tau} \tag{3.9}$$

$$D = \frac{2P\tau}{\pi} \tag{3.10}$$

So far, the basic dimensions, such as L and D, have been calculated. Stator slot parameters can be calculated now using an approach described as follows.

The d- and q-axis slot ampere-turns components are calculated using (3.11) and (3.12), which are equal to 108.197 A.turns and 324.591 A.turns, respectively.

$$n_{\text{s}} I_{\text{dm}} = \frac{B_{1\text{dm}} \pi g k_{\text{c}} (1 + k_{\text{s}})}{3\sqrt{2}\mu_0 q k_{\text{w1}} k_{\text{dm1}}} \tag{3.11}$$

$$n_{\text{s}} I_{\text{qm}} = n_{\text{s}} I_{dm} \sqrt{\frac{L_{\text{d}}}{L_{\text{q}}}} \tag{3.12}$$

The total slot ampere-turns component is calculated using (3.13), which is equal to 342.149 A.turns.

$$n_s I_m = \sqrt{\left(n_s I_{dm}\right)^2 + \left(n_s I_{qm}\right)^2} \tag{3.13}$$

In order to calculate the useful (effective) slot area (A_s) by (3.14), it is important to assign current density (J_c) and slot filling factor (k_{fill}) as mentioned in Table 3-1 and also consider the practical aspects such as manufacturing. The effective slot area is consequently calculated as 183.11 mm^2.

$$A_s = \frac{n_s I_m}{J_c k_{fill}} \tag{3.14}$$

Stator slot pitch (τ_s) is defined by (3.15) and yields a value of 8.36 mm.

$$\tau_s = \frac{\tau}{3q} \tag{3.15}$$

Before calculating the other parameters, it may be useful to have a diagram with marked dimensions as shown in Figure 3-1.

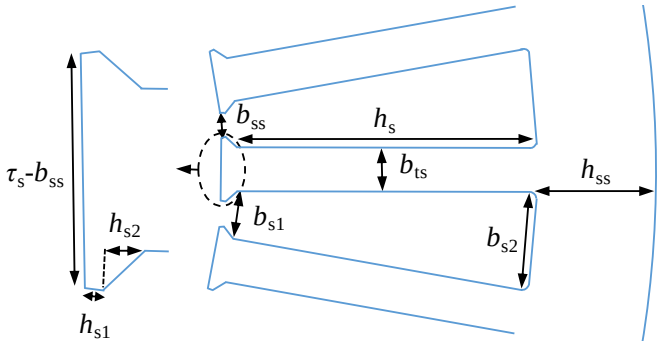

Figure 3-1: Stator dimensions.

Usually M19-29G lamination saturates in the flux densities above 1.8 T. In order to be on the safe side, tooth flux density of the stator (B_{ts}) is considered as two times the B_{1dm}, which is equal to 1.67 T to calculate value for stator tooth width (b_{ts}) of 4.24 mm as defined by (3.16).

$$b_{ts} = B_{1g\ max} \cdot \frac{\tau_s}{B_{ts}} \tag{3.16}$$

The inner slot width (b_{s1}) can be mathematically expressed as in (3.17). In order to calculate this expression h_{s1} and h_{s2} are set to be 0.5 mm and 1 mm, respectively, which finally yield a value of 4.38 mm for b_{s1}.

$$b_{s1} = \frac{\pi\left(D + 2\times(g + h_{s1} + h_{s2})\right)}{6Pq} - b_{ts} \tag{3.17}$$

The already calculated effective slot area by (3.14) can be used in (3.18) assuming that the slot area is in a trapezoidal shape. Accordingly, the outer slot width (b_{s2}) can be calculated using (3.19).

$$A_s = \frac{h_s\left(b_{s1} + b_{s2}\right)}{2} \tag{3.18}$$

$$b_{s2} = \frac{\pi\left(D + 2\times(g + h_{s1} + h_{s2} + h_s)\right)}{6Pq} - b_{ts} \tag{3.19}$$

One can easily see the nonlinear relationship between h_s and b_{s2} in (3.18). Accordingly, it is suggested to manually set a value for h_s considering reasonable split ratio values, long enough yoke width to prevent saturation, and enough available space for the winding sets. i.e., A_s. Taking into account these considerations, h_s is set to be equal to 28 mm and consequently b_{s2} will be equal to 9.33 mm. Slot opening width (b_{ss}) must be selected carefully to make the manufacturing and winding process easier while also preventing any high harmonic contents for the fabricated machine. A relatively large b_{ss} may result in a higher harmonic content in the air-gap MMF; therefore, b_{ss} is set to be approximately equal to two times the conductor size. According to the desired output power, power factor, voltage rating of the machine, and allowed current density for a copper conductor, AWG 17 is recommended as the conductor of the machine. According to AWG 17 standard size, the calculated b_{ss} is equal to 2.3 mm.

Finally the stator yoke height (h_{ss}) is calculated assuming the average flux density at yoke (B_{ss}) equal to two times that of the $B_{1g\ max}$ (3.20). The calculated value of h_{ss} is consequently equal to 11.98 mm.

$$h_{ss} = \frac{B_{1g\ max}}{B_{ss}} \cdot \frac{\tau}{\pi} = \frac{\tau}{2\pi} \tag{3.20}$$

So far all the physical parameters of the stator are calculated except stator winding parameters such as number of turns per phase (n_s) and detailed conductor size calculation. These parameters can be theoretically calculated by evaluating the inductances and developing the required expressions for the phase voltage at the base speed. Slot permeance (λ_s) is approximately expressed by (3.21) and calculated to a value of 4.5834 H.

$$\lambda_s \approx \frac{2h_s}{3\left(b_{s1} + b_{s2}\right)} + \frac{2h_{s2}}{b_{s1} + b_{ss}} + \frac{h_{s1}}{b_{ss}} \tag{3.21}$$

Differential permeance (λ_z) is approximately expressed by (3.22) and calculated to a value of 0.1357 H.

$$\lambda_z \approx \frac{5g}{5b_{ss} + 4g} \tag{3.22}$$

When calculating the phase resistance, it is also important to consider the end winding length (l_f). Coil set of each end winding is assumed to have an end winding curvature with a radius of $\tau/2$. This is an approximated value, and may vary depending on the winding methods, n_s and wire gauge. The calculated value for l_f is 118.2 mm according to (3.23).

$$l_f = \pi \cdot \frac{\tau}{2} \tag{3.23}$$

End coil permeance (λ_f) can be defined as in (3.24) to obtain an evaluated value of 0.01 H.

$$\lambda_f = 0.34 \times \frac{q}{L}\left(l_f - 0.64\tau\right) \tag{3.24}$$

Now, L_l will be equal to $6.1089\times10^{-6}n_s^{\,2}$ according to (3.25).

$$L_l = 2Pq\mu_0 n_s^{\,2}\left(\lambda_s + \lambda_z + \lambda_f\right)L \tag{3.25}$$

Using calculated L and l_f, the total coil length per slot (l_c) can be found by (3.26) yielding a value of 377.9 mm.

$$l_c = 2\left(L + l_f\right) \tag{3.26}$$

Phase resistance (R_s) is calculated for continuous operation taking into account the temperature rise inside the stator winding and is governed by (3.27) yielding a value of $7.7\times10^{-4}n_s^{\,2}$.

$$R_s = \rho_{120} l_c Pq \frac{J_c}{n_s I_m} n_s^{\,2} \tag{3.27}$$

Magnetizing inductance (L_m) can also be expressed in terms of n_s using (3.28) to obtain a value of $1.12\times10^{-4}n_s^{\,2}$.

$$L_m = \frac{6\mu_0 \tau LP\left(qn_s k_{w1}\right)^2}{\pi^2 g k_c\left(1+k_s\right)} \tag{3.28}$$

Now, d- and q-axis components of the magnetizing inductances. i.e., L_{dm} and L_{qm} in terms of n_s are obtained by (3.29) and (3.30) equal to $107\times10^{-6}n_s^{\,2}$ and $6.154\times10^{-6}n_s^{\,2}$, respectively.

$$L_{dm} = L_m k_{dm1} \tag{3.29}$$

$$L_{qm} = L_m k_{qm1} \tag{3.30}$$

Equations (3.25) and (3.30) yield values for L_l and L_{qm} of $6.1089\times10^{-6}n_s^2$ and $6.154\times10^{-6}n_s^2$ verifying the initial approximation of $L_l \approx L_{qm}$. D- and q-axis inductances using the approximate equations (3.31) and (3.32) are equal to $113\times10^{-6}n_s^{\,2}$ and $12.3\times10^{-6}n_s^{\,2}$, respectively.

$$L_d = L_{dm} + L_l \approx L_{dm} + L_{qm} \tag{3.31}$$

$$L_q = L_{qm} + L_l \approx 2L_{qm} \tag{3.32}$$

Voltage-current vector diagram of the SynRM in d-q reference frame is shown in Figure 3-2. According to Figure 3-2, the d- and q-axis voltage components can be easily expressed by (3.33) and (3.34). Although at this point I_{dm} and I_{qm} are unknown, the n_s term in L_d and L_q can be used to combine with I_{dm} and I_{qm} to produce $n_s I_{dm}$ and $n_s I_{qm}$ terms, which are known via (3.11) and (3.12). Then V_{dm} and V_{qm} can be calculated in terms of n_s as $-0.6698n_s$ according to (3.33) and $2.5547n_s$ according to (3.34) , respectively.

$$V_{dm} = -\omega_b L_q I_{qm} + R_s I_{dm} \tag{3.33}$$

$$V_{qm} = \omega_b L_d I_{dm} + R_s I_{qm} \tag{3.34}$$

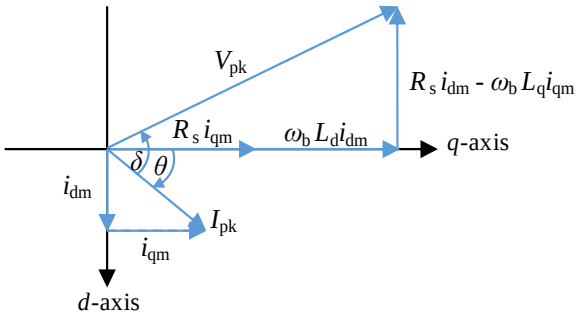

Figure 3-2: Voltage-current phasor vector diagram for a SynRM.

According to the voltage rating of the machine, n_s is directly calculated using (3.35), which is equal to 65 where the phase peak voltage (V_{rph}) is equal to 170V.

$$n_s = \frac{V_{rph}}{\sqrt{V_{dm}^{\ 2} + V_{qm}^{\ 2}}} \tag{3.35}$$

The stator peak phase current (I_m) can be calculated using (3.36), to yield a value of 5.26A.

$$I_m = \frac{n_s I_m}{n_s} \tag{3.36}$$

Based on n_s and J_c, the required copper wire diameter (d_{cu}) is calculated by (3.37), which is equal to 1.152 mm supported by AWG 17.

$$d_{cu} = \sqrt{\frac{4 \times n_s}{\pi \times J_c}} \tag{3.37}$$

Since the machine has been designed for maximum power factor achievement, the current angle with respect to q-axis (θ) is given by (3.38), which equals to 18.26^0 for a ξ value of 9.18.

$$\theta = 90^0 - \tan^{-1}\sqrt{\xi} \tag{3.38}$$

Table 3-2 summarizes the calculated stator dimensions and winding parameters as follows.

Table 3-2: Calculated Stator dimensions and winding parameters.

Parameter	**Value**	**Parameter**	**Value**
L	70.7 mm	b_{ss}	2.3 mm
D	95.8 mm	h_{ss}	11.98 mm
Stator outer diameter	179.48 mm	h_{s1}	0.5 mm
b_{ts}	4.24 mm	h_{s2}	1 mm
b_{s1}	4.31 mm	I_m	5.26 A
b_{s2}	9.27 mm	n_s	65 turns
h_s	28 mm		

3.3 Rotor Design and Design Variables

The design of the rotor structures using analytical methods is challenging due to the highly anisotropic structure of a four flux barrier SynRM as discussed before. Therefore, a FE-based design method is used to obtain the rotor structures considering the desired operating properties. Two types of rotor structures, namely a constant air-gap rotor (normal rotor) and a cut-off rotor, are used in the analysis as shown in Figure 3-3 with the d- and q-axis flux directions. For the sake of the rotor's mechanical rigidity, the radial ribs are added and flux barrier ends are filleted.

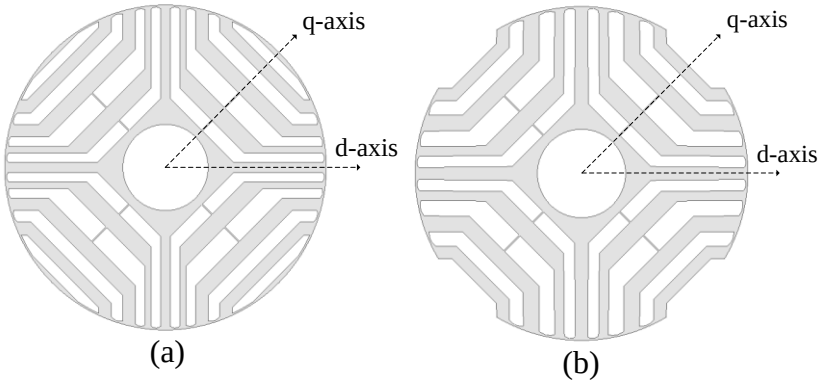

Figure 3-3: SynRM's rotor structure (a) normal rotor and (b) cut off rotor.

The proposed rotor structure for SynRM's flux barriers and carriers arrangement along the q-axis is defined based on analysis reported in [21]; however, the flux barrier and carrier widths and angles along the d-axis are defined as free variables, which are subjected to change and are determined by the optimization algorithm. Although this way of introducing free variables along d-axis can complicate the rotor structure development in FE environment, it offers great versatility for the optimization algorithm to find an optimal barrier arrangement.

Important coordinates and design variables are shown in Figure 3-4. Flux carrier and barrier widths along the d-axis are denoted by S_{nd} and W_{nd}, respectively, where n represents the corresponding segment number. Optimal arrangement of the flux barrier and carrier widths may result in optimized d-axis insulation ratio, which yields a higher d-axis inductance (L_d) and saliency ratio (ξ). Rotor slot pitch controller angle (β) specifies the available d-axis room, and flux barrier angle (γ), directly a dependent of k, determines the flux path along the d-axis. In addition to the provisions for the d-axis flux and inductance, the flux barrier and carrier widths along the q-axis are defined based on the analysis reported in [21] as functions of β and (P_n, P_n) to support unity q-axis insulation ratio (k_{wq}) as a desirable value for maximum power factor achievement. R_0 is the effective rotor radius considering the end fillet of the flux barrier.

Additionally k is defined to give a full degree of freedom in the flux barrier angle (γ) changes within the available space in the d-axis.

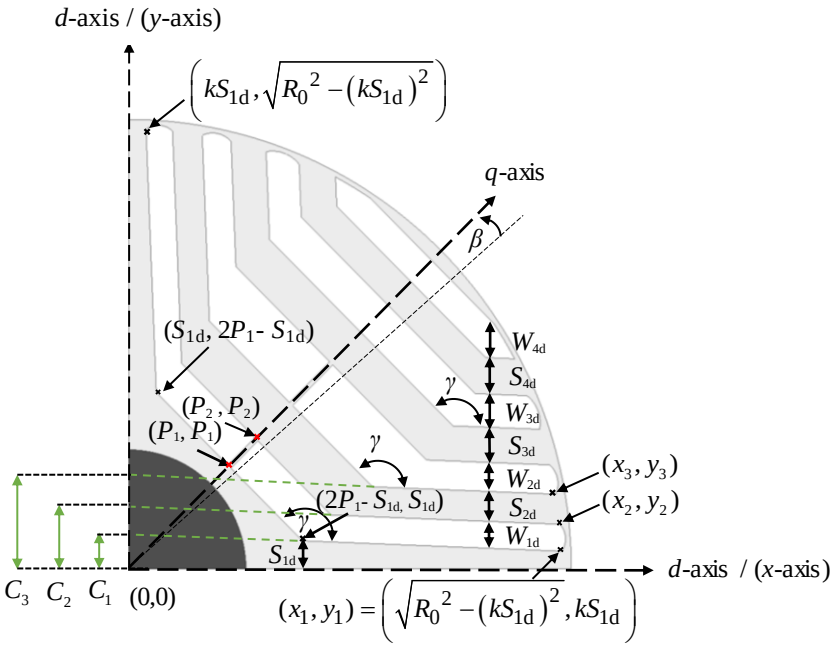

Figure 3-4: Rotor structure, design variables, and important coordinates.

The rotor flux barriers are comprised of lines and three point arcs. The systematical way of deriving the coordinates are explained in detail as follows. q-axis intersection of each flux barrier line has a symmetrical coordinate denoted by (P_n, P_n), which can be calculated using (3.39), (3.40), and (3.41), while the q-axis flux barrier and carriers widths are the functions of k_{wq} and β and expressed as in [21]. And also S_{nq} and W_{nq} represents the nth flux carrier and barrier along q-axis. For example in (3.40) when n=2, $W_{0.5nq}$ equals to W_{1q}.

$$P_1 = \frac{R_{shaft} + S_{1q}}{\sqrt{2}} \tag{3.39}$$

$$P_n = \frac{P_{n-1} + W_{0.5nq}}{\sqrt{2}} \qquad n = 2, 4, 6, 8 \tag{3.40}$$

$$P_n = \frac{P_{n-1} + S_{0.5(n+1)q}}{\sqrt{2}} \qquad n = 3, 5, 7 \tag{3.41}$$

In this thesis, an equal flux barrier angle is considered for all flux barriers. Hence each flux barrier line along d-axis has the same gradient. Prior to calculating the gradient, middle and end points of the flux barrier line along d-axis need to be mathematically expressed using known parameters and expressions as marked on Figure 3-4. Since the quarter of the rotor structure is symmetrical around q-axis, coordinates can be mirrored to obtain the corresponding point on the other side. Gradient (m) can be expressed using the defined middle and end point coordinates to yield an expression described in (3.42).

$$m = \frac{(1-k)S_{1\mathrm{d}}}{(2P_1 - S_{1\mathrm{d}}) - \sqrt{R^2{}_0 - (kS_{1\mathrm{d}})^2}} \tag{3.42}$$

At this point y intersection of the first d-axis flux barrier line (C_1) calculation is not necessary, as the end coordinates (x_1, y_1) are already known as shown in Figure 3-4. Since the gradient of all flux barrier lines along d-axis are the same according to (3.42) and if the midpoint coordinates to be in the form of ($x_{\text{t-mid}}$, $y_{\text{t-mid}}$), then (3.43) and (3.44) show the mathematical expressions for the respective midpoint coordinates of flux barrier lines along d-axis where t is the corresponding flux barrier line number.

$$(x_{\text{t-mid}}, y_{\text{t-mid}}) = \left(2P_t - \sum_{n=1}^{0.5t} (S_{\mathrm{nd}} + W_{\mathrm{nd}}), \sum_{n=1}^{0.5t} (S_{\mathrm{nd}} + W_{\mathrm{nd}}) \right) ;\ t = 2, 4, 6, 8 \tag{3.43}$$

$$(x_{\text{t-mid}}, y_{\text{t-mid}}) = \left(\left(2P_t - \sum_{n=1}^{0.5(t+1)} S_{\mathrm{nd}} - \sum_{n=1}^{0.5(t-1)} W_{\mathrm{nd}} \right), \left(\sum_{n=1}^{0.5(t+1)} S_{\mathrm{nd}} + \sum_{n=1}^{0.5(t-1)} W_{\mathrm{nd}} \right) \right); \ t = 3, 5, 7 \tag{3.44}$$

In order to calculate the endpoint coordinates of each flux barrier lines along d-axis, one may express the y axis intersection (C_{t}) of each d-axis flux barrier line using (3.45) and (3.46).

$$C_{\mathrm{t}} = \sum_{n=1}^{0.5t} (S_{\mathrm{nd}} + W_{\mathrm{nd}}) - m \left(2P_t - \sum_{n=1}^{0.5t} (S_{\mathrm{nd}} + W_{\mathrm{nd}}) \right); \ t = 2, 4, 6, 8 \tag{3.45}$$

$$C_{\mathrm{t}} = \sum_{n=1}^{0.5(t+1)} S_{\mathrm{nd}} + \sum_{n=1}^{0.5(t-1)} W_{\mathrm{nd}} - m\left(2P_t - \sum_{n=1}^{0.5(t+1)} S_{\mathrm{nd}} - \sum_{n=1}^{0.5(t-1)} W_{\mathrm{nd}} \right); \mathrm{t} = 3, 5, 7 \tag{3.46}$$

Now the corresponding endpoint coordinates of each d-axis flux barrier line (prior to filleting) can be expressed in terms of R_0, C_{t}, and m as shown in (3.47) and (3.48). The first two d-axis flux barrier line end points are in the form of (x'_{t}, y'_{t}) as marked in Figure 3-5. The endpoint coordinates must satisfy each d-axis flux barrier line and the rotor outer circle equations. Since the considering rotor quarter is also in 1st quarter of the *x*-*y* reference frame, only the positive solution of the quadratic equation (3.47) is selected for *x* coordinate value.

$$x'_{\mathrm{t}} = \frac{\sqrt{R_0^{\,2}(1+m^2) - C_t^{\,2}} - mC_{\mathrm{t}}}{1+m^2} \; ; \mathrm{t} = 2 \ldots 8 \tag{3.47}$$

$$y'_{\mathrm{t}} = mx'_{\mathrm{t}} + C_t \; ; \mathrm{t} = 2 \ldots 8 \tag{3.48}$$

In this study, filleting of each flux barrier is also incorporated to the design to enhance the mechanical rigidity of the rotor structure. Figure 3-5 shows an exaggerated illustration of first flux barrier filleting, important coordinates, and corresponding angles.

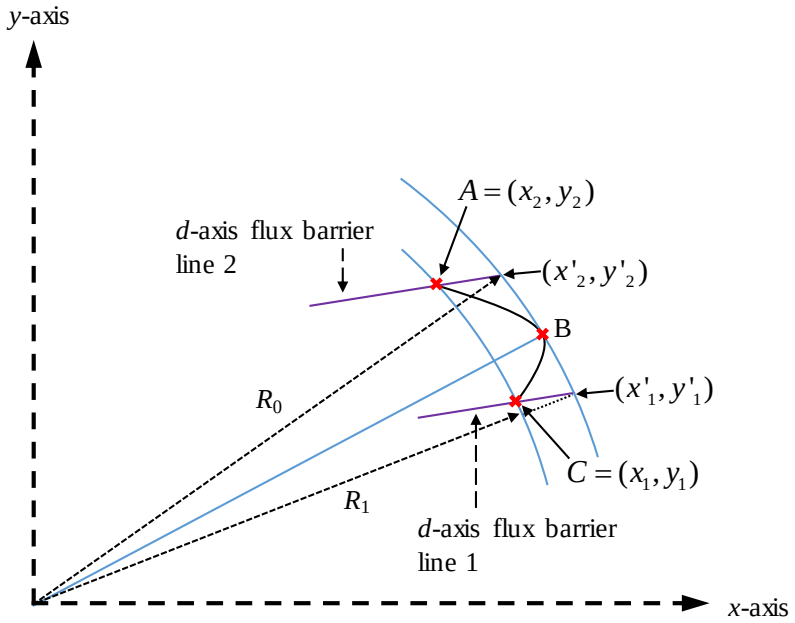

Figure 3-5: Coordinates of the 1st barrier fillet.

Prior to defining the three point arc, A, B, and C point coordinates need to be expressed in terms of (x'_1, y'_1) and (x'_2, y'_2) also taking into account how much filleting is needed by setting a reasonable value for filleting radius (R_1), which is typically slightly smaller than R_0.

Point B is assumed to be the midpoint of the curvature between known d-axis flux barrier line endpoints (i.e. (x'_1, y'_1) and (x'_2, y'_2)). Using trigonometric relationships, point B coordinates in the *x*-*y* Cartesian plain can be expressed as in (3.49).

$$B = \left(R_0 \cos\left(0.5\tan^{-1}\left(\frac{y'_1}{x'_1}\right) + 0.5\tan^{-1}\left(\frac{y'_2}{x'_2}\right)\right), R_0 \sin\left(0.5\tan^{-1}\left(\frac{y'_1}{x'_1}\right) + 0.5\tan^{-1}\left(\frac{y'_2}{x'_2}\right)\right)\right) \quad (3.49)$$

Points A and C are also on respective d-axis flux barrier line. If they are assumed to be on a circular path of radius R_1 (which is smaller than R_0), coordinates of the point A and C can be found in a similar manner to the previous calculations shown in (3.47) and (3.48) by replacing R_0 by R_1. Adding the radial ribs to the design is relatively easy as (P_n, P_n) coordinates are already known. In this thesis it is assumed that both radial and tangential ribs width are equal to 0.5 mm.

A similar set of variables are used in the FEA environment to generate the flux line coordinates to test different rotor structures during each step of the optimization, so that the optimizer can directly find the optimal dimensions to meet the considering objective function.

3.4 Objective Functions (OFs)

Three OFs are defined for torque ripple minimization (RM) (3.50), saliency ratio maximization (SM) (3.51), and a COF (3.52) to find a compromise design with minimized torque ripple and maximized saliency ratio while supporting the required torque. In (3.52), ξ_0, T_{rip0}, and T_0 are the maximum possible saliency ratio found by (3.51), the minimum torque ripple obtained by (3.50), and 10.61 Nm as the required rated torque, respectively.

$$\min\left(T_{\text{rip}} = \frac{T_{\max} - T_{\min}}{T_{\text{avg}}}\right) \tag{3.50}$$

$$\max\left(\xi = \frac{L_{\text{d}}}{L_{\text{q}}}\right) \tag{3.51}$$

$$\min\left(0.2\left[\xi - \xi_0\right]^2 + 0.2\left[T_{\text{avg}} - T_0\right]^2 + 0.6\left[T_{\text{rip}} - T_{\text{rip}_0}\right]^2\right) \tag{3.52}$$

In an iterative optimization algorithm, careful definition of design variable constraints helps to avoid generating infeasible rotor structures during optimization. Firstly, a linear constraint is set to take care of the summation of W_{nd} and S_{nd} keeping this value within the available d-axis room. In order to determine the minimum values of W_{nd} and S_{nd} along the d-axis flux path, described by (3.53) and (3.54), respectively, a slope (m) constraint defined by (3.42) should be considered; otherwise, unrealistic rotor structures may be generated. Effectively "m" controls γ as shown in Figure 3-4. It is worth noticing that P_{n} in (3.53) and (3.54) denotes the q-axis intersection coordinate of the n^{th} barrier line along the q-axis.

$$W_{\text{nd}} = \frac{2m}{m+1}(P_{2\text{n}} - P_{2\text{n-1}})\text{; n = 1, 2, 3, 4} \tag{3.53}$$

$$S_{(\text{n+1})\text{d}} = \frac{2m}{m+1}(P_{2\text{n+1}} - P_{2\text{n}})\text{; n = 1, 2, 3, 4} \tag{3.54}$$

The feasible design variable ranges are shown in Table 3-3 and β is set between 4° to 11° to reduce the torque ripple, and k is set between 0.625 to 3 to cover all possible flux barrier and carrier arrangements in d-axis providing at least 1.5 mm space between the edges of the first flux barriers in two adjacent poles. According to these two ranges γ may change between 120° to 140° and other design variables can have their own possible minimum and reasonable maximum values reported.

Table 3-3 : Design variables ranges.

Variable	Min	Max	Variable	Min	Max
β (deg)	4	11	k	0.625	3
S_{1d} (mm)	1	4	W_{1d} (mm)	1.8	4.1
S_{2d} (mm)	1.2	4.5	W_{2d} (mm)	2.4	5
S_{3d} (mm)	2.2	6.9	W_{3d} (mm)	2.7	5
S_{4d} (mm)	2.8	6	W_{4d} (mm)	2.5	5

3.5 Selecting Candidates, Related Design Variables Dimensions, and Machines Structures

In order to conduct the FEA and find the optimized SynRMs, ANSYS-Maxwell and its optimetrics toolbox have been used, respectively. The optimetrics' built-in Genetic Algorithm (GA) optimizer has been run for 50 generations using an 8-core (3.4 GHz Intel® Core-i7) machine with a 64-bit operating system and 16 GB of RAM. An average time of 6 hours was recorded for each optimization run. Using two different rotor geometries (normal and cut off), and three OFs discussed before, six optimized SynRMs are separately introduced for further analysis. As shown in Figure 3-6, each machine is selected from more than 1500 generated candidates by considering the corresponding OF and selected machines are marked in their three dimensional Pareto surfaces of ξ, T_{rip}, and T_{avg}.

Table 3-4 shows the optimized design variables. As is seen in Table 3-4, minimized torque ripple characteristic is seen for the cases with the lowest β of 6.63° and 5.43° in the RM-normal rotor and RM-cutoff rotor SynRMs, respectively. For the SM-based designs, the behavior of β is exactly contrary to the RM-based designs. Figure 3-7 shows a plot of the flux lines superposed on the machine structure for the rated operating condition for the optimally designed and a non-optimized [21] SynRMs. And it also shows the flux density distribution corresponding to the flux lines.

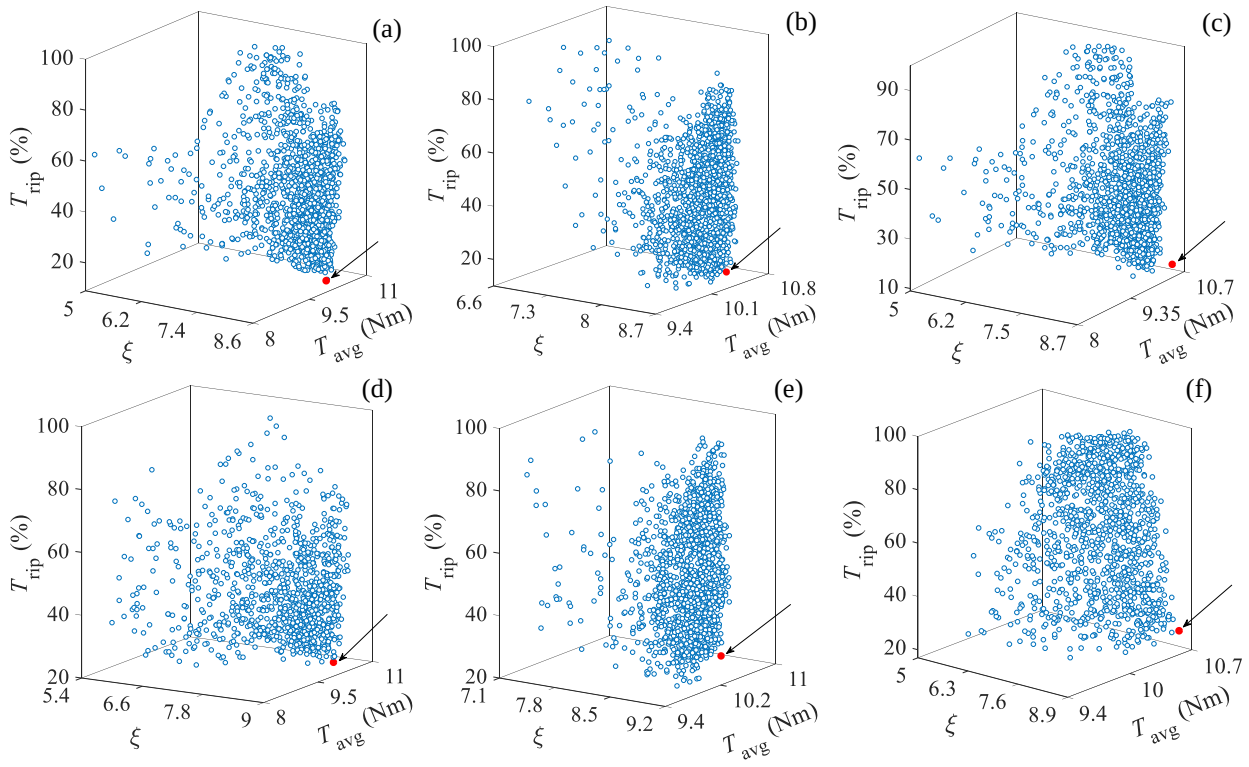

Figure 3-6 : Saliency ratio (ξ), average torque (T_{avg}), and torque ripple (T_{rip}) variations at rated operating point for the generated solutions in (a) RM (normal rotor), (b) SM (normal rotor), (c) COF (normal rotor), (d) RM (cut off rotor), (e) SM (cut off rotor), (f) COF (cut off rotor).

Table 3-4 : Optimized design variable.

	Preliminary design	**Normal rotor**			**Cut off rotor**		
Variables		SM	RM	COF	SM	RM	COF
β (deg)	7.000	9.833	6.637	7.000	6.469	5.432	6.022
k	1.000	0.756	0.657	1.000	0.866	0.719	0.863
γ (deg)	135.00	135.71	136.27	135.00	135.49	136.16	135.56
S_{1d} (mm)	2.754	1.379	1.772	1.521	1.767	1.988	1.986
S_{2d} (mm)	5.284	2.249	3.814	1.861	2.213	2.907	2.753
S_{3d} (mm)	4.590	3.207	4.311	3.638	3.429	4.666	4.553
S_{4d} (mm)	3.500	3.412	4.091	3.840	5.308	5.597	3.618
W_{1d} (mm)	2.676	2.399	2.498	2.753	2.409	3.798	3.174
W_{2d} (mm)	4.009	3.290	4.354	2.870	2.434	2.475	4.362
W_{3d} (mm)	2.691	3.682	4.932	3.431	4.010	4.472	4.038
W_{4d} (mm)	2.063	4.650	3.299	3.698	4.828	5.100	4.218

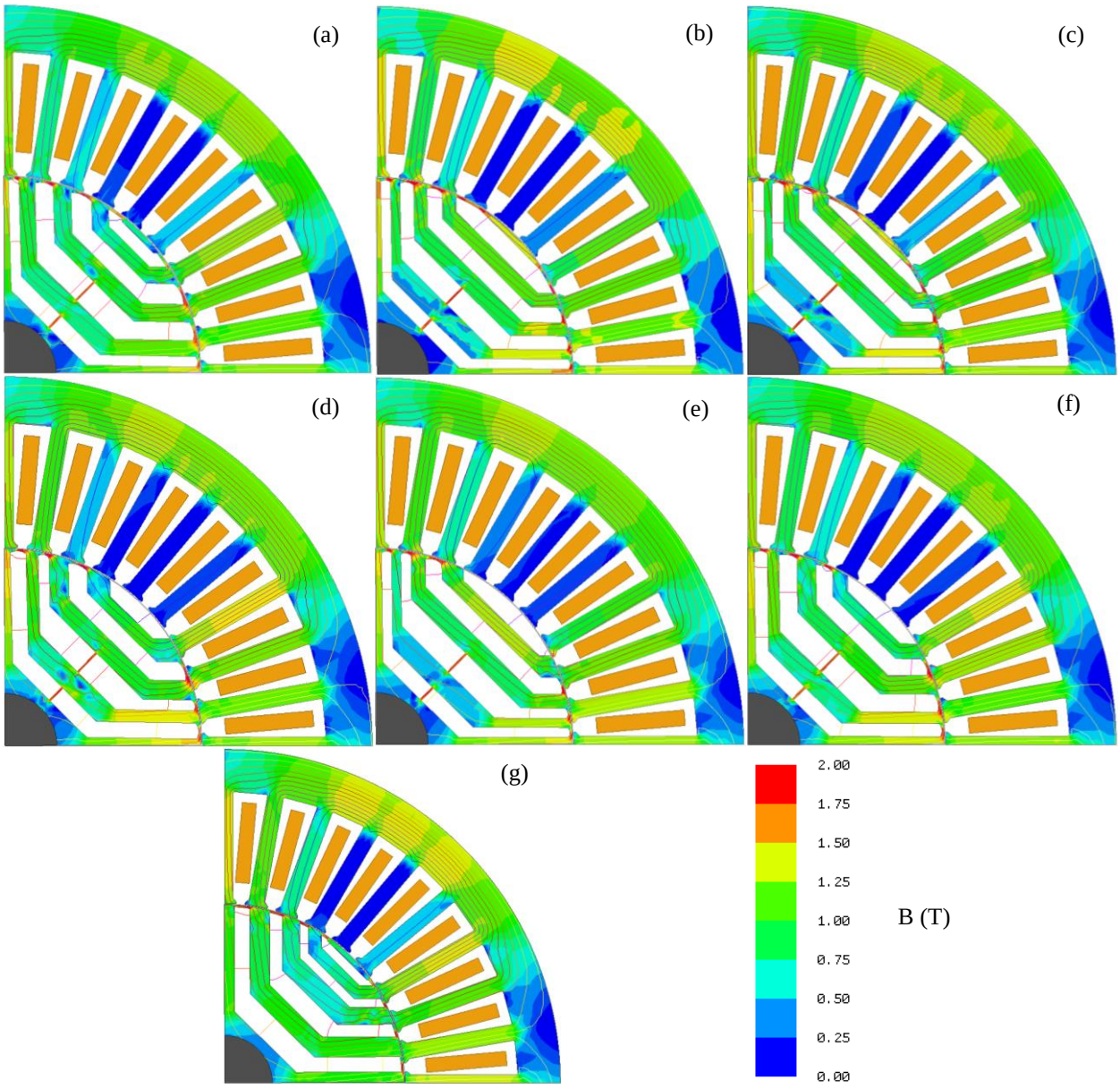

Figure 3-7: The structure, flux lines and flux density distribution in rated operating condition for (a) RM-normal rotor, (b) SM-normal rotor, (c) COF-normal rotor, (d) RM-cut off rotor, (e) SM-cut off rotor, (f) COF-cut off rotor, and (g) Non-optimized preliminary designed SynRMs.

As is seen in Table 3-4 and the SynRMs structure shown in Figure 3-7, β increases to 9.83° and 6.46° for the SM-normal rotor and SM-cutoff rotor SynRMs, respectively. The β values for the COF-based designs lie between the RM-based and SM-based designs. In all of the optimized SynRMs, γ is equal or above 135°, while the highest γ of 136.27° and 136.16° are seen for RM-normal rotor and RM-cut off rotor SynRMs, respectively. Although the preliminary designed

SynRM is able to support the required rated torque, the optimized SynRMs have significantly smaller torque ripples and larger saliency ratios while still supporting the required torque.

Table 3-5 shows the torque ripple of the preliminary design is 90%, while the torque ripple can be minimized even to 9.25% in the normal rotor structure and 21% in the cutoff rotor structure. Although no radial rib and filleting on the barrier ends exist in the preliminary designed SynRM, this machine can only support a saliency ratio of 8.1, which is much smaller than the SM-cutoff rotor and SM-normal rotor SynRMs with the saliency ratios of 8.99 and 8.66, respectively. The saliency ratios and torque ripples of cutoff rotor structures are 0.15 to 0.36 and 10.6% to 12% larger than their normal rotor structure counterparts, respectively. The torque ripple and saliency ratio of COF-based SynRMs lie between those of the SM-based and RM-based designs.

Table 3-5: Operating properties of the selected SynRMs.

	Preliminary design	**Normal rotor**			**Cut off rotor**		
		SM	RM	COF	SM	RM	COF
ξ	8.1	8.66	8.2	8.57	8.99	8.56	8.72
T_{avg}	10.61	10.56	10.67	10.6	10.66	10.78	10.63
T_{rip}	90%	16%	9.25%	12%	26.6%	21%	24%

3.6 Finite Element (FE) Based Comparative Study

In this section FE analysis of optimized six different machines are compared with each other as well as with the non-optimized preliminary design. The comparative analysis is consists of different performance indicators such as saliency ratio and torque ripple variation under different excitation levels, developed maximum power versus speed, power factor versus speed and finally efficiency versus speed.

3.6.1 Saliency Ratio

Saliency ratio variations of each designed SynRM are analyzed versus I_{pk} and θ changes and shown in Figure 3-8.

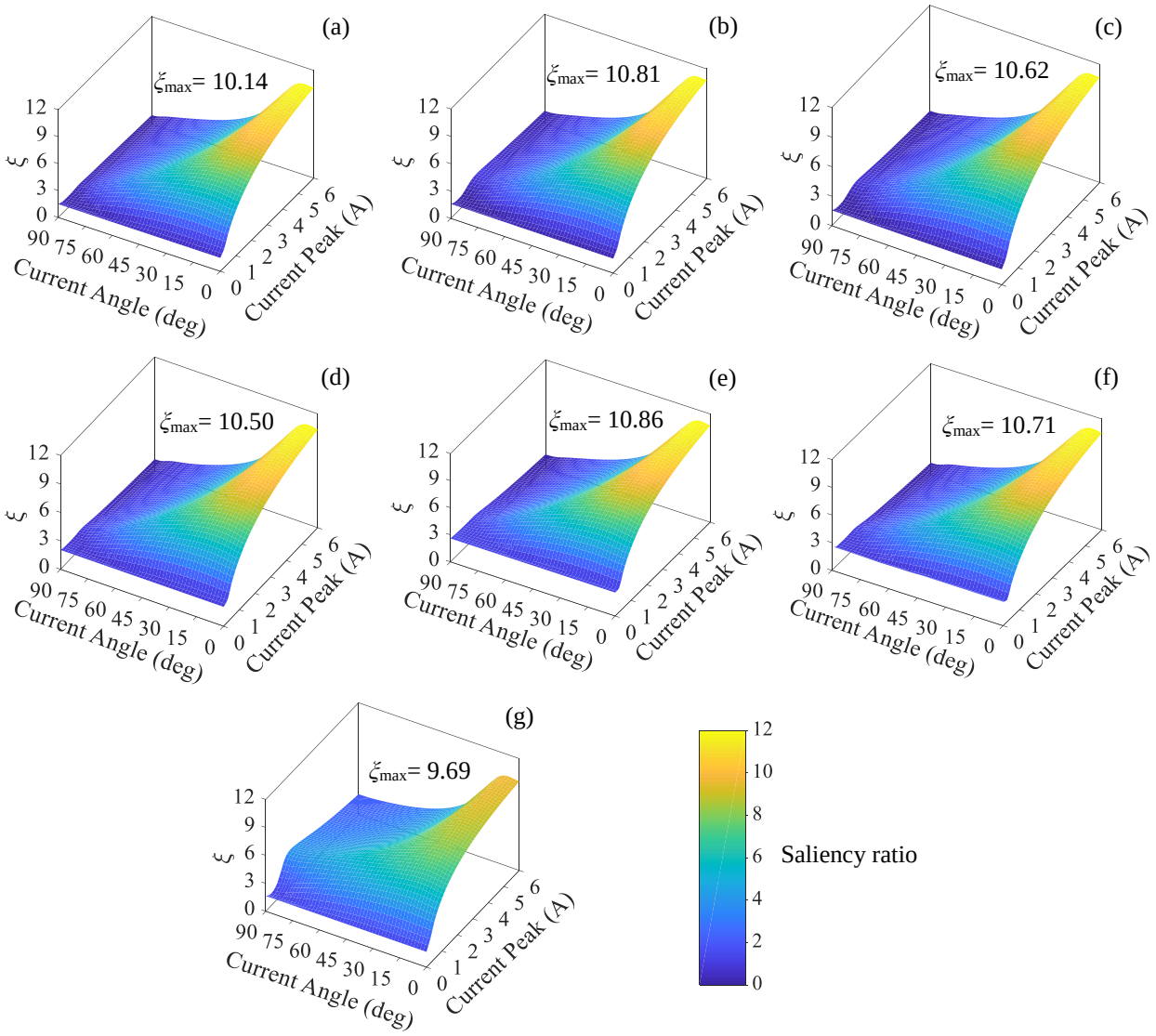

Figure 3-8 : Saliency ratio evaluation with respect to I_{pk} and θ variations for (a) RM-normal rotor (b) SM-normal rotor, (c) COF-normal rotor, (d) RM-cut off rotor, (e) SM-cut off rotor, (f) COF-cut off rotor, and (g) Non-optimized preliminary designed SynRMs.

I_{pk} varies between 0 A to 6 A and θ varies between 0° to 90°. According to Figure 3-8, a common trend for the saliency ratio variation versus the I_{pk} and θ changes is seen for all designed SynRMs. The saliency ratio is directly a function of the operating point and changes significantly

from values around 1 to even 10.86. By increasing θ in a given high I_{pk} (3 A to 6 A), the saliency ratio is significantly reduced, as the d-axis flux path becomes more magnetized. For example, a saliency ratio reduction from 9.69 to 2 and from 10.86 to 1 is predicted in this area for the preliminary designed and SM-cutoff rotor SynRMs, respectively. For lower current angles (0° to 20°), the saliency ratio is significantly increased versus I_{pk} increment. This phenomenon happens because the q-axis component of the current is dominant in the small θ, and by increasing I_{pk} the q-axis inductance gets reduced.

3.6.2 Torque Ripple

Torque ripple (T_{rip}) variation is predicted versus I_{pk} and θ changes for the designed SynRMs (see Figure 3-9). The gray colored areas in Figure 3-9 correspond to the operating points with larger than 100% torque ripple. The largest and smallest portion of the gray colored area is seen for the preliminary designed and RM-normal rotor SynRMs, respectively. In the preliminary designed SynRM, at least 80% of the remaining reported operating points show a torque ripple above 60%, while in the RM-normal rotor SynRM a large number of operating points have a torque ripple below 30%. In addition, the operating points with less than 100% torque ripple in the SynRMs with a normal rotor structure are more than those of with the cutoff rotor structure. In all of the torque ripple contour maps, the torque ripple is maximized in the relatively low (0° to 10°) and high (80° to 90°) current angles, because in these ranges of θ the developed torque of the SynRM is minimized and even a very small peak to peak torque variation results in a large torque ripple. A same scenario exists for the small I_{pk} (0 A-0.5 A) operating regions.

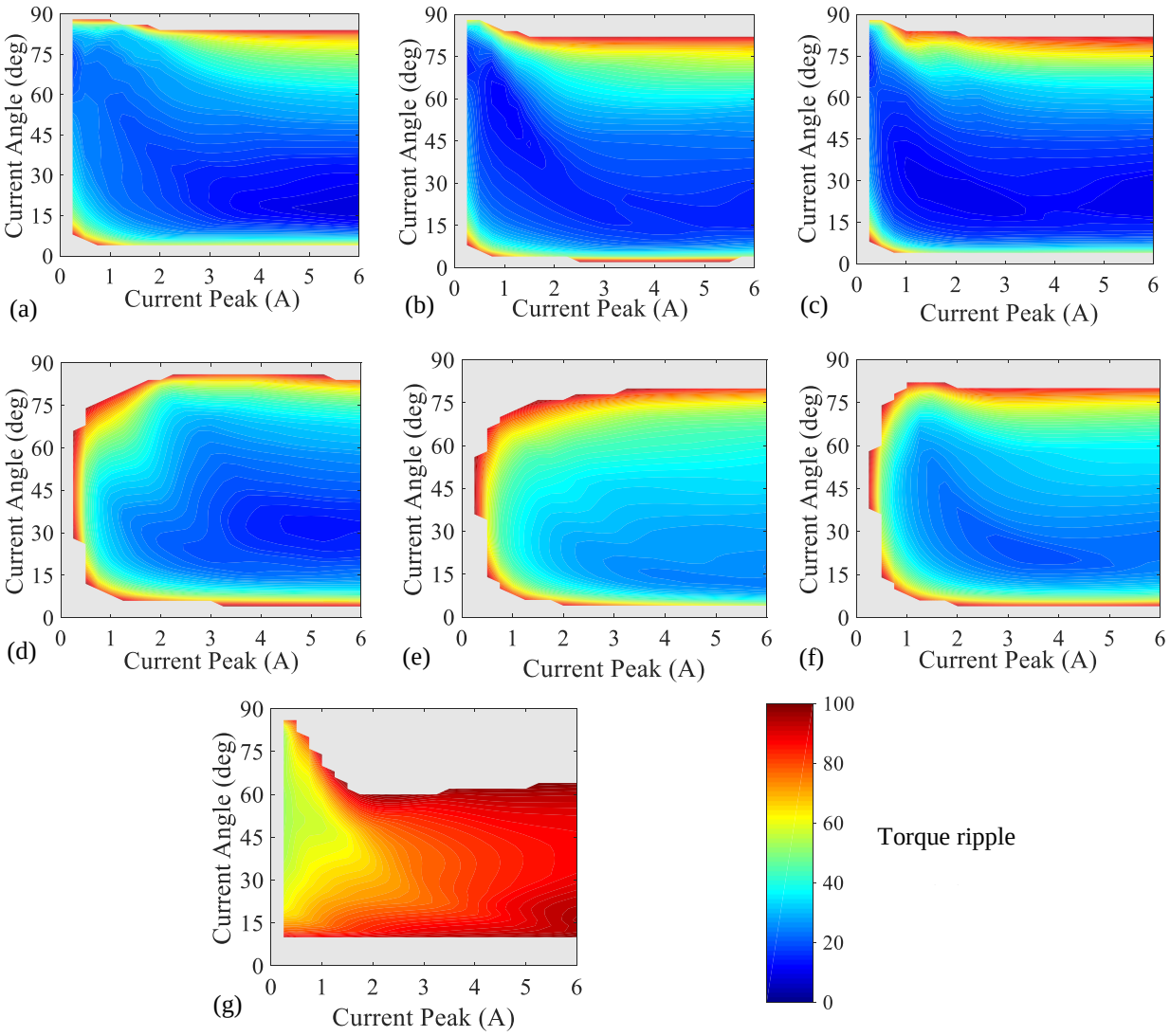

Figure 3-9: Torque ripple evaluation with respect to I_{pk} and θ variations for (a) RM-normal rotor (b) SM-normal rotor, (c) COF-normal rotor, (d) RM-cut off rotor, (e) SM-cut off rotor, (f) COF-cut off rotor, and (g) Non-optimized preliminary designed SynRMs.

3.6.3 Maximum Output Power

Below base speed, I_{pk} and θ are adjusted based on the Maximum Power Factor (MPF) current control strategy, and above base speed I_{pk} and/or θ may change to find the maximum possible developed power making sure that the peak of the fundamental and harmonic components of the machine's terminal voltage is not larger than 1 pu. Table 3-6 shows the I_{pk} (A) and θ (°) values for all designed SynRMs at each operating speed for their related maximum

developed powers. As is seen in Table 3-6, I_{pk} of the preliminary designed SynRM should reduce to even 2.47 A in 1800 rpm for its maximum possible developed power, otherwise the peak of the harmonic components in the machine's terminal voltage waveform significantly increase well beyond 1 pu. For the other SynRMs, since the MMF harmonic contents of the machine are indirectly reduced during the machine design optimizations, I_{pk} of 5.35 A can be still kept fixed in a wide speed range and only θ should reduce at higher speeds to support the maximum developed power.

Table 3-6: I_{pk} and θ variations versus speed changes.

Speed (rpm)	**300**	**600**	**900**	**1200**	**1500**	**1800**	**2100**	**2400**
Preliminary design	5.35A 18°	5.35 A 18°	5.35 A 18°	3.95 A 16.4°	3.05 A 16.4°	2.47 A 16.4°	- -	- -
SM (normal rotor)	5.35 A 18°	5.35 A 18°	5.35 A 18°	5.35 A 12.4°	5.35 A 8.6°	5.35 A 6.1°	5.35 A 3.9°	- -
RM (normal rotor)	5.35 A 18°	5.35 A 18°	5.35 A 18°	5.35 A 11.7°	5.35 A 8.1°	5.35 A 5.4°	5.35 A 2.8°	- -
COF (normal rotor)	5.35 A 18°	5.35 A 18°	5.35 A 18°	5.35 A 12.2°	5.35 A 8.5°	5.35 A 5.9°	5.35 A 3.6°	- -
SM (cut off rotor)	5.35 A 18°	5.35 A 18°	5.35 A 18°	5.35 A 12.6°	5.35 A 8.9°	5.35 A 6.5°	5.35 A 4.6°	5.35 A 2.95°
RM (cut off rotor)	5.35 A 18°	5.35 A 18°	5.35 A 18°	5.35 A 11.9°	5.35 A 8.3°	5.35 A 5.8°	5.35 A 3.6°	- -
COF (cut off rotor)	5.35 A 18°	5.35 A 18°	5.35 A 18°	5.35 A 12.4°	5.35 A 8.7°	5.35 A 6.1°	5.35 A 3.8°	- -

The designed SynRMs including the preliminary design are able to provide the rated power of 1 kW at the rated speed 900 rpm (see Figure 3-10 (b)). Corresponding average torque profiles are also given in Figure 3-10 (a) for convenience.

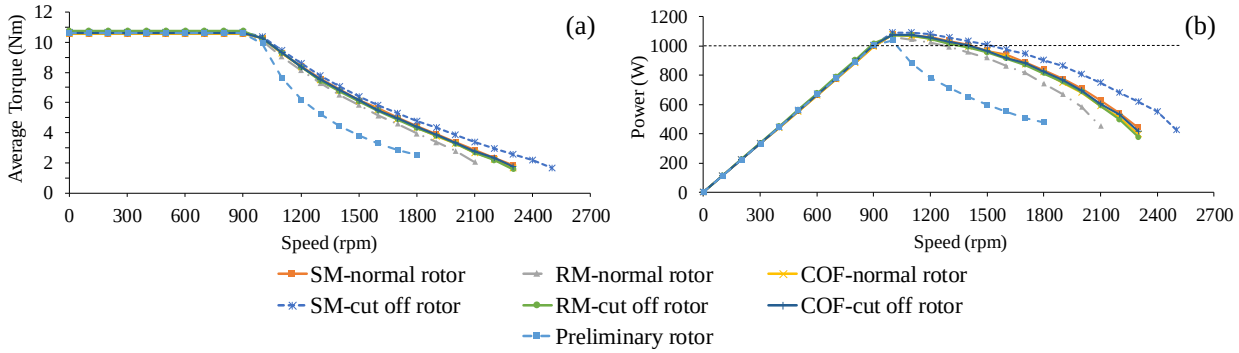

Figure 3-10: (a) Average torque and (b) maximum developed power comparison.

Up to base speed, I_{pk} and θ for all designed SynRMs are set to 5.35 A and 18°, respectively, to support the maximum power factor considering a desired saliency ratio of 9. Above base speed, all machines are capable to provide a peak power beyond 1 kW; for example the peak power of SM-cutoff rotor SynRM is 1088 W at 1100 rpm. However, the speed range in which a constant output power of 1 kW is satisfied is different for the designed machines. For instance, the preliminary designed SynRM can only support a 1 kW output power up to 1025 rpm, while the SM-cutoff rotor SynRM can support this power up to even 1500 rpm. The main reason for a much shorter speed range in the preliminary designed SynRM compared to its other optimized counterparts is its higher MMF harmonic content, which also shows its effects in the higher torque ripple content of this machine.

As the other finding, the RM-normal rotor and RM-cutoff rotor SynRMs have the shortest constant power speed range of up to 1250 rpm and 1350 rpm, respectively, compared to the other optimized machines. The speed ranges of COF-based SynRMs lie between the SM-based and RM-based SynRMs. From the power capability profiles, it is clearly seen that the higher saliency ratio property results in a wider speed range trait.

3.6.4 Power Factor and Efficiency

For the power factor and efficiency comparison, only the optimized SynRMs are analyzed as the preliminary designed SynRM did not show a promising power capability, torque ripple, and saliency ratio characteristics. The phase angle difference between the fundamental component of machine's terminal voltage and current is used for the power factor calculation. The I_{pk} values reported in Table 3-6, and the R_s equal to 3.83 (Ω) are used to assess P_{cu} in each operating point of the optimized SynRMs. Using FEA, the total P_{core} of the SynRMs in each operating point is recorded. Accordingly, the efficiency is calculated using (3.55). Figure 3-11, shows the power factor and efficiency profiles of the optimized SynRMs versus speed in their maximum output powers.

$$Eff\,(\%) = \frac{P_{out}}{P_{out} + P_{copper} + P_{core}} \times 100 \tag{3.55}$$

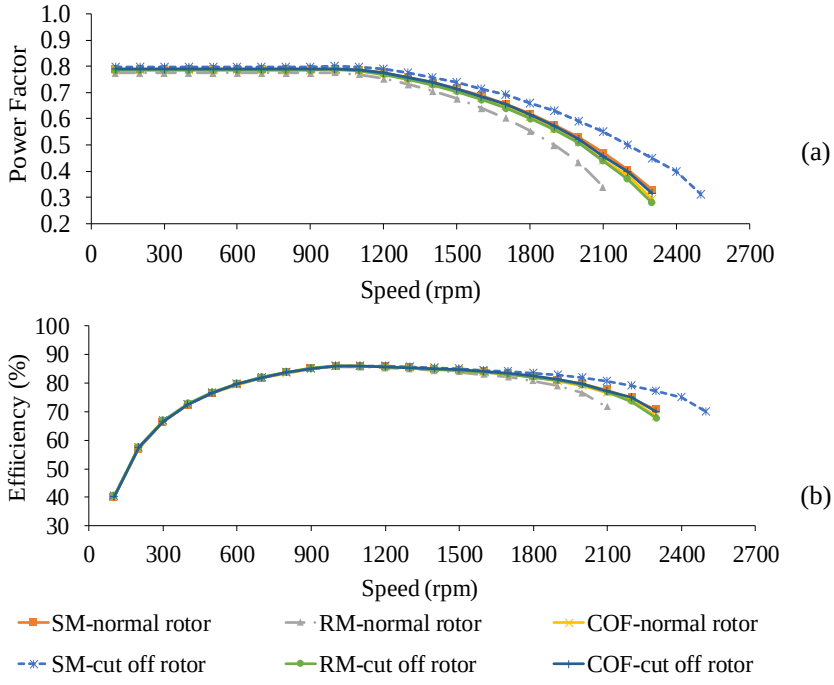

Figure 3-11: (a) Power factor variations in the maximum developed powers (b) efficiency versus speed profiles in the maximum developed powers.

As seen in Figure 3-11, all of the optimized SynRMs have power factors above 0.77 below base speed, which is close to the desired analytical 0.8 power factor in this region. From base speed to the speed at which the peak power is seen the power factors of SynRMs slightly increase; however, after this speed the power factor significantly reduces. For example, SM-cutoff rotor SynRM shows a power factor of 0.797 up to base speed, then its power factor increases to 0.799 at the peak power of 1088 W occurring at 1100 rpm, and finally the power factor even drops to 0.311 at the highest possible speed of 2500 rpm. It is worth noting that the highest and lowest power factors are seen for the SM-cutoff rotor and RM-normal rotor SynRMs respectively, while the power factor values of the other candidates including COF-based SynRMs lie in their between in the wide speed range. According to Figure 3-11(a), up to the speeds corresponding to the peak power, the efficiencies increase from 40% to even 86% (for SM-cutoff rotor) as the output power is increasing for all optimized SynRMs, while the copper losses are constant (164.3 W) and the core losses are less than 12 W. After this area, the efficiencies reduce to 65%-70% in the maximum possible speeds because of the reduction of the developed power and increment of core losses in this region. It is seen in Figure 3-11(b) that still SM-based SynRMs show the highest possible efficiencies compared to the RM-based SynRM, while the efficiencies of the COF-based SynRMs lie between SM- and RM-based designs.

3.7 Summary

An FE-based design optimization was conducted to obtain the optimal rotor structures of a four flux barrier TLA SynRM for the comparative study and performance improvement purposes. The Stator for 36-slot, four-pole SynRM is specifically designed using analytical electric and magnetic loading principles and a novel coordinate based four flux barrier rotor structure is introduced for the purpose of optimization. The coordinate based rotor includes

various possible design variables along the d- and q-axis flux paths. The optimized properties of the rotor structure were found for the RM-based, SM-based, and COF-based optimally designed SynRMs. It was shown that the torque ripple and saliency ratio of the SynRMs may significantly change, as a function of machine's operating points, for instance from 5% to above 100% and 1 to 10.86, respectively. Furthermore, the higher saliency ratio characteristic could result in a larger developed power, wider speed range, and higher power factor with the expense of a larger torque ripple. To make a compromise between the useful and unwanted operating characteristics, a COF-based optimized SynRM could be a reliable alternative.

Chapter 4

Performance Prediction of SynRM with Various SPP Values

In this chapter, same approach is used for rotor design optimization and performance prediction of a series of four flux barrier Transversally Laminated Anisotropic (TLA) SynRMs with various slot per pole per phase (SPP) properties and normal and cut off rotor structures. A COF is defined and solved to minimize the torque ripple and maximize the saliency ratio of the SynRMs while also supporting the desired developed torque.

4.1 Combined Objective Function Based Candidates

Rotor design optimization and performance improvement of SynRMs can be focused on either only a single performance indicator e.g., torque ripple, saliency ratio, and developed torque or a combination of two or more. Only considering one specific performance indicator in design steps may negatively affect the machine's performance from other perspectives. For instance, minimizing the torque ripple does not necessarily contribute to saliency ratio or developed torque betterment. Although the complexity of optimization grows with addition of more performance indicators and design parameters, the optimized machine may fulfill different favorable requirements at a same time. However, combined objective functions can compromise between different performance indicators and yield overall best performance.

The most important common parameters of the optimized SynRMs are similar to previous study given in Table 3.1 except the stator slot number. Here the stators of 24 (SPP = 2) and 48 (SPP = 4) slot, 4 pole SynRMs are analytically designed in addition to the previously designed 36 (SPP = 3) slot SynRM based on conventional electric and magnetic loading principles and the

requirements to support maximum power factor below the base speed[6]. The stator winding patterns are similar to those of distributed winding IMs with the same pole numbers. During the stator design steps, the machine's teeth and yoke are kept unsaturated under full load conditions. Most importantly all 3 designed stators are according to IEC-90S and have the same air-gap (g) length which is 0.35mm and the same coordinate based rotor structure is used since the rotor radius for each SPP case is similar. In fact, the same constrains are used for the variables as given in Table 3-3.

However, during design optimization, the corresponding ranges for each variable must be observed; otherwise unrealistic rotor structures may be generated. As the first constraint, the summation of the flux barrier and carrier widths along the d-axis must always be within the available room. According to [21], β must be defined within 4° to 11° for low torque ripple. This range for β determines the available d-axis room and contributes to flux barrier and carrier arrangements along the q-axis. In addition, there should be at least 1.5 mm distance between the edges of the first flux barriers of two adjacent poles for mechanical rigidity, and none of the flux barriers must intersect with the adjacent flux barrier in the same pole.

A COF (4.1) is used to find a compromised design possessing minimized T_{rip} and maximized ξ ($\xi = L_d/L_q$, L_d is d-axis inductance and L_q is q-axis inductance), while supporting the required average torque (T_{avg}). Prior to minimization of (4.1) it is important to identify the maximum possible ξ and minimum possible T_{rip} for each rotor structure. This is done by running two separate optimizations for saliency ratio maximization and torque ripple minimization for each of the analyzed machines. In (4.1) ξ, T_{avg}, and T_{rip} are calculated for each candidate solution, whereas ξ_0, T_0, and T_{rip0} are the optimized values already obtained by saliency ratio maximization, torque ripple minimization, and the rated torque, respectively. Weighting factors

for each part in (4.1) are selected proportional to the sensitivity of each parameter towards the outcome of the expression.

$$\min(0.2\left[\xi-\xi_0\right]^2+0.2\left[T_{\text{avg}}-T_0\right]^2+0.6\left[T_{\text{rip}}-T_{\text{rip0}}\right]^2) \tag{4.1}$$

Optimetrics toolbox of ANSYS-Maxwell and the inbuilt Genetic Algorithm (GA) method are used to run the optimization considering the defined ranges in Table 3-3 and the COF introduced in (4.1). One full GA run took nearly 6 hours on an 8-core (3.4 GHz Intel® Core-i7) machine with a 64-bit operating system and 16 GB of RAM to provide 1500 generated candidates after 50 generations. The results generated in each optimization are plotted against ξ, T_{avg}, and T_{rip} in Figure 4-1. The best selected candidate is marked in red and identified with an arrow.

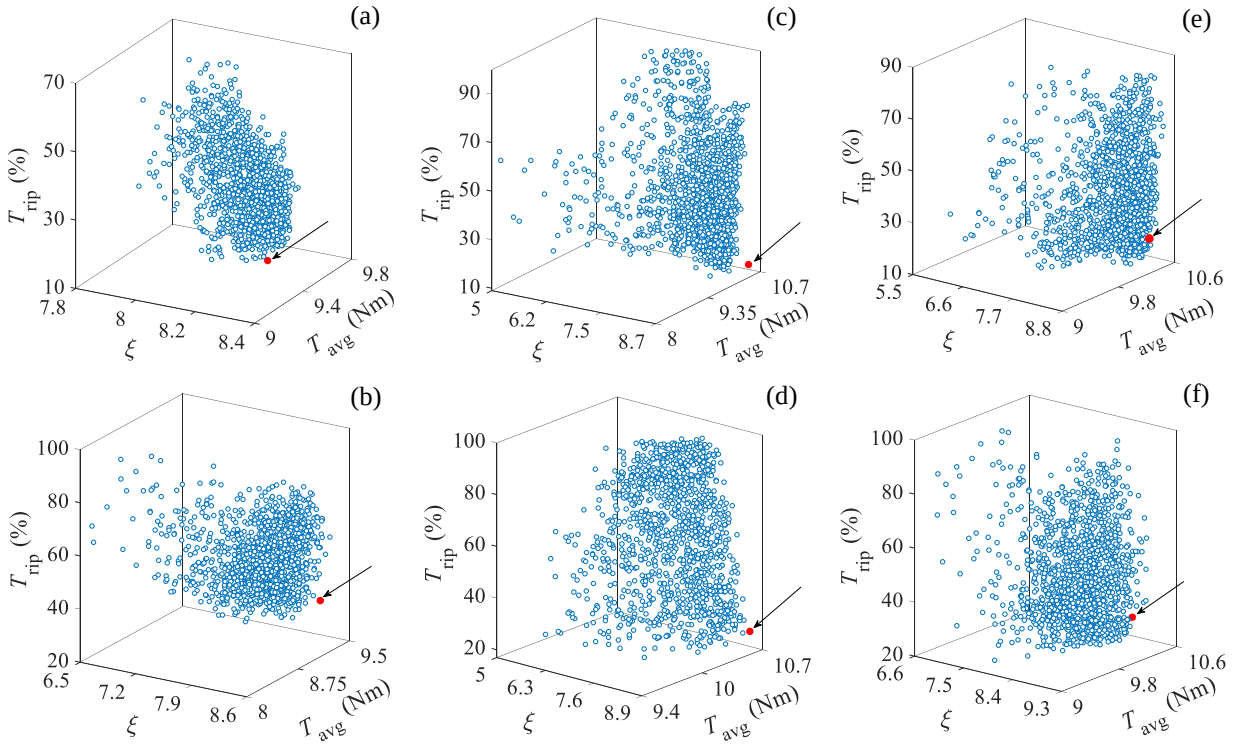

Figure 4-1: Saliency ratio (ξ), average torque (T_{avg}), and torque ripple (T_{rip}) variations at rated operating point for the generated solutions in (a) normal rotor (SPP = 2), (b) cut off rotor (SPP = 2), (c) normal rotor (SPP = 3), (d) cut off rotor (SPP = 3), (e) normal rotor (SPP = 4) and (f) cut off rotor (SPP = 4).

As seen in Figure 4-1, different ranges are selected for the axes to represent the actual variations of the related values. According to Figure 4-1, T_{rip} is the most sensitive parameter compared to the other performance indicators, i.e., ξ and T_{avg}. T_{rip} may change from 9% to 100%, while ξ and T_{avg} change from 5 to 9.4 and 8 to 10.7, respectively.

The smallest T_{avg} ranges of [9, 9.8] Nm and [8, 9.5] Nm appear in normal rotor and cut off rotor SynRMs both with SPP of 2, respectively. For SPP = 3 and SPP = 4, normal and cut off rotor structures show T_{avg} values ranging from 8 Nm to even 10.7 Nm. Specifically the SPP = 3 normal rotor structure shows numerous T_{avg} values around 10.6 Nm, which is the same as the T_{avg} value to support 1 kW of output power. In terms of T_{rip} variation for different rotor structures, normal rotor structures of SPP = 2, 3, and 4 show values ranging from 10% to 70% and SPP = 3 has a rotor with a lower T_{rip} value of 9%. On the other hand cut off rotor SynRMs for all SPPs show T_{rip} values ranging on average from 20% to 80% and even to 100% in SPP = 3. Generally, a higher ξ is followed also by a higher T_{rip}. Since the power factor of the machine is greatly related to ξ, a compromise in selecting a solution has to be made to obtain low T_{rip}. The T_{avg} value is also considered during the selection as one of the main aims of the selected SynRM candidate is to support the required rated power. It is worth noting that the selected candidates pointed by arrows do not necessarily support the globally minimum T_{rip} or globally maximum ξ among all the generated solutions; however, they satisfy the best combinations of high ξ, low T_{rip}, and high T_{avg} to support the rated power at a same time.

4.2 SynRMs` Dimensions and Structures

The selected candidates among 1500 generated solutions are reported in Table 4-1, which also shows the optimized variables; Figure 4-2 illustrates the optimized SynRM structures.

Table 4-1: Optimized design variables.

Variables	Normal rotor			Cut off rotor		
	SPP = 2	SPP = 3	SPP = 4	SPP = 2	SPP = 3	SPP = 4
β (deg)	7.705	7.000	6.281	5.475	6.022	7.006
k	0.817	1.000	0.788	0.927	0.863	0.835
γ (deg)	135.66	135.00	135.81	135.30	135.57	135.72
S_{1d} (mm)	1.775	1.521	1.769	2.019	1.986	2.035
S_{2d} (mm)	1.740	1.861	3.876	3.160	2.753	4.115
S_{3d} (mm)	3.551	3.638	2.478	3.657	4.553	3.040
S_{4d} (mm)	3.655	3.840	3.333	3.286	3.618	3.393
W_{1d} (mm)	1.819	2.753	3.897	3.823	3.174	3.587
W_{2d} (mm)	3.863	2.870	3.400	2.968	4.362	2.677
W_{3d} (mm)	3.264	3.431	3.106	3.317	4.038	2.911
W_{4d} (mm)	4.0964	3.698	2.737	2.653	4.218	2.923

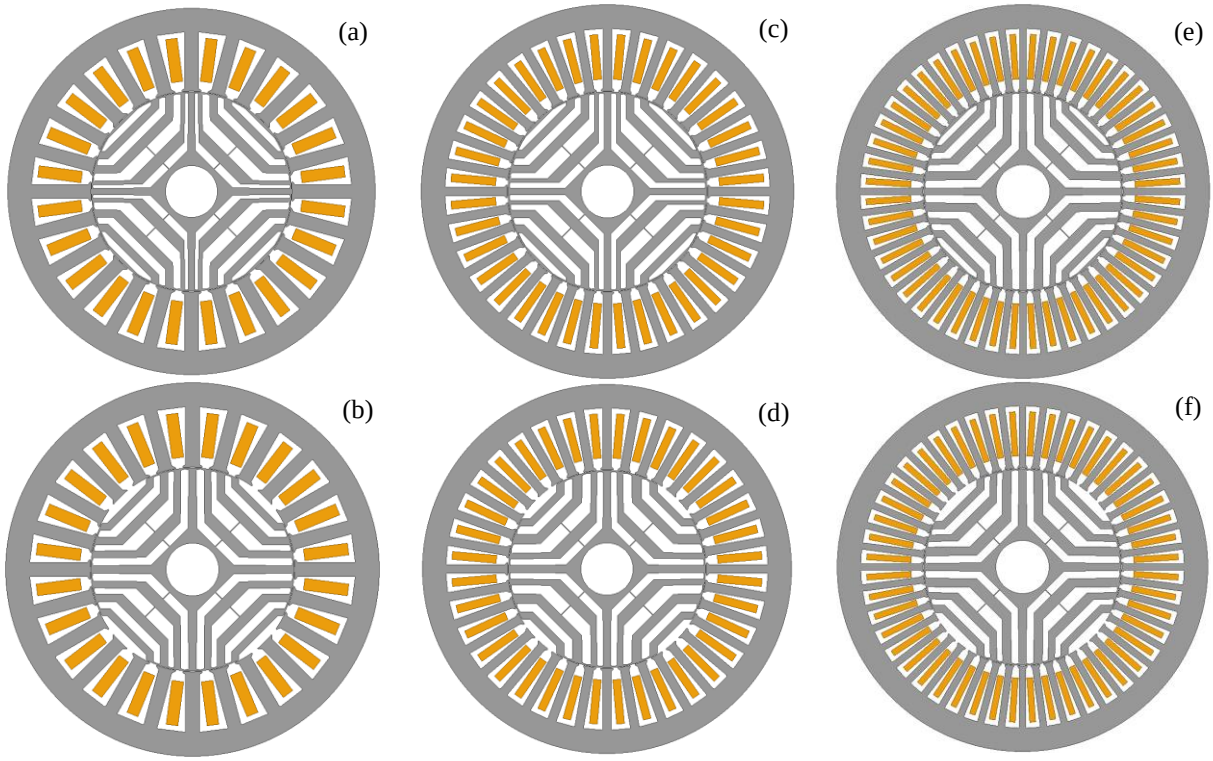

Figure 4-2: SynRM structures for (a) normal rotor (SPP = 2), (b) cut off rotor (SPP = 2), (c) normal rotor (SPP = 3), (d) cut off rotor (SPP = 3), (e) normal rotor (SPP = 4), and (f) cut off rotor (SPP = 4).

As seen in Table 4-1, all of the design variables are within the defined ranges and no violation is observed.

4.3 Finite Element (FE) Based Comparative Study

In this section, the electromagnetic performance of the optimally designed SynRMs under each SPP number are evaluated and compared using FEA to introduce a final design.

4.3.1 Inductance Analysis and Torque Profiles

The developed torque of a SynRM is directly a function of its d- and q-axis inductances (L_d and L_q). L_d, L_q, and ξ of each optimized SynRM are reported in Table 4-2 at rated current.

Table 4-2: inductances and saliency ratios of the SynRMs.

	Normal rotor			**Cut off rotor**		
SPP	**2**	**3**	**4**	**2**	**3**	**4**
L_d (mH)	508.8	564.2	554.8	487.9	558.6	534.1
L_q (mH)	61.5	65.8	65.4	58.3	64.0	61.5
ξ	8.27	8.57	8.49	8.37	8.72	8.69

Figure 4-3 shows the torque profiles of each optimized SynRMs and respective percentage torque ripple values at rated speed.

According to Table 4-2, L_q of the optimized SynRMs change from 58.3 mH for the cut off rotor SynRM (SPP = 2) to 65.8 mH for the normal rotor SynRM (SPP = 3). On the other hand, L_d may change from 487.9 mH to even 564.2 mH depending on the rotor structure and SPP. The smallest ξ is recorded for the SynRMs with SPP = 2, which explains the lowest developed torque in this SPP as illustrated in Figure 4-3.

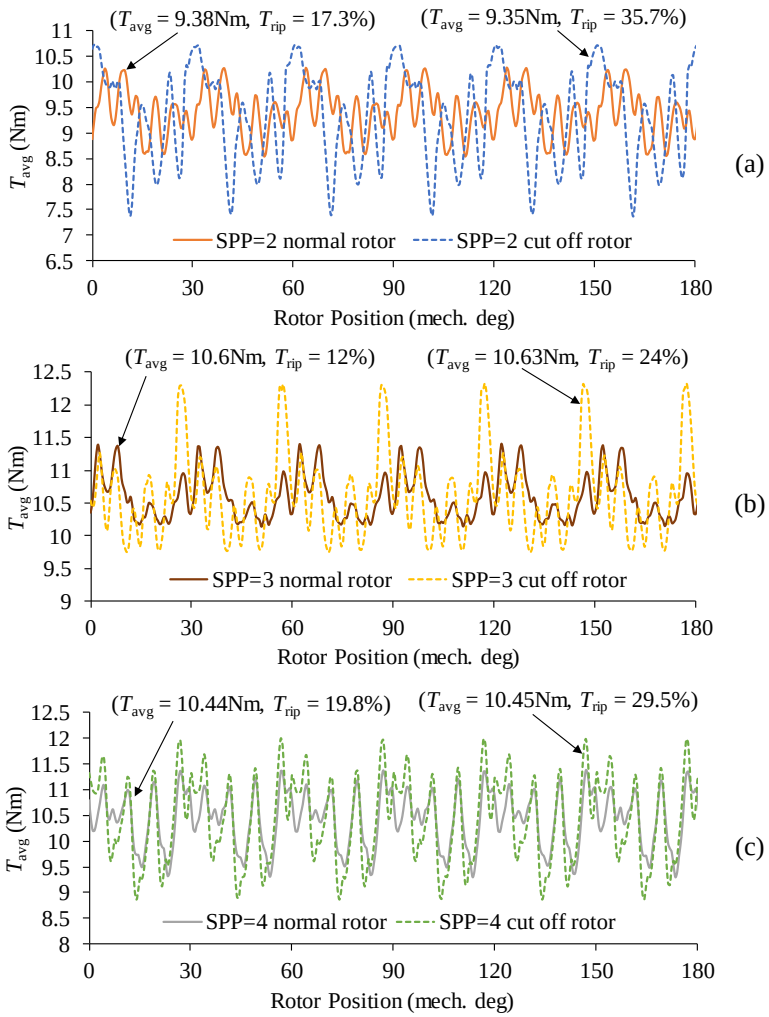

Figure 4-3: Torque profile versus rotor position in rated current for (a) SPP = 2 rotor structures, (b) SPP = 3 rotor structures, and (c) SPP = 4 rotor structures.

According to Figure 4-3, all of the normal rotor SynRMs show smaller T_{rip} compared to cut off rotors. For example, at least 18.4%, 12%, and 9.7% T_{rip} increments are seen for the cut off rotor designs with SPPs of 2, 3, and 4, respectively. In addition, SynRMs with SPP of 3 can easily support the required developed torque at rated speed, while SynRMs with SPP of 2 are incapable to do so. T_{avg} of SynRMs with SPP of 3 is much larger than its SPP = 2 counterparts and close to the desired average developed torque of 10.6 Nm.

4.3.2 Air-gap Flux Density and Harmonic Analysis

SynRMs inherently suffer from high harmonic content due to their highly anisotropic rotor structure that adversely affects their torque profiles and causes vibrations. The main indicator of the harmonic content of a SynRM is the air-gap flux density ($B_{\text{air-gap}}$). $B_{\text{air-gap}}$ of the optimized SynRMs are illustrated in Figure 4-4 at the rated operating point, while the fundamental component ($B_{1(\text{peak})}$) and the Total Harmonic Distortion (B_{THD}) are separately calculated and reported on each plot.

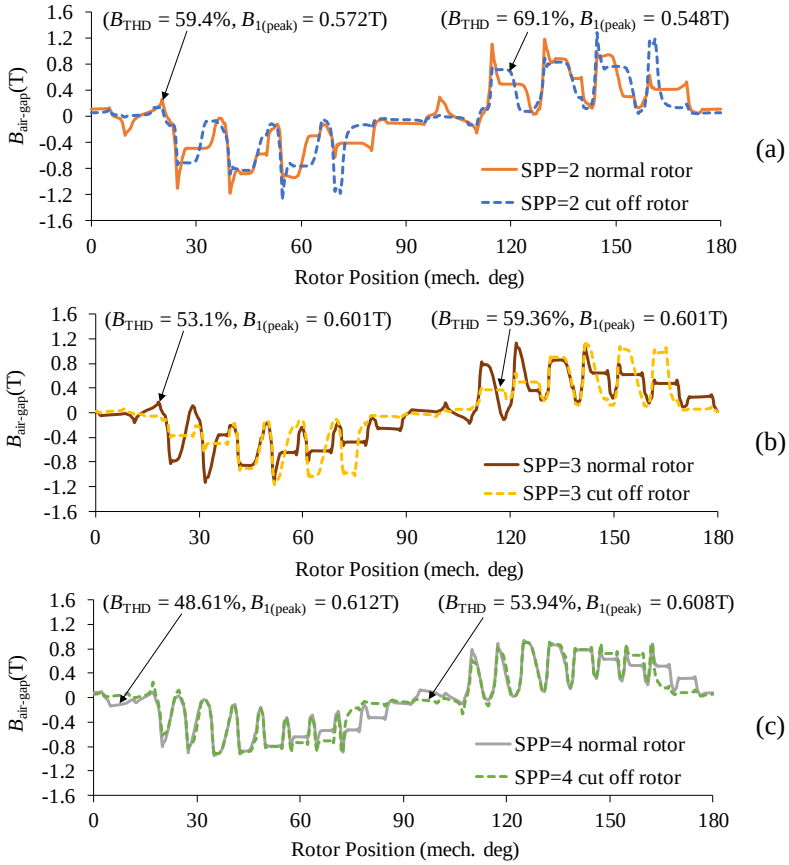

Figure 4-4: $B_{\text{air-gap}}$ versus rotor position in rated conditions for (a) SPP = 2 rotor structures, (b) SPP = 3 rotor structures, and (c) SPP = 4 rotor structures.

As seen, B_{THD} varies from 48.61% to even 69.1% depending on the machine's structure. In addition, the cut off rotor designs show a larger B_{THD} compared to normal rotor machines. For instance, at least 9.7%, 6.26%, and 5.33% B_{THD} increment is seen for the cut off rotor SynRMs

with SPPs of 2, 3, and 4, respectively, compared to the normal rotor SynRMs. Furthermore, the minimum $B_{1(peak)}$ of 0.548 T and 0.572 T are seen for the SynRMs with SPP of 2, which reconfirms why a much smaller developed torque is predicted for these SynRMs compared to the other ones.

4.3.3 Maximum Output Power

In order to extract the maximum developed torque/power in a wide speed range, the phases of the machines are fed by a variable frequency current source. Below the base speed, current magnitude and angle are set based on the MPF current angle control strategy, while above the base speed Voltage Current Limited Maximum Torque (VCLMT) control approach is employed. The maximum average torque capabilities versus speed are shown in Figure 4-5 (a). The maximum developed power capabilities of the optimized SynRMs versus speed are shown in Figure 4-5 (b) and According to Figure 4-5 (b), the maximum developed powers of SynRMs with SPP of 2 are equal to 885.9 W for normal rotor and 878.4 W for the cut off rotor cases. On the other hand, SynRMs with SPPs of 3 and 4 are capable to support nearly 1 kW at the rated speed. All optimized SynRMs are capable to support peak power above 1077 W, while the SynRMs with SPPs of 3 and 4 experience peak power at 1000 rpm and SynRMs with the SPP of 2 show peak power at 1200 rpm. SynRMs with SPP of 2 are capable to provide the rated power up to 1500 rpm, while the maximum speed in constant power speed region for other SynRMs is limited to 1400 rpm. The cut off rotor SynRMs consistently can support a higher output power as well as a wider constant power speed region compared to the normal rotor SynRM with the same SPP.

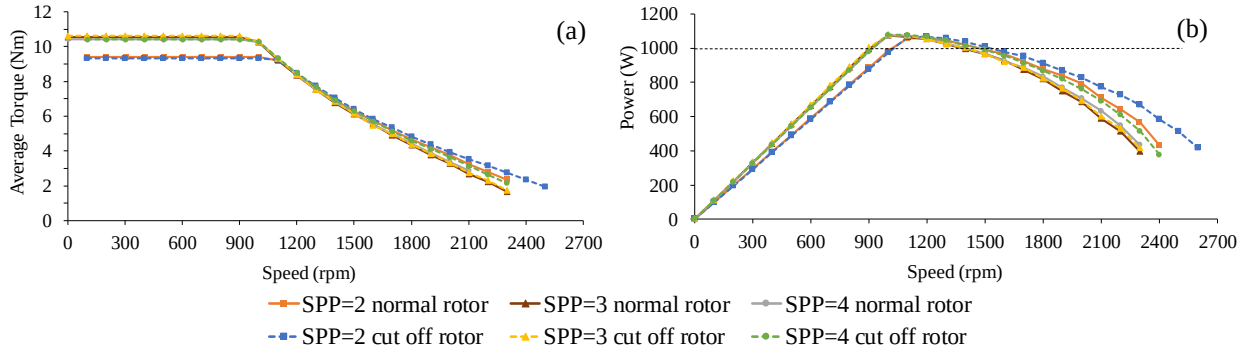

Figure 4-5: (a) Average torque and (b) maximum developed power comparison.

4.3.4 Core and Copper Losses

Core and copper losses are evaluated for each optimally designed SynRM in a wide speed range. For copper loss calculations only the winding's DC resistance is taken into account and the high frequency AC Joule losses are neglected. As the peak of the currents fed to the phases of all optimized SynRMs are equal and constant (I_{peak} = 5.35 A), the only component affecting copper losses is the phase resistance of each machine. Copper losses of the optimized SynRMs with SPPs of 2, 3, and 4 are equal to 154.6 W, 164.3 W and 159.9 W, respectively. FEA core losses calculations has been used and the variations of these losses are shown in Figure 4-6.

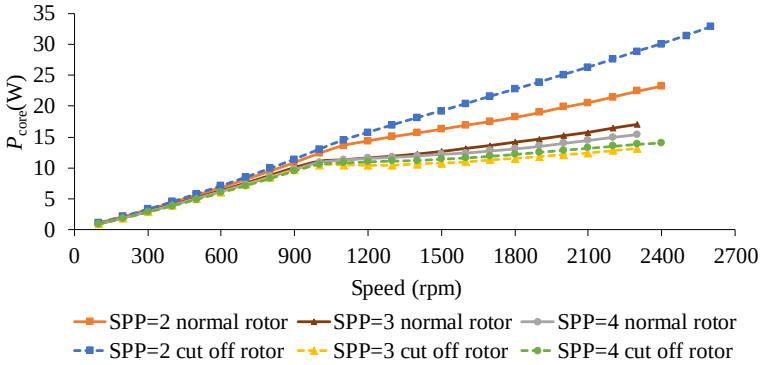

Figure 4-6: Core losses versus speed in the maximum developed powers.

According to Figure 4-6, the cut off rotor SynRMs with SPPs of 2 and 3 show the highest and lowest core losses at all operating speeds, respectively. For example at 2300 rpm cut off rotor SynRM with SPP = 2 shows core losses equal to 28.86 W, and cut off rotor SynRM with

SPP = 3 has core losses equal to 13.86 W. At base speed, all machines show core losses around 10 W except the cut off rotor SynRM with SPP = 2, which shows core losses around 11.39 W.

4.3.5 Efficiencies at Maximum Developed Powers

Using the evaluated copper and core losses and the developed output power, the efficiency of each design can be calculated over the entire operating speeds. The efficiency plots versus speed variations are shown in Figure 4-7. As seen, the efficiency of each optimized SynRM increases from 40% to 86% for SPPs of 3, 4 and up to 85.5% for SPP = 2. At the rated speed, all optimized SynRMs with SPPs of 3 and 4 can support an efficiency above 85%, while the efficiency of the SynRM with SPP = 2 (both normal and cut off rotors) is limited to 84%. However, the efficiency of the optimized SynRMs with SPP = 2 is larger than the other optimized SynRMs with SPPs of 3 and 4 at higher speeds. For example at 2300 rpm, the efficiency of the cut off rotor SynRM with SPP = 2 is 3.7% and 8.4% larger than the efficiency of the cut off rotor SynRMs with SPPs of 3 and 4, respectively.

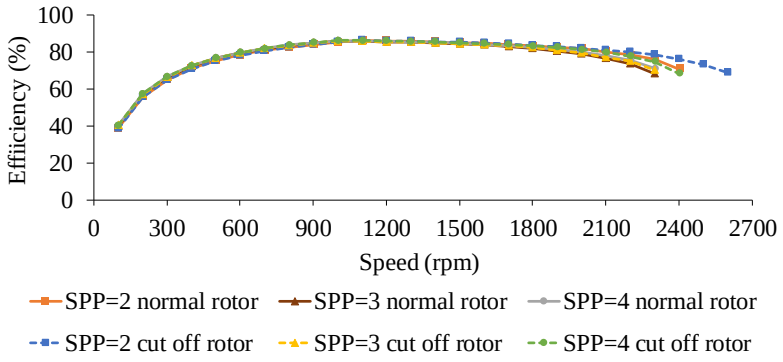

Figure 4-7: Efficiency versus speed in maximum developed powers.

4.3.6 Power Factor Values at Maximum Output Powers

For power factor calculations, phase angle difference between the fundamental components of phase voltage and current is considered. As is seen in Figure 4-8, all 6 optimized SynRMs have power factors between 0.78 (SPP = 2 normal rotor) and 0.79 (SPP = 3, 4 cut off rotor) up to

the base speed, which is close to the design requirement of 0.8. Power factor increases slightly until the peak power point and drops significantly as speed increases further. For example, the cut off rotor SynRM with SPP = 4 shows a power factor of 0.792 at 1000 rpm, which then decreases to even 0.28 at 2400 rpm.

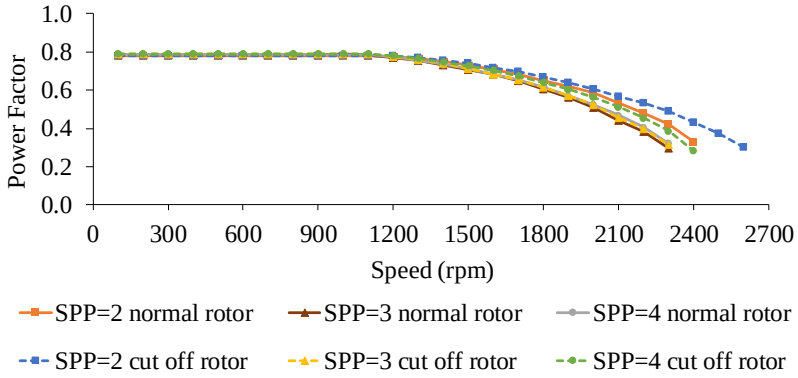

Figure 4-8: Power factor versus speed in maximum developed powers.

4.4 Mechanical Considerations of the Finally Selected SynRM

According to the analysis reported in this section, normal rotor SynRM with SPP = 3 is selected as the final design as it supports the rated power and desired efficiency at the base speed, and also posses minimized torque ripple compared to the other counterparts. Radial and tangential ribs are introduced even in the electromagnetic optimization of rotor structure of SynRMs to come close as possible to practical rotor structures with mechanical rigidity. However, the width of these ribs must be minimal to prevent any electromagnetic incapability. So, the rib widths are set to 0.5 mm, and a set of structural analyses are conducted to ensure that the ribs can withstand centrifugal forces at high speeds. Von-Mises stress analysis and deformation analysis are conducted at various operating speeds up to 2700 rpm, which is above the expected maximum speed of the machine in the rated power. Figure 4-9 shows the von-Mises stress and deformation distribution at 2700 rpm.

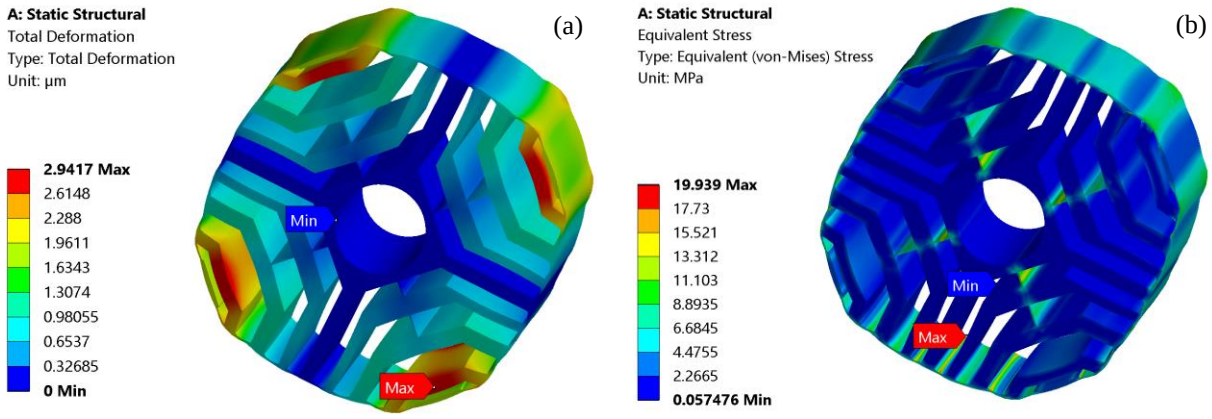

Figure 4-9: Exaggerated view (×1800) of (a) deformation and (b) von-Mises stress distribution for the final design in 2700 rpm.

According to Figure 4-9, it is clear that even at 2700 rpm the maximum possible deformation is only 2.94 μm at flux carrier 4, which is a small value when it is compared with the flux barrier and carrier widths and the machine's air-gap length of 350 μm. On the other hand, the maximum possible equivalent stress of 19.939 MPa occurs in the tangential rib of flux barrier 1, which is far below the yield strength of M19-29G lamination (around 400 MPa) used in the rotor structure of the designed SynRM.

4.5 Summary

Design optimization and performance analysis for SynRMs with different SPPs were conducted. It was seen how the performance of 4 pole SynRMs is affected for various slot numbers and rotor designs. It was shown that a SynRM with SPP of 2 could support a larger output power, efficiency, and power factor in high speed regions, however lacking performance around and below base speed. Furthermore, SynRMs with SPPs of 3 and 4 are superior in terms of these performance indicators at low speeds including base speed. In general, cut off rotor designs showed the higher saliency ratio and larger harmonic content compared to the normal

rotor structures. Structural analysis was conducted up to the maximum expected speed of the final design, and it was shown that no mechanical stress or deformation concerns may arise.

Chapter 5

Permanent Magnet-Assisted Synchronous Reluctance Machines

In this chapter, an FE-based rotor design optimization is conducted to come up with the optimal rotor geometry and magnet arrangements in a SynRM assisted with the ferrite magnets. As discussed in the previous chapters, a COF is defined to simultaneously reduce the torque ripple and increase the saliency ratio of the optimally designed SynRM, while the desired torque capability of the machine is always taken into account as well. To further improve the performance capability of the previously optimized SynRM, ferrite magnets are inserted into the rotor slots and the corresponding optimized arrangement of the magnets is found. A comparative electromagnetic study and mechanical stress analysis are carried out to predict the performance capabilities and operating limits of the designed SynRM and PMaSynRM.

5.1 Theory, Advantages and Challenges

As seen in the previous chapters, power factor and field weakening capability and torque density of the SynRM is still lagging behind with PM counterparts despite the other advantages. To mitigate these performance issues of a SynRM, adding PMs into the rotor slots is beneficial [47]. The widely accepted method is to insert the PMs along q-axis to saturate the radial ribs resulting uninterrupted flux passage along d-axis. The radial ribs along q-axis get saturated partly due to PM flux [48] and this PM flux linkage is effectively rotates the flux linkage vector out of phase with the current vector resulting the voltage vector to rotate towards the current vector as shown in Figure 5-1. The end result is the improved power factor [49], [50] and exceptional field weakening capability [51], [52] compared to SynRM.

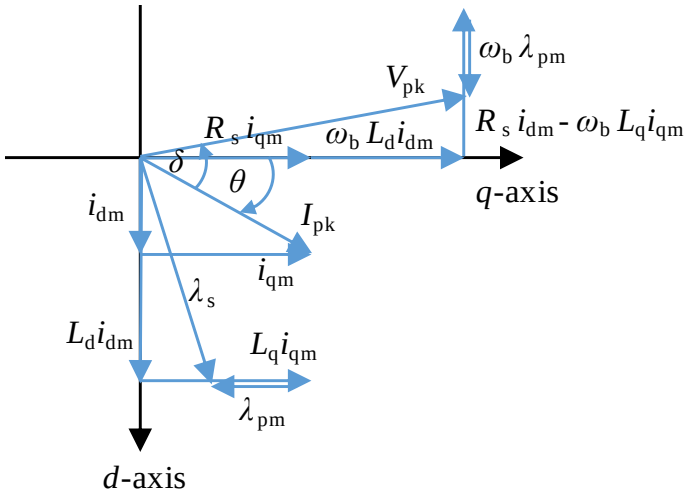

Figure 5-1: Voltage-current vector diagram of a PMaSynRM.

The torque equation of PMaSynRM as stated in (5.1), has an additional torque component which is produced by the added PM where λ_{pm} is the flux linkage due to PM.

$$T = \frac{3}{2} P\left[(L_d - L_q) i_d i_q + \lambda_{pm} i_d\right] \tag{5.1}$$

However the reluctance torque component in a PMaSynRM is still the dominant term in the torque production and it is the main indicator to distinguish this machine from a PMSM in which the magnetic torque component is the most dominant torque production element [53]. PMaSynRM can produce the same torque with a relatively low current magnitude compared to SynRM due its inherently larger power factor as the resulting decreased power factor angle as shown in Figure 5-1. Accordingly, the increased torque density can be mentioned as a principle advantage of PMaSynRMs compared to SynRMs [49], [54], [55].

Despite the several advantages, adding PM will introduce some performance drawbacks and design challenges. For example, short circuit fault current cannot be avoided for any non-zero speeds due to the generated back-EMF and this can be addressed by the use of a special motor drive for safety critical applications [56]. However, the use of ferrite magnets can reduce

the short circuit fault impacts as they produce a relatively low remnant flux density [57], [58] but with the risk of demagnetizing problems [59]. PMaSynRMs designed for high speed applications may need additional attention when deciding the dimensions for radial ribs as they should withstand the centrifugal forces occur at higher speeds, but no bonding of the magnets are needed as in the surface mounted PMSMs [60]. When it comes to securing the magnets within the designated slots, they are prone to slide across if proper migratory measurements are not taken into account. The decoupled torque control can also be challenging, since d- and q-axis inductances are the functions of air-gap flux [61] contributing to the major reluctance torque component in all operating points.

Among many options, neodymium [62] and ferrite [63] magnets are widely popular when it comes to magnetization of rotor structures of all machine types. But, despite the unbeatable performance enhancement offered by rare earth magnets such as neodymium, due to high recorded price in recent years [64] and limited supply [65], industries are leaning more toward on widely available low cost ferrite magnets. In addition, cheaper ferrite magnets offer better efficiencies than neodymium magnets at higher temperatures due to high Curie temperature [66]. One of the main challenges of designing a PMaSynRM is to find the optimal placement and dimension of the magnets used in the rotor structure as the performance of the machine is highly affected by the magnet arrangements [67], [68]. The magnet dimensions have been determined in [47], [62], [69], [70] to improve the performance of PMaSynRMs, however in [62] the magnet dimensions and placements are not optimized, in [47] only limited magnet width options are considered, in [69] the number of design variables to define magnet dimensions and sizes is limited and machine’s developed torque improvement is not considered, and in [70] the power

factor of machine is maximized using the optimized magnet dimensions while the developed torque and torque ripple betterment are not well considered.

As a solution to the above listed issues, the optimal dimensions of ferrite magnets in PMaSynRM are obtained in this thesis considering the torque ripple minimization and developed torque maximization by solving a corresponding COF. Meanwhile, the saliency ratio of PMaSynRM is already maximized during the initial SynRM design optimization. Among the encouraging optimized magnet arrangements, the one supporting the widest speed range, highest developed torque, and minimized torque ripple for the designed PMaSynRM is selected for machine fabrication steps.

5.2 Proposing Methodology to Obtain Optimal Magnet Dimensions

The same optimally designed rotor structure of 36-slot (SPP=3) SynRM is used for the PMaSynRM design optimization and analysis. The optimized magnets arrangement is obtained using a newly defined COF and based on the operating limits of a non-optimized PMaSynRM and performance parameters of the optimized SynRM.

5.2.1 Non-Optimized PMaSynRM

A ferrite magnet (Y30) with the remnant flux density of 0.4 T is used in the rotor structure of the analyzed PMaSynRMs. For the non-optimized PMaSynRM (PMaSynRM-1), whole of the available rotor slot space along the q-axis is filled up with the ferrite magnets. The rotor structure of PMaSynRM-1 is shown in Figure 5-2.

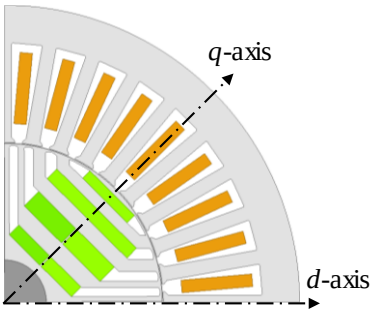

Figure 5-2: The structure of a non-optimized PMaSynRM (PMaSynRM-1).

Table 5-1 shows the performance characteristics of PMaSynRM-1.

Table 5-1: Operating characteristics of PMaSynRM-1 at rated speed.

L_d (mH)	L_q (mH)	ξ	T_{rip} (%)	T_{avg} (Nm)
564.9	77.1	7.32	28.5	12.12

Figure 5-3 shows the transient torque profile of optimized SynRM versus PMaSynRM-1 in the rated operating condition.

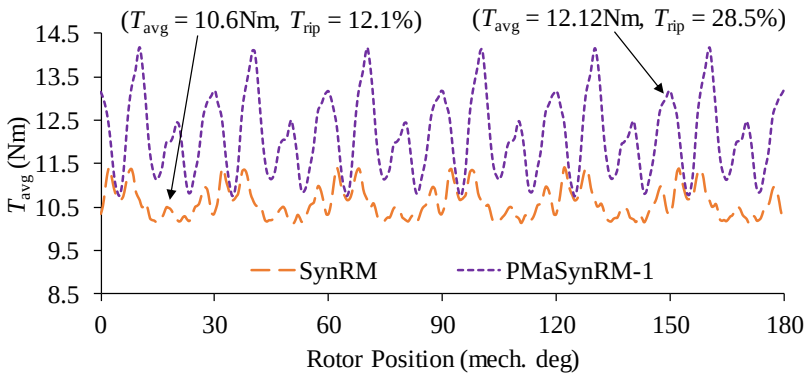

Figure 5-3: Torque profiles of optimized SynRM and PMaSynRM-1 versus rotor position.

According to Table 5-1 and Figure 5-3, the average developed torque and torque ripple of PMaSynRM-1 are 14.3% and 16.4% larger than the optimized SynRM, respectively. However, the saliency ratio of PMaSynRM-1 is 1.25 smaller than the optimized SynRM. This analysis shows that adding PMs into the rotor slots can help the power capability of PMaSynRM to get significantly improved compared to the designed SynRM, however as the additional cogging torque is introduced so the torque ripple of PMaSynRM-1 becomes larger than the optimally

designed SynRM. In addition, as the rotor structure of SynRM was initially optimized to maximize the machine's saliency ratio, as such the q-axis flux path of the SynRM was already defined in a way to make this flux path including the radial ribs and tooth tips to be saturated. Once the PMs are added into the rotor slots, the provided flux supported by the newly added PMs opposes the original q-axis flux lines so the q-axis flux path gets less magnetized and the q-axis inductance of PMaSynRM-1 becomes larger than the optimized SynRM with a saturated q-axis flux path. This issue causes the saliency ratio of the PMaSynRM-1 to become smaller than SynRM (only in the rated operating point).

5.2.2 Model for Optimization

At this point the maximum average torque possible and the minimum torque ripple value possible are known for PMaSynRM. Hence the lengths of the magnets can be optimized by easily defining additional variables as shown in Figure 5-4 and the new COF as stated in (5.2).

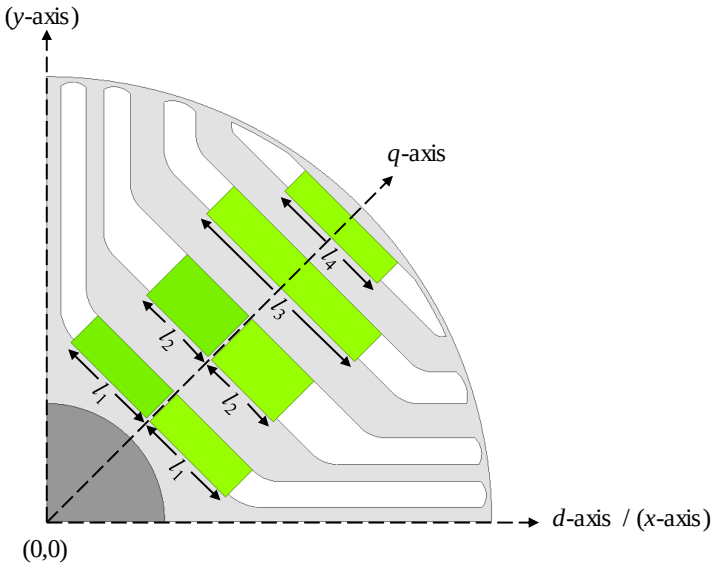

Figure 5-4: Optimized PMaSynRM's structure including the design variables.

$$\min\left(\left[T_{\text{avg}} - T_1\right]^2 + \left[T_{\text{rip}} - T_{\text{rip}_1}\right]^2\right) \tag{5.2}$$

A similar GA optimizer used in SynRM optimization steps is employed to find the solutions of the new defined COF (5.2) considering the design variables ranges given in Table 5-2 and required average developed torque and torque ripple.

In (5.2), T_1 is the average developed torque seen in PMaSynRM-1 once all of rotor slots along the q-axis are filled up with the magnets and T_{rip1} is the torque ripple seen in the optimized SynRM once no magnet is used in the rotor structure. In defining T_1 and T_{rip1}, it is assumed to find the optimal PM dimensions for the optimized PMaSynRMs in a way to simultaneously consider the operating performance advantages of both SynRMs and PMaSynRMs.

Table 5-2: Magnet length ranges.

Variable	Min	Max
l_1 (mm)	0	13.05
l_3 (mm)	0	34.06
l_2 (mm)	0	15.93
l_4 (mm)	0	19.09

5.2.3 Optimized PMaSynRMs

Based on the defined COF (5.2), design variables ranges in Table 5-2, and 50 generations of GA-based optimization runs, more than 1500 generated solutions are extracted. Figure 5-5 shows the saliency ratio, developed torque, and torque ripple values of the generated solutions. PMaSynRM-2 and PMaSynRM-3 are selected among the generated candidates as they both support the highest developed torques, promising torque ripples, and large saliency ratios.

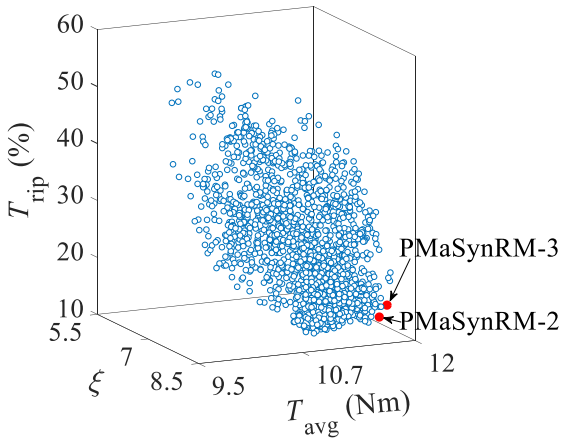

Figure 5-5: Saliency ratio, torque ripple, and average developed torque of the generated solutions in the rated operating point.

The structures of PMaSynRM-2 and PMaSynRM-3 showing the magnet arrangements are depicted in Figure 5-6.

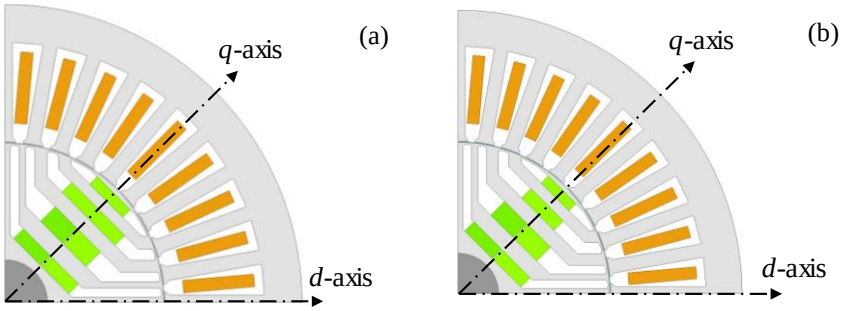

Figure 5-6: Structure of the optimized PMaSynRMs, (a) PMaSynRM-2, and (b) PMaSynRM-3.

The design variables and operating parameters of the extracted optimized PMaSynRMs are separately reported in Table 5-3 for comparison purposes. According to Table 5-3, all of the design variables are within the provided ranges and the total magnet weights of PMaSynRM-2 and PMaSynRM-3 are 221 g and 257 g lighter than PMaSynRM-1 with the total magnet weight of 714.55 g, respectively. In addition, the saliency ratios of PMaSynRM-2 and PMaSynRM-3 are both 0.44 and 0.67 larger than PMaSynRM-1, respectively.

Table 5-3: Design variables and parameters of optimized PMaSynRMs.

Variable/Parameter	PMaSy	PMaSynRM-3
l_1 (mm)	11.50	12.24
l_2 (mm)	9.39	9.99
l_3 (mm)	22.55	14.32
l_4 (mm)	14.07	12.43
ξ	7.74	7.97
L_d (mH)	568.1	571.6
L_q (mH)	73.4	71.7
T_{rip} (%)	12.8	15.1
T_{avg} (Nm)	11.89	11.89
Total magnet weight (g)	493.56	457.14

Figure 5-7 shows the torque profiles of PMaSynRM-2 and PMaSynRM-3 versus rotor position in the rated operating point.

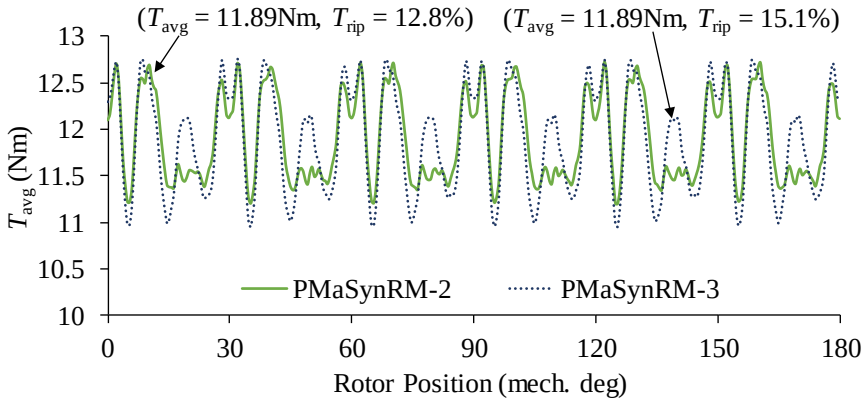

Figure 5-7: Torque profiles of PMaSynRM-2 and PMaSynRM-3 versus rotor position.

Both Figure 5-7 and Table 5-3 demonstrate that PMaSynRM-2 and PMaSynRM-3 possess 15.7% and 13.4%, smaller torque ripple than the PMaSynRM-1, respectively, and with the expense of only 1.9% developed torque reduction. This analysis shows that finding an optimal

placement of magnets in PMaSynRMs may support an improved performance characteristics for the designed machine with a significantly smaller size of magnets used in the rotor structure.

5.3 Finite Element (FE) Based Comparative Study of SynRM and PMaSynRMs

In this section, an FE-based comparative study is conducted to compare the predicted electromagnetic performance and capabilities of the optimized SynRM, PMaSynRM-1, PMaSynRM-2, and PMaSynRM-3.

5.3.1 Maximum Output Power

To predict the power capabilities of designed SynRM and PMaSynRMs, the MPF current angle control method is used for the below base speed operating region and VCLMT method is employed for the Field Weakening (FW) region. For all of the simulation analysis of this section a variable frequency current source is used for the phase excitation of machines in ANSYS-Maxwell. Figure 5-8 (a) shows the maximum average torque capability and Figure 5-8 (b) shows the output power capability comparison in a wide speed range.

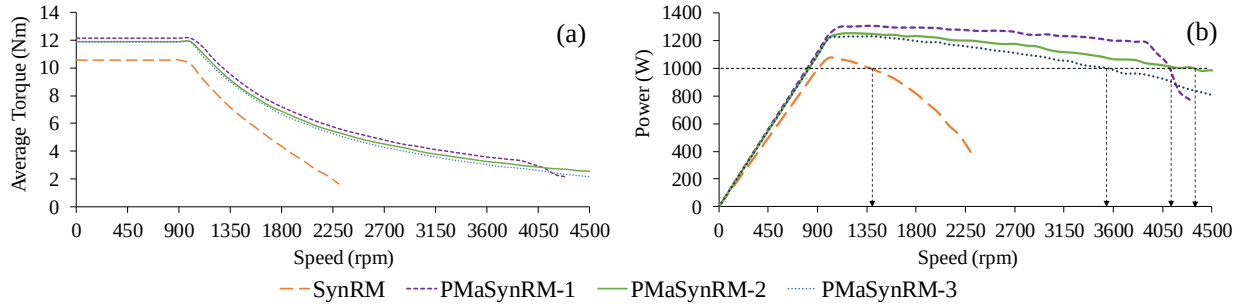

Figure 5-8: (a) Average torque and (b) maximum developed power comparison.

As seen in Figure 5-8 (b), not only adding PMs improves the output power of PMaSynRMs compared to the SynRM in the rated speed of 900 rpm, but also significantly widens the FW region of the designed machines. The peak power of optimized SynRM is 1075 W occurring at 1000 rpm, while the peak power of PMaSynRM-1, PMaSynRM-2, and PMaSynRM-3 are 1308

W, 1254 W, and 1232 W, respectively. The maximum speed in which the rated power can be fulfilled for SynRM, PMaSynRM-1, PMaSynRM-2, and PMaSynRM-3 are 1383 rpm, 4113 rpm, 4329 rpm, and 3541 rpm, respectively. The main reason of a sudden power drop for PMaSynRM-1 after 4000 rpm is its large harmonic content which already showed its presence in high torque ripple of PMaSynRM-1 compared to the other three machines.

5.3.2 Efficiencies at Maximum Output Powers

To predict the efficiency of the designed machines, (5.3) is used. In (5), P_{out}, P_{cu}, P_{core}, and P_{mech} show the output power, copper, core, and mechanical losses, respectively. Mechanical losses are the combination of friction, windage, and bearing losses measured in the actually built SynRM versus speed changes, while the other power components are extracted using FEA in the correspond speed and excitation. The efficiency plots versus speed changes are illustrated in Figure 5-9.

$$Eff\,(\%) = \frac{P_{out}}{P_{out} + P_{cu} + P_{core} + P_{mech}} \times 100 \tag{5.3}$$

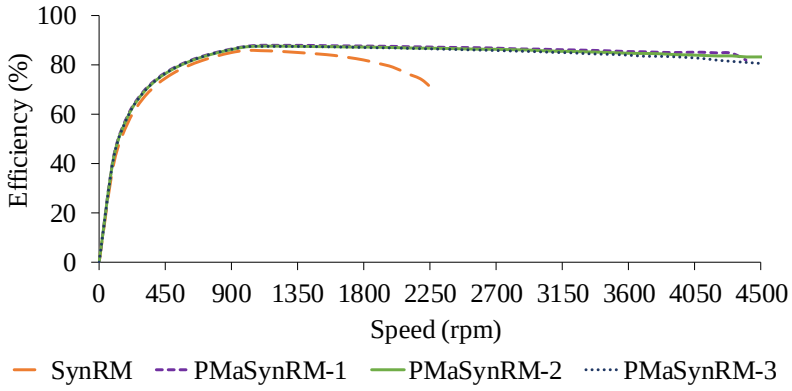

Figure 5-9: Efficiency comparison in a wide speed range.

As seen, the efficiencies of designed PMaSynRMs are significantly larger than the optimized SynRM in a wide speed range. For instance, the peak efficiency of SynRM is 85.98% occurring at 1000 rpm, while the peak efficiency of PMaSynRM-1, PMaSynRM-2, and

PMaSynRM-3 are 88.03%, 87.67%, and 87.50%, respectively. The efficiency of SynRM may drop to below 70% in 2250 rpm, while the efficiency of PMaSynRM-1, PMaSynRM-2, and PMaSynRM-3 are still above 85.19%, 83.6%, and 84.09%, respectively, in their corresponding maximum speed supporting the rated output power of 1 kW.

5.3.3 Power Factors at Maximum Output Powers

The fundamental components of voltage and current waveforms are used to predict the power factor capability of the designed machines in a wide speed range. The corresponding power factor plots are presented in Figure 5-10.

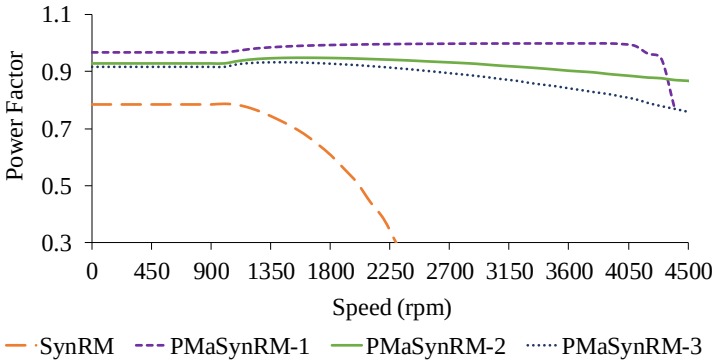

Figure 5-10: Power factor comparison in a wide speed range.

The significant contribution of adding PMs into the rotor slots of PMaSynRMs for power factor improvement objectives is clearly seen in Figure 5-10, in a wide speed range. Up to the base speed, the power factor may be improved from 0.77 in SynRM to above 0.95, 0.92, and 0.91 for PMaSynRM-1, PMaSynRM-2, and PMaSynRM-3, respectively. In addition, the peak power factor of SynRM, PMaSynRM-1, PMaSynRM-2, and PMaSynRM-3 are 0.78, 1, 0.95, and 0.93, respectively. It is worth noting that all of the designed machines except PMaSynRM-1 show a lagging power factor in their entire operating speeds. The power factor of PMaSynRM-1 is either lagging or unity up to 4000 rpm, while after this speed the machine shows a leading power factor.

5.3.4 Saliency Ratio and Torque Ripple

The saliency ratio and torque ripple values of designed SynRM are compared with one of the optimized PMaSynRMs, i.e., PMaSynRM-2 in various excitation levels and current angles. In order to make the explanation and analysis easier to follow, two new parameters are defined as follows.

$$R_{\text{sal}} = \frac{\xi_{\text{PMaSynRM-2}}}{\xi_{\text{SynRM}}} \tag{5.4}$$

$$R_{\text{rip}} = \frac{T_{\text{rip-PMaSynRM-2}}}{T_{\text{rip-SynRM}}} \tag{5.5}$$

Figure 5-11 shows R_{sal} and R_{rip} variations versus current angle and current peak changes.

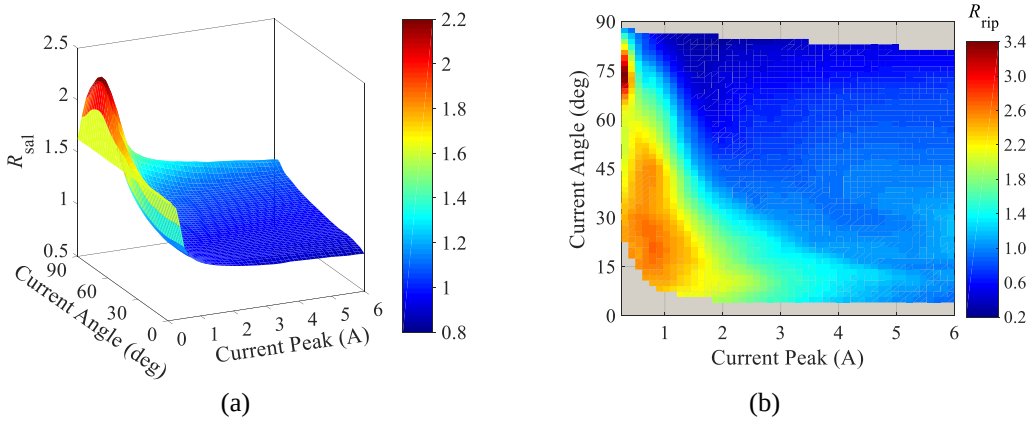

Figure 5-11: Saliency ratio and torque ripple comparison, (a) R_{sal}, and (b) R_{rip}.

According to Figure 5-11(a), it is seen that the saliency ratio of PMaSynRM-2 is not always smaller or larger than the SynRM with a similar rotor. In other words, adding PMs into the rotor structure does not necessarily increase the saliency ratio for a PMaSynRM as was discussed in [62], [71]. The behavior of saliency ratio for a PMaSynRM in comparison with a SynRM depends on the current peak and current angle in which the saliency ratios are assessed. For instance, in small current peaks (below 1.5 A) the saliency ratio of PMaSynRM-2 is

generally larger than SynRM, and this difference gets more significant up to 2.2 times in current angles above 60°. In larger current peaks (above 2 A) and current angles below 45°, this situation gets reversed and the saliency ratio of PMaSynRM-2 becomes smaller than the designed SynRM. As seen in Figure 5-11(b), a fixed behavior comparison is not observed between the torque ripples of PMaSynRM-2 and SynRM and the torque ripple of each machine may actually be larger or smaller than the other one depending on the operating current excitation. For example, in low current peaks (below 1.5 A) the torque ripple of PMaSynRM-2 may be significantly larger than SynRM, while in the current peaks above 2 A and current angle above 45° the torque ripple of SynRM gets even 5 times larger than PMaSynRM-2. It is worth noting that the grey areas in Figure 5-11(b) correspond to R_{rip} values around zero.

5.4 Mechanical Considerations of the Finally Selected PMaSynRM

According to the comparative study presented in the section 5.3 and performance characteristics of designed SynRM and PMaSynRMs discussed in section 5.2, PMaSynRM-2 is selected as a final design for the mechanical stress analysis, fabrication, and experimental evaluation. PMaSynRM-2 may provide the widest speed range, lowest torque ripple, promising efficiency and high power factor with a reasonable amount of ferrite magnets used in its rotor structure.

One of the critical design aspects of SynRMs and PMaSynRMs is to ensure the mechanical rigidity of their rotor in high speed operating regions as there are relatively thin radial and tangential ribs assigned in their rotor structure. 4050 rpm and 2700 rpm are the maximum operating speeds that PMaSynRM-2 and SynRM may be tested in the lab, respectively, considering the experimental loading capabilities and expected meaningful output power in FW region. Mechanical aspects analysis is conducted in this section using ANSYS-Workbench. The

maximum Von-Mises stress and deformation observed in the rotor structure of SynRM and PMaSynRM-1 versus speed changes are shown in Figure 5-12.

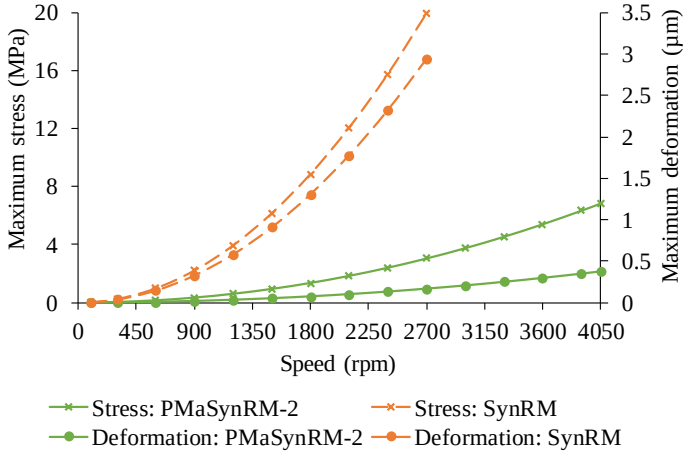

Figure 5-12: Maximum Von-Mises stress and deformation analysis versus speed changes for the designed SynRM and PMaSynRM-2.

According to Figure 5-12, both SynRM and PMaSynRM-2 show less than 20 MPa maximum Von-Mises stress versus speed changes which is noticeably smaller than the yield strength of M19-29G (400 MPa). In addition, the maximum deformation observed in the rotor of SynRM and PMaSynRM-2 is limited to at most 3µm which is a negligible dimension considering the air-gap length of 0.35 mm and radial and tangential ribs of 0.5 mm. Furthermore, it is also demonstrated that adding PMs may improve the mechanical strength of rotor for PMaSynRM-2 as both maximum Von-Mises stress and deformation of this machine are significantly smaller than SynRM at same speeds. As an example, the Von-Mises stress and deformation distributions for the rotor of SynRM and PMaSynRM-2 in speed of 2700 rpm are shown in Figure 5-13.

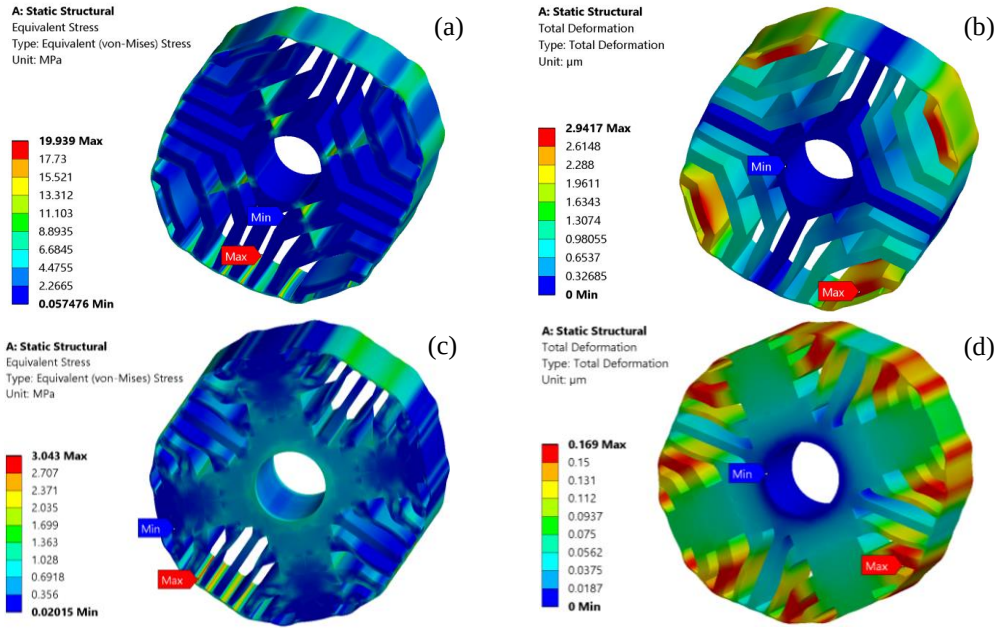

Figure 5-13: Exaggerated mechanical stress and deformation distribution, (a) Von-Mises stress-SynRM, (b) Deformation-SynRM, (c) Von-Mises stress-PMaSynRM-2, and (d) Deformation-PMaSynRM-2.

As seen in Figure 5-13, the maximum Von-Mises stress is seen in the tangential ribs for both SynRM and PMaSynRM-2, however, this stress value in PMaSynRM-2 is only 15.2% of the value seen in SynRM mechanical analysis. The maximum deformation is seen in the fourth flux carrier along q-axis and third flux carrier along d-axis for SynRM and PMaSynRM-2, respectively. The maximum deformation of PMaSynRM-2 is only 5.7% of what is expected for SynRM.

5.5 Summary

Design optimization of a 36-slot four-pole PM-assisted SynRM was conducted to find the optimal dimensions of ferrite magnets along q-axis to improve the average torque, power factor and wide speed range. For example selected PMaSynRM-2 improves average torque by 12.6%, power factor by 19.5% and constant power wide speed range by 213% compared to it`s SynRM version. Interestingly enough, the use of low cost ferrite magnets combined with salient behavior

of the machine can produce competitive performance to other PMSMs. Although the power factor is not a part of the optimization process, introduction of the magnets have greatly improved the power factor due to additional PM flux linkage. The best selected candidate, PMaSynRM-2 shows the importance of an optimization by being able to reduce the magnet weight by almost one third yet providing similar performance in terms of average torque, power factor and wide speed capability. And also it offers superior torque ripple reduction over PMaSynRM-1 (15.7% smaller) similar to SynRM.

Adding PM will not necessarily improve the saliency ratio, but due to the introduction of the additional PM flux linkage, average torque, power factor and wider speed range are greatly improved yet still being a salient machine. The mechanical aspects of the SynRM is also improved after introducing the magnets along q-axis as the deformation and stress of the rotor laminations got reduced by 94.25% and 84.74%, respectively.

Chapter 6

Machine Fabrication and Experimental Analysis

In this chapter, the sensitivity of SynRM performance toward a manufacturing tolerance is investigated. The optimized SynRM and PMaSynRM-2 are fabricated and the experimental analyses are presented to provide the actual operating capabilities of the tested machines. The same rotor and stator are used for PMaSynRM-2 with the only exception of added ferrite magnets along q-axis and different parts required to complete the test apparatus were built in house.

6.1 Stator, Rotor, and Fabricated SynRM and PMaSynRM

The stator and the rotor structures are made of the same M19-29G laminations and stacked transversally to obtain the required length. Stator lamination stack was welded prior to the winding process to prevent any deformations. During the simulation analysis the copper wire gauge of AWG 17 was used; however, for the actual winding a parallel configuration of AWG 20 copper wires were used due to the material unavailability and to help the end winding to be shorter in the actually wound stator. It is worth noticing that the effective cross sectional areas of the windings are nearly identical for the simulation analysis and built machine. Wound stator is shown in Figure 6-1(a). Since the stator laminations do not have any tight tolerances, the fabricated stator has nearly the same dimensions as in the simulations. However due to the extreme complexity in the rotor geometry and tight tolerances, the fabricated rotor is 0.25 mm smaller (radially) compared to the simulations. As a result of that the fabricated SynRM has an air-gap of 0.6 mm compared to 0.35 mm simulated air-gap value. To secure the rotor laminations

together, double split shaft collars were used with end plates at both ends. A few additional modifications were made to the rotor laminations prior to fabrication. For instance, every d-q axis flux barrier line intersection was filleted to increase mechanical rigidity and a key way and three holes in the middle of the rotor were introduced to align them when stacking. Those modifications were done carefully to cause minimal electromagnetic property changes in the rotor. Figure 6-1(b) shows the fabricated rotor of the optimized SynRM. The same wound stator and rotor have been used for the optimized PMaSynRM-2, while the ferrite magnets with the optimized dimensions are inserted into the rotor slots as shown in Figure 6-1(c).

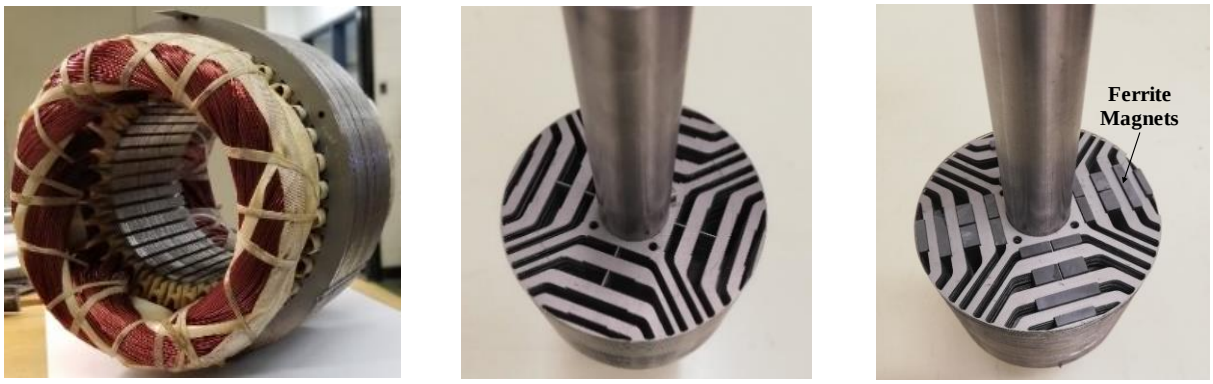

(a) (b) (c)

Figure 6-1: Machines' parts, (a) Wound stator, (b) SynRM's rotor, and (c) PMaSynRM-2's rotor.

6.1.1 Performance Sensitivity towards a Manufacturing Error

For the designed SynRM and PMaSynRM-2 of this thesis, the air-gap length has been set to be equal to 0.35 mm in the simulation studies. Any manufacturing error in the cutting of stator or rotor laminations may affect the performance characteristics of the fabricated machines. The sensitivity trends of average developed torque, saliency ratio, and power factor of the designed SynRM versus air-gap length increment from 0.35 mm to 0.7 mm are shown in Figure 6-2.

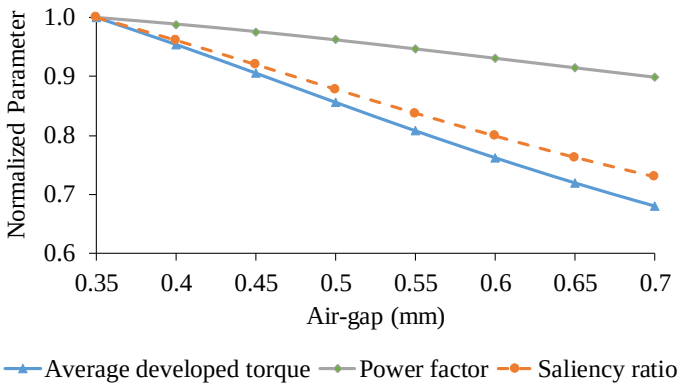

Figure 6-2: Average developed torque, saliency ratio, and power factor variations versus air-gap length changes.

As seen in Figure 6-2, the performance parameters of the optimized SynRM are all adversely affected versus air-gap length increment. Among the investigated parameters, the average developed torque and power factor of the machine show the highest and lowest sensitivities toward air-gap changes, respectively. According to Fig. 15, 32%, 27%, and 10% reductions are observed for the average developed torque, saliency ratio, and power factor of SynRM, respectively, once the air-gap changes from 0.35 mm to 0.7 mm.

6.2 Experimental Test Rig

A full-scale test rig, shown in Figure 6-3, is prepared to investigate the experimental performance of the designed SynRM and PMaSynRM-2 using a closed-loop FOC method as discussed in the previous section. A three phase power converter is used to provide the Pulse Width Modulated (PWM) signals to the machines' phases. The DC link voltage of the converter is supported by a three-phase rectifier included in the converter and the DC voltage level may be adjusted by a three-phase variac between the grid supply and the rectifier's input. A real-time digital simulator (RTDS) is used to assess the analog input, digital input and digital output signals using GTAI, GTDI and GTDO cards respectively to control the machine with a time step of 10 μs. A four-quadrant dynamometer is used to load the machine and a 20-Nm torque

transducer is utilized to measure the load. Rotor speed and position are measured using a 1000 CPR optical encoder.

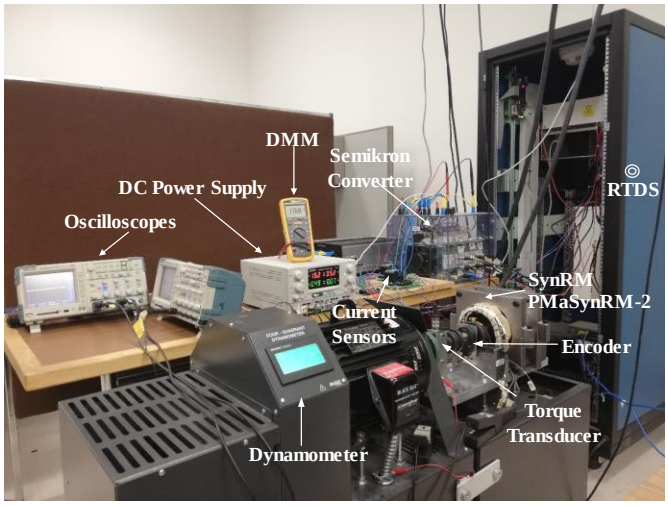

Figure 6-3: Experimental test rig

6.2.1 Back-EMF Analysis

The experimental back-EMF voltage waveform of PMaSynRM-2 in the rated speed is compared with the FE simulation analysis as illustrated in Figure 6-4. It is worth noticing that all of the simulation analyses reported in this section are based on the actual properties of the built machine including the updated air-gap dimension of 0.6 mm instead of 0.35 mm.

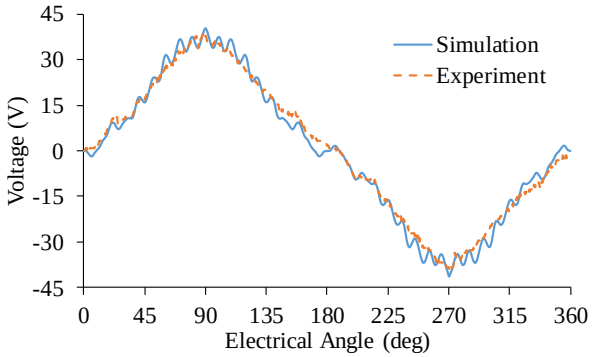

Figure 6-4: Back-EMF voltage waveform for PMaSynRM-2 at 900 rpm.

As seen in Figure 6-4, the experimental back-EMF voltage waveform is in well agreement with the FE simulation results. Using the Fast Fourier Transform (FFT) analysis, it is found that

the peaks of the fundamental components of simulated and experimental back-EMF voltages show less than 0.8 V difference and the third order harmonic component is the most dominant harmonic component in both simulation and experiment. To verify the harmonic content of the back-EMF voltages, the Total Harmonic Distortion (THD) of voltage waveforms are calculated and the values of 20.13% and 15.29% are recorded in the simulation and experiment, respectively.

6.3 Field Oriented Control of SynRM and PMaSynRM

Motor control techniques play a vital role when it comes to proper utilization of available resources based on the required performance outcomes. Essentially, these control techniques offer a speed control capability at a higher level and in the meantime excellent control over torque and field flux as the core controls to support the expecting outcome throughout the speed range. These core controls are generally coupled in nature for any type of motor except separately excited DC motor and often add complexities to the drive system. However during 1970s a breakthrough control technique was proposed by K. Hasse [72], and F. Blaschke [73] namely Field Oriented Control (FOC) as a linier torque control method to de-compose the stator phase currents to two orthogonal currents in rotor reference frame namely direct axis (d-axis) current and quadrature axis (q-axis) current for independent field flux and torque control respectively in an IM. This proposition was in fact encouraged by a separately excited DC machine as there is an additional winding only for excitation and armature winding for torque control and most importantly electro-mechanical separation of field and torque. Several torque control techniques have been introduced after the inception of FOC over the past few decades and can be categorized in few ways according to [74], [75]. For general understanding variable frequency motor control methods can be classified as in Figure 6-5. It is worth noticing that

linier torque control techniques such as FOC, DTC-SVM and DTC-FVM functions with voltage Pulse Width Modulations (PWMs) where the required voltages to the motor terminals are generated based on the control requirements determined by linear proportional-integral (PI) controllers using average measurements over each sampling time step.

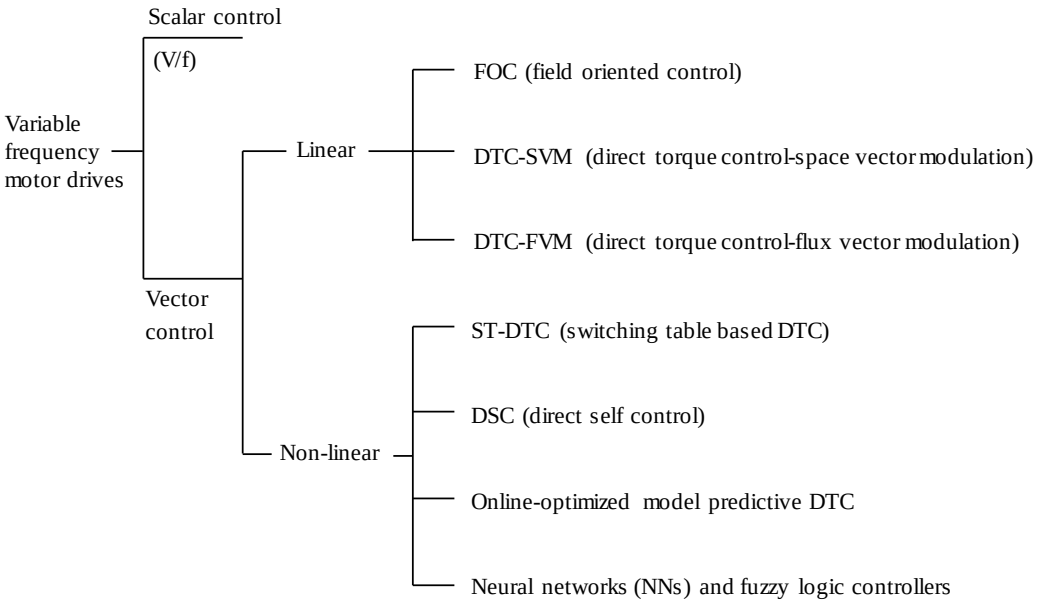

Figure 6-5: Variable frequency motor drives classification.

As in common practice a simple FOC topology is used in this thesis where, outer speed loop is followed by an inner torque loop and a separate field flux loop as shown in the Figure 6-6. Decoupled current controls are implemented to give additional robustness to the controller. Speed feed-back signal is measured using an incremental encoder with an index pulse (used for encoder calibration). It is worth noticing that L_d and L_q values can be determined for the fabricated machine by running the machine at rated speed without decoupling the current controllers and taking torque and current measurements at steady state and also using the approximated saliency ratio value from simulations based on actual measurements of the fabricated machine. The instantaneous rotor position after encoder calibration used for Park`s transformation is denoted by θ_r in Figure 6-6.

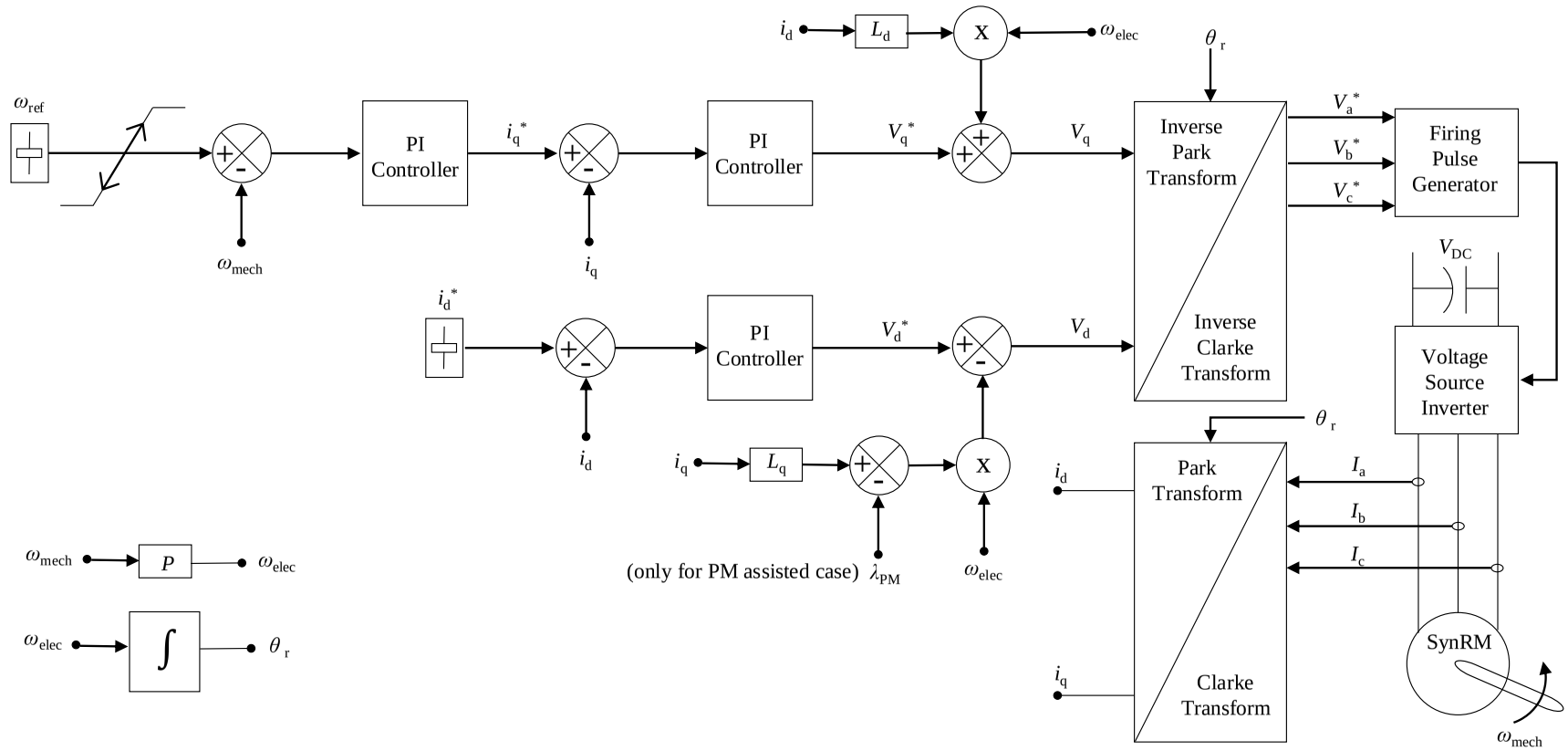

Figure 6-6: FOC of SynRM with decoupled current controllers.

6.3.1 Encoder Calibration

During the experimental analysis, rotor d-q reference frame was aligned in a way that q-axis is in phase with phase-A similar to simulation analysis. To do this PMaSynRM-2 was selected because of the back-EMF producing capability. When the rotor is fixed to ball bearings at both ends, and an encoder is mounted on the same shaft, the index pulse is coming at the same physical location at any speed. If the rotor is rotated using a prime mover, back-EMF voltages will be generated in phase windings to oppose the flux in the stator and can be mathematically expressed as in (6.1). Since the magnets are placed along q-axis of each rotor pole, one should expect the maximum flux linkage when the q-axis is aligned with the observing back-EMF phase voltage. If the back-EMF is assumed to have a sinusoidal variation with respect to rotor position, flux should have a cosine variation due to the mathematical relationship shown in (6.1).

$$BEMF \propto -\frac{d(\psi)}{dt} \tag{6.1}$$

In other words, flux should have a positive maximum when the back-EMF has a positive zero crossing and the encoder index pulse needs to be delayed to appear exactly on the back-EMF positive zero crossing to align the rotor q-axis with phase-A as shown in Figure 6-7.

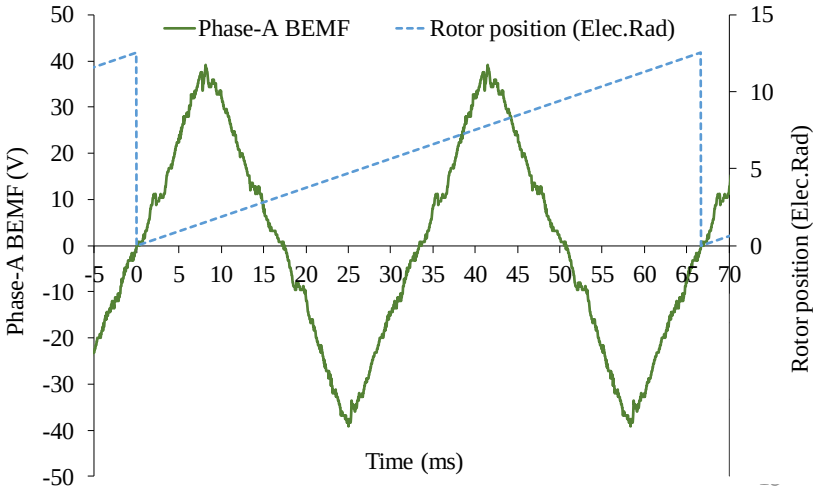

Figure 6-7: Rotor position after calibration.

It is also worth noticing that since this is a four-pole machine, within one physical rotation of rotor there are two full electrical cycles. Hence the rotor position accumulates up to 12.566 (4π) radians until it is reset by another index pulse.

6.3.2 PI Controller Tuning

As discussed in this section before, three different linear PI controllers were used for speed and d-q reference frame current loops as shown in Figure 6-6. Motor speed reference (ω_{ref}) and d-axis current references (i_d^*) are kept as user manipulating variables to test the machine at desired levels. Gains for each PI controllers were obtained using observation based tuning methods. The values of the finalized gains are given in Table 6-1.

Table 6-1: Tuned gain values of PI controllers.

	Speed	$\boldsymbol{i_d}$	$\boldsymbol{i_q}$
K_P	0.4	16	30
K_I (s)	45	0.01	0.01

It is also worth noticing that due to high magnetic saliency, gain values of the d- and q-axis current controllers are different unlike in the case of IPMSM where the saliency ratio is around unity and outer speed control loop is much slower than the inner i_q current loop.

6.3.3 Starting, Speed Transition and Steady State Performance of the Closed Loop Control System

This discussion is presented for the PMaSynRM-2 and is equally applicable for SynRM without any changes to PI controller gain values. As shown in Figure 6-6, ω_{ref} is applied using a ramp function to avoid sudden variations in the current loops. Figure 6-8(a) and (b) shows the speed response and stator three phase currents at starting to a ω_{ref} of 150 rpm under no load conditions respectively. As can be seen in the Figure 6-8(a), the actual rotor speed is in a good

agreement with the reference signal. It needs to be highlighted even under no load condition, small i_d^* current should apply to support the air-gap flux in both SynRM and PMaSynRM-2 scenarios as to create the required air-gap flux. For this specific case, i_d^* was kept at 0.85A and q-axis current reference (i_q^*) was determined by the controller to support mechanical and friction losses and settled around 0.7A resulting a phase peak current of 1.1A.

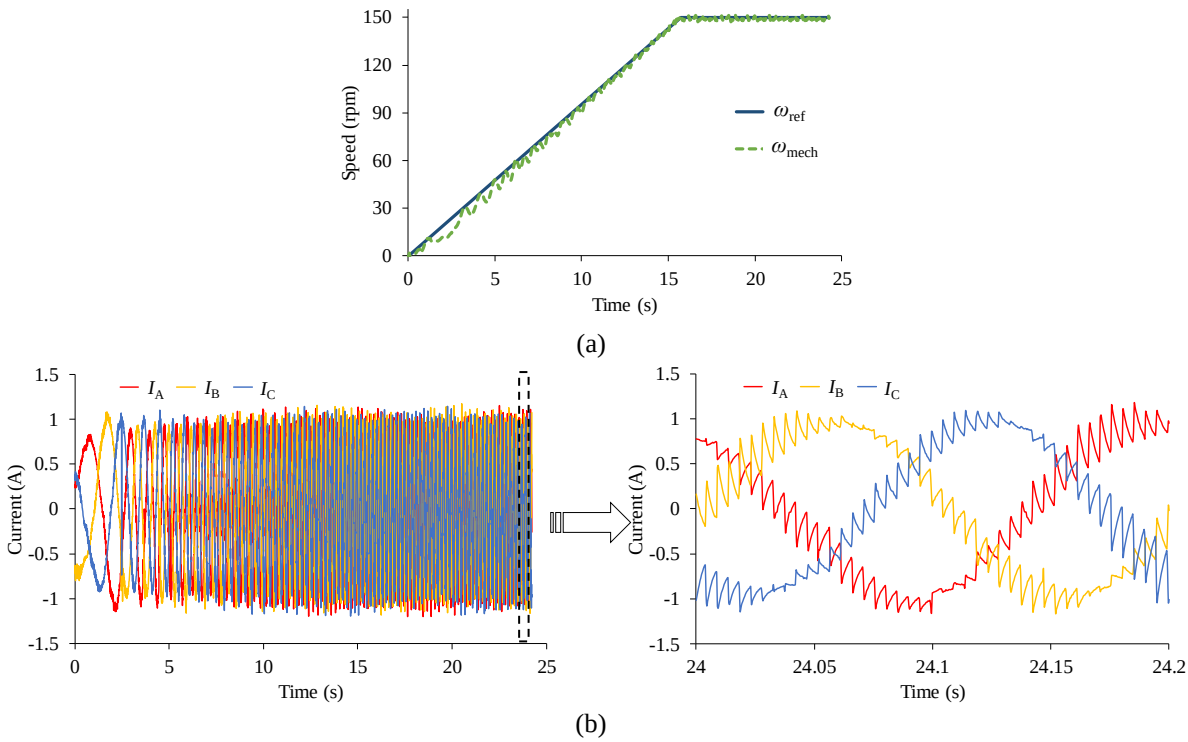

Figure 6-8: PMaSynRM-2 starting (a) speed response, and (b) phase currents.

After motor gained the initial speed reference, motor can be brought up to the rated speed by changing only the speed reference. Loading was done using a four-quadrant dynamometer and with a step of 0.5 Nm until the maximum torque value is achieved while increasing the i_d^* simultaneously to rated value, which in this case is 1.91 A. Figure 6-9 shows the speed transition under full load condition from 450 rpm to 600 rpm. As seen, Figure 6-9 shows a reasonable agreement between the reference and the actual speed with minimized error.

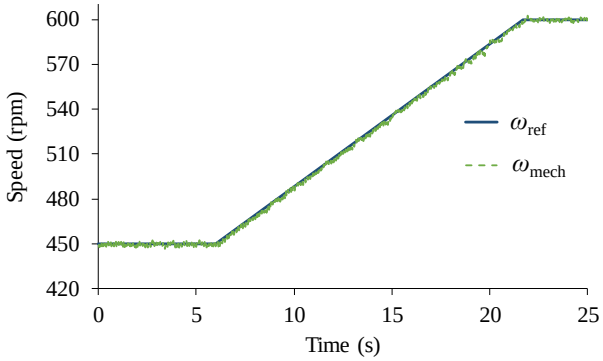

Figure 6-9: Speed transition of PMaSynRM-2 from 450 rpm to 600 rpm under full load condition.

A solid steady state performance throughout entire speed range is the main target as all the measurements are taken at steady state. Figure 6-10 shows the steady state rotor speed, d-q reference frame currents (i_d and i_q) and voltage values (V_d and V_q) under full load at rated speed.

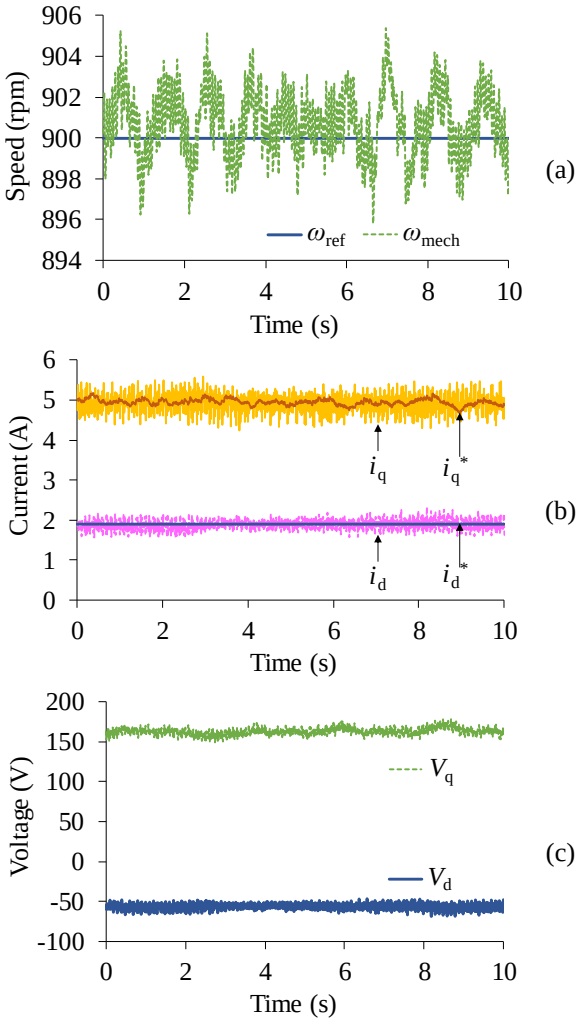

Figure 6-10: PMaSynRM-2 steady state variations of (a) speed, (b) i_d and i_q and, (c) V_d and V_q at the rated operation.

It is clear from the above graphs that the steady state performance of the fabricated PMaSynRM-2 is as expected and controllers are tuned to a satisfactory level. For example at rated operation when i_d^* is set to 1.9 A, the expected i_q^* is 5 A, which is also determined by the controller itself. On the other hand, the generated V_d and V_q signals are averaged around -60 V and 160 V, respectively to create phase peak of 170 V without any over modulation, hence the maximum utilization of the available DC link voltage of 340 V is achieved.

6.4 Experimental Analysis and Evaluation

Actual performances of fabricated SynRM and PMaSynRM-2 are considered maximum power output, efficiencies at maximum output powers and power factors at maximum output powers and compared with modified simulation predictions.

6.4.1 Maximum Output Power

MPF current angle and VCLMT control methods are used to control the SynRM and PMaSynRM-2 in the operating regions below base speed and FW region, respectively. FW is achieved by bringing down the i_d^* gradually towards zero when speed is beyond rated speed. The FE-based simulated and experimental output power capabilities of the designed machines are shown in Figure 6-11.

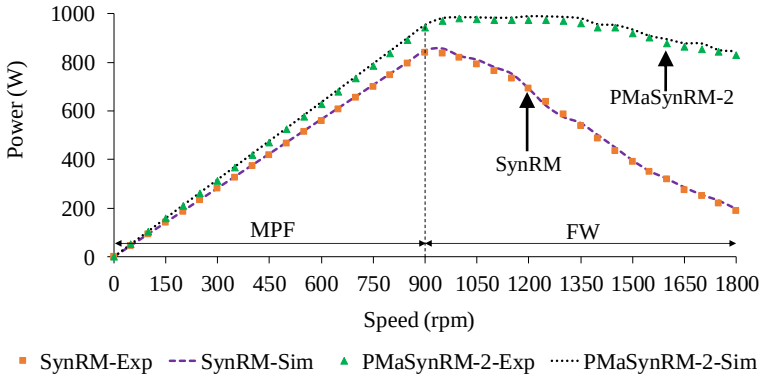

Figure 6-11: Output power capabilities for the designed SynRM and PMaSynRM-2

As seen, there is a close agreement between the simulated and actual output power of the analyzed machines in a wide speed range. Due to the manufacturing error and 0.25 mm larger air-gap for the built machines compared to what it was initially assumed, the output powers of the tested machines are 15% smaller than the designs' initial requirements which are justified through the analysis of section 6.1.1. In addition, the output power of PMaSynRM-2 is 942 W in base speed which is actually 12% larger than that of SynRM at a same speed. The peak power of PMaSynRM-2 may reach above 980 W at 1000 rpm, which is still at least 135 W larger than the peak power of SynRM. In FW region, the output power of PMaSynRM-2 is 600 W larger than SynRM at 1800 rpm verifying the significant contribution of adding PMs into SynRM's structure in beyond base speed operating regions.

6.4.2 Efficiencies at Maximum Output Powers

The efficiency of each tested machine is calculated using the measured input and output powers in a wide speed range. The FE-based simulated efficiencies are compared with the experimental results to verify the accuracy of the simulated models. The efficiency evaluations are shown in Figure 6-12. As seen, the efficiencies of the simulated SynRM and PMaSynRM-2 are well validated through the tests. At base speed, the efficiencies of 84% and 85.5% are recorded for SynRM and PMaSynRM-2, respectively, which are both close to the initial efficiency requirement of 85%. The maximum recorded efficiencies in the maximum possible developed torques during the tests are 84.5% and 86% for SynRM and PMaSynRM-2 occurring at 950 rpm, respectively. Meanwhile, an efficiency drop is not seen for the tested and corresponding simulated SynRM in FW region as the drawn current may actually reduce from 5.35 A to 4.3 A in this region causing the copper losses to diminish for this machine.

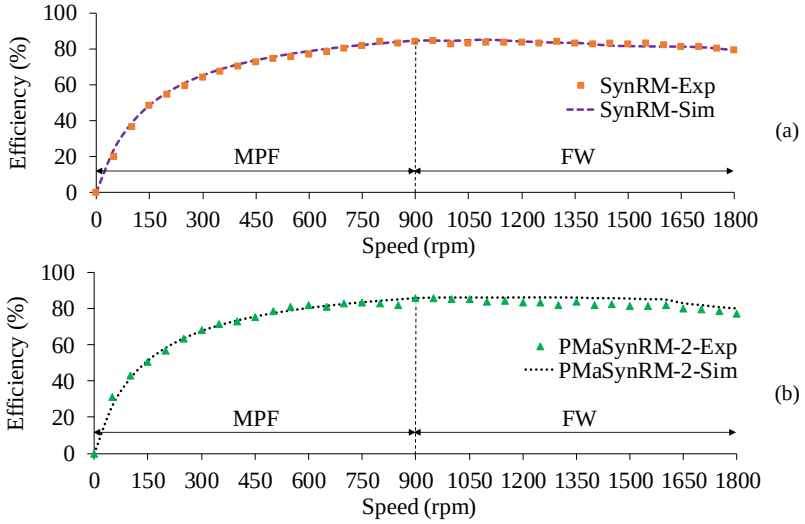

Figure 6-12: Efficiency evaluations for (a) SynRM and (b) PMaSynRM-2.

6.4.3 Power Factors at Maximum Output Powers

The power factor variations of the simulated and actual SynRM and PMaSynRM-2 in a wide speed range are shown in Figure 6-13.

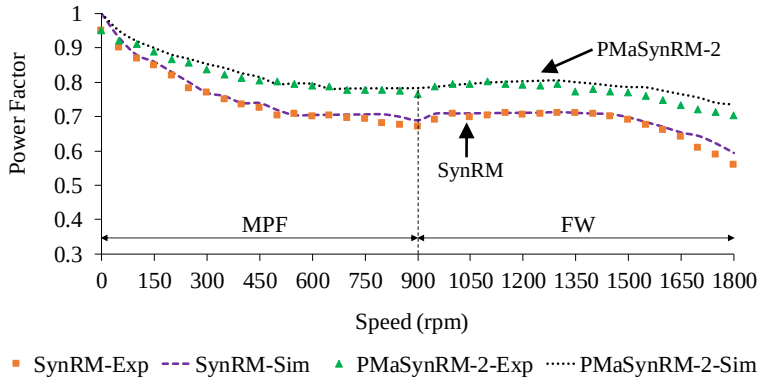

Figure 6-13: Power factor variations for designed SynRM and PMaSynRM-2.

As seen, a well agreement between simulations and experimental results are observed for the analyzed machines. The rated power factors of 0.67, 0.76 and maximum power factors of 0.71 at 1350 rpm and 0.8 at 1050 rpm are recorded for SynRM and PMaSynRM-2 respectively. The comparative study shows that adding PM may contribute up to 13% to the power factor of a SynRM in a wide speed range. The power factors of the analyzed machines are highly affected

by the core loss components in the d-q axis voltage-current vector diagrams; as such, a significantly larger power factor is supported in low speed operating points.

6.5 Summary

Experimental validation for the predicted performance of SynRM and PMaSynRM were considered with a detailed decoupled closed loop FOC. It has also been highlighted how manufacturing inaccuracies can affect the performance of each machine type especially the importance of preserving the air-gap length during fabrication is highlighted. Although the initially defined power capabilities of the SynRM and PMaSynRM were not fully satisfied due to the manufacturing error, 12%, 300%, 1.5%, and 13% improvement in the rated power, output power in FW region, efficiency, and power factor were validated for the tested PMaSynRM-2 versus SynRM, respectively. Experimental test results confirmed the accuracy of the simulation-based optimal design predictions.

Chapter 7

Contributions, Conclusions and Future Work

Important contributions of this, concluding remarks, and the suggested future work are presented in this final chapter.

7.1 Contributions and Conclusions

The main objective of this thesis was to develop a four flux barriers per pole, four-pole hyperbolic rotor structure for SynRMs in a FE-based environment for possible multi objective performance enhancements such as saliency ratio improvement, torque ripple minimization and power density improvement using GA optimization. A comprehensive implementation of the said rotor and specifically designed stator structure for each considered SynRM was used to perform simulation analysis. The best selected SynRM was fabricated and analyzed experimentally to show how manufacturing tolerances can affect the predicted performance and again validated through the updated simulation results. The following paragraphs portray the important findings of each chapter.

In Chapter 2, the basic operating principle of SynRM was discussed and a literature review was done to identify the advantages, challenges and possible improvements to both rotor and stator structures. As a result, distributed winding and four pole, four flux barrier rotor characteristics were recommended for the design efforts due to the potential higher developed torque capability with lower harmonic contents in the air-gap. To broaden the analysis, various SPPs and rotor structures were encouraged to find a better potential design with more promising

operating indicators. The importance of modeling the SynRM torque equation in rotor d-q reference frame was also given in details.

In Chapter 3, a comprehensive step-by-step guide to calculate the stator dimensions for a 36-slot, four-pole SynRM was presented and a systematic approach to design coordinate based four flux barriers per pole, four-pole hyperbolic rotor structure in a FE environment was presented with practical additions like incorporation of filleting of the flux barriers into the same design so that the simulation can be more analogous to a practical design. The optimized properties of the rotor structure were found for the RM-based, SM-based, and COF-based optimally designed SynRMs. It was shown that the torque ripple and saliency ratio of the SynRMs may significantly change, as a function of machine's operating points, for instance from 5% to above 100% and 1 to 10.86, respectively. Furthermore, the higher saliency ratio characteristic could result in a larger developed power, wider speed range, and higher power factor with the expense of a larger torque ripple. To make a compromise between the useful and unwanted operating characteristics, a COF-based optimized SynRM could be a reliable alternative.

In Chapter 4, design optimization and performance analysis for SynRMs with different SPPs categories were conducted. It was shown that a SynRM with SPP of 2 could support a larger output power, efficiency, and power factor in high speed regions, however lacking performance around and below base speed. Furthermore, SynRMs with SPPs of 3 and 4 are superior in terms of these performance indicators at low speeds including base speed. In general, cut off rotor designs showed the higher saliency ratio and larger harmonic content compared to the normal rotor structures. The 36-slot four-pole (SPP=3) SynRM was verified by simulations as the overall best performer.

In Chapter 5, addition of ferrite magnets along q-axis to the selected 36-slot, four-pole SynRM was analyzed and it was found that it can improve the average torque by 12.6%, power factor by 19.5%, and constant power wide speed range by 213% compared to its SynRM counterpart. It was also shown that optimization can greatly help to reduce the magnet weight while keeping the performance enhancements. For example the optimal PMaSynRM-2 rotor structure only utilizes one third of the available q-axis room yet offers similar or better performance compared to the full magnet model. It was also found that adding PM will not necessarily improve the saliency ratio. The mechanical aspects of the SynRM are improved after introducing the magnets along q-axis as the deformation and stress of the rotor laminations even got reduced by 94.25% and 84.74%, respectively.

Lastly in Chapter 6, the fabrication, experimental validation of the selected best SynRM and PMaSynRMs were reported and the effects of manufacturing inaccuracies towards the predicted performance were also tested and again supported by simulations. Since the original simulation model was modified accordingly to match with the fabricated machines for final validation, the accuracy and validity of the original model was also preserved. A detailed FOC for SynRM was presented and experimentally validated. It has also been highlighted the importance of preserving the air-gap length during fabrication in both simulation and experimental results. Although the fabricated machines couldn`t provide the defined power capabilities, PMaSynRM-2 showed the similar percentage improvement in developed torque over SynRM even with a 71.5% larger air-gap.

Overall, PMaSynRM-2 can be recommended as the all-round winner that has higher power capability, power factor profile, wide speed range, and a better stable operation. However special cases may need magnet free rotor structures, hence SynRM can also be an alternative to IMs.

7.2 Limitations and Future Work

The methodology to obtain the rotor structure dimensions using FE-based optimization is strictly for four flux barriers per pole, four-pole hyperbolic rotor structures only. This is mainly due to the derived mathematical equations were meant to be systematic. Hence prior to obtaining the coordinates, specific rotor structure had to be chosen. The high level steps can, however, be used as a guide to obtain coordinates for any other rotor type.

Throughout this thesis, detailed FE-based 2D model simulations were used as a balance between accuracy and time. Also the close agreement between simulation and experimental results justifies that 2D analysis is sufficient at least for the motor structure considered. However, for other modified structures and properly account for the stator end windings, especially with distributed winding arrangements, 3D modelling could be used, but would introduce additional challenges. Deriving a similar model with large degrees of freedom such as the one in this thesis in 3D is more difficult and requires significantly more computational time and memory resources.

Fabrication of the machine structure as designed can be hugely challenging due to highly complex rotor structure and small air-gap requirement. It is advised to use high accuracy tools to cut the laminations in future works, otherwise the performance may be affected depending on the measurements discrepancy between designed and built models. Ordering laser cut magnets slightly smaller than designated slots can be helpful when inserting.

The same rotor structure can be used to analyse asymmetric magnet arrangement in each pole for possible performance improvements by slightly modifying the given variables in this thesis and follow the same optimization procedure. It may then require proper rotor balancing if proceed with experimental testing.

7.3 Publications

Two research papers were presented in highly reputed IEEE conferences and one IEEE journal paper is under review at the time of writing this thesis.

1. I. P. Abeyrathne, M. S. Toulabi and S. Filizadeh, "A Comparative Study of Optimally Designed Synchronous Reluctance Machines," in *Proc., XXIII IEEE International Conference on Electrical Machines (ICEM)*, Alexandroupoli, 2018, pp. 467-473.
2. I. P. Abeyrathne, M. S. Toulabi and S. Filizadeh, "Design Optimization and Performance Prediction of Synchronous Reluctance Motors," in *Proc., 21st IEEE International Conference on Electrical Machines and Systems (ICEMS)*, Jeju, 2018, pp. 576-581.
    - **Won the Best Paper Award** in the "DC and AC Machines" category
3. I. P. Abeyrathne, M. S. Toulabi, S. Filizadeh and A. M. Gole "Design and Analysis of a Ferrite Magnet Assisted Synchronous Reluctance Machine," *IEEE Trans. Energy Convers*, submitted (TEC-00501-2019).

References

[1] A. Fatemi, D. M. Ionel, N. A. O. Demerdash, S. J. Stretz, and T. M. Jahns, “RSM-DE-ANN method for sensitivity analysis of active material cost in PM motors,” in *Proc., IEEE Energy Conversion Congress and Exposition (ECCE),* 2016, pp. 1–7.

[2] Blondel, *A.E.: Synchronous Motors and Converters: Theory and Methods of Calculation and Testing, translated by Mailloux*. C.O. McGraw Hill Book Co., New York, 1913.

[3] R. E. Doherty and C. A. Nickle, "Synchronous machines I-an extension of blondel's two-reaction theory," in *Transactions of the American Institute of Electrical Engineers*, vol. XLV, pp. 912-947, Jan. 1926.

[4] J. K. Kostko, "Polyphase reaction synchronous motors," in *Journal of the American Institute of Electrical Engineers,* vol. 42, no. 11, pp. 1162-1168, Nov. 1923.

[5] A. J. O. Cruickshank, R. W. Menzies, and A. F. Anderson, “Axially laminated anisotropic rotors for reluctance motors,” *Proc. Inst. Electr. Eng.*, vol. 113, no. 12, pp. 2058–2060, Dec. 1966.

[6] I. Boldea, *Reluctance Synchronous Machines and Drives*. Clarendon Press, 1996.

[7] T. Fukami, M. Momiyama, K. Shima, R. Hanaoka and S. Takata, "Steady-State Analysis of a Dual-Winding Reluctance Generator With a Multiple-Barrier Rotor," *IEEE Trans. Energy Convers.*, vol. 23, no. 2, pp. 492-498, June 2008.

[8] G. Bramerdorfer, A. Zăvoianu, S. Silber, E. Lughofer and W. Amrhein, "Possibilities for Speeding Up the FE-Based Optimization of Electrical Machines—A Case Study," *IEEE Trans. Ind. Appl.*, vol. 52, no. 6, pp. 4668-4677, Nov.-Dec. 2016.

[9] C. Babetto, G. Bacco and N. Bianchi, "Synchronous Reluctance Machine Optimization for High-Speed Applications," *IEEE Trans. Energy Convers.*, vol. 33, no. 3, pp. 1266-1273, Sept. 2018.

[10] A. Kersten, Y. Liu, D. Pehrman and T. Thiringer, "Rotor Design of Line-Start Synchronous Reluctance Machine with Round Bars," *IEEE Trans. Ind. Appl.*, Early Access., 2019.

[11] I. P. Abeyrathne, M. S. Toulabi and S. Filizadeh, "A Comparative Study of Optimally Designed Synchronous Reluctance Machines," in *Proc., XXIII IEEE International Conference on Electrical Machines (ICEM)*, Alexandroupoli, 2018, pp. 467-473.

[12] I. P. Abeyrathne, M. S. Toulabi and S. Filizadeh, "Design Optimization and Performance Prediction of Synchronous Reluctance Motors," *in Proc., 21st IEEE International Conference on Electrical Machines and Systems (ICEMS)*, Jeju, 2018, pp. 576-581.

[13] K. Wang, Z. Q. Zhu, G. Ombach, M. Koch, S. Zhang and J. Xu, "Optimal slot/pole and flux-barrier layer number combinations for synchronous reluctance machines," in *Proc., 8th IEEE International Conference and Exhibition on Ecological Vehicles and Renewable Energies (EVER)*, Monte Carlo, 2013, pp. 1-8.

[14] X. Ma, G. Li, Z. Zhu, G. W. Jewell and J. Green, "Investigation on synchronous reluctance machines with different rotor topologies and winding configurations," in *IET Electric Power Applications*, vol. 12, no. 1, pp. 45-53, 1 2018.

[15] B. Lehner and D. Gerling, "Design and comparison of concentrated and distributed winding synchronous reluctance machines," *in Proc., IEEE Energy Conversion Congress and Exposition (ECCE)*, Milwaukee, WI, 2016, pp. 1-8.

[16] J. H. Lee, B. D. Lee and T. W. Yun, "A novel stator design of synchronous reluctance motor by loss & torque evaluations related to slot numbers using coupled Preisach model & FEM," in *Proc., IEEE International Conference on Electrical Machines and Systems*, Incheon, 2010, pp. 1438-1442.

[17] T. Mohanarajah, M. Nagrial, A. Hellany and J. Rizk, "Effect of saturation on performance of synchronous reluctance machines," in *Proc., IEEE International Conference on Power and Energy (PECon)*, Melaka, 2016, pp. 802-807.

[18] A. Vagati, A. Fratta, G. Franceschini and P. Rosso, "AC motors for high-performance drives: a design-based comparison," *IEEE Trans. Ind. Appl.*, vol. 32, no. 5, pp. 1211-1219, Sept.-Oct. 1996.

[19] A. Vagati, A. Canova, M. Chiampi, M. Pastorelli and M. Repetto, "Design refinement of synchronous reluctance motors through finite-element analysis," *IEEE Trans. Ind. Appl.*, vol. 36, no. 4, pp. 1094-1102, July-Aug. 2000.

[20] C. Hong, H. Liu, H. Seol, H. Jun and J. Lee, "Decrease torque ripple for SynRM using barrier arrangement design," in *Proc., 17th International Conference on Electrical Machines and Systems (ICEMS)*, Hangzhou, 2014, pp. 1834-1837.

[21] R. Moghaddam and F. Gyllensten, "Novel High-Performance SynRM Design Method: An Easy Approach for A Complicated Rotor Topology," in *IEEE Trans. Ind. Electron.*, vol. 61, no. 9, pp. 5058-5065, Sept. 2014.

[22] N. Bianchi, S. Bolognani, D. Bon and M. Dai Pre, "Rotor Flux-Barrier Design for Torque Ripple Reduction in Synchronous Reluctance and PM-Assisted Synchronous Reluctance Motors," in *IEEE Trans. Ind. Appl.*, vol. 45, no. 3, pp. 921-928, May-june 2009.

[23] M. D. Nardo, G. L. Calzo, M. Galea and C. Gerada, "Design Optimization of a High-Speed Synchronous Reluctance Machine," in *IEEE Trans. Ind. Appl.,* vol. 54, no. 1, pp. 233-243, Jan.-Feb. 2018.

[24] Y. Wang, D. M. Ionel, V. Rallabandi, M. Jiang and S. J. Stretz, "Large-Scale Optimization of Synchronous Reluctance Machines Using CE-FEA and Differential Evolution," in *IEEE Trans. Ind. Appl.,* vol. 52, no. 6, pp. 4699-4709, Nov.-Dec. 2016.

[25] M. Muteba, B. Twala and D. V. Nicolae, "Torque ripple minimization in synchronous reluctance motor using a sinusoidal rotor lamination shape," in *Proc., XXII IEEE International Conference on Electrical Machines (ICEM)*, Lausanne, 2016, pp. 606-611.

[26] N. Bianchi, S. Bolognani, D. Bon and M. Dai PrÉ, "Torque Harmonic Compensation in a Synchronous Reluctance Motor," in *IEEE Trans. Energy Convers.,* vol. 23, no. 2, pp. 466-473, June 2008.

[27] A. Vagati, M. Pastorelli, G. Francheschini and S. C. Petrache, "Design of low-torque-ripple synchronous reluctance motors," in *IEEE Trans. Ind. Appl.,* vol. 34, no. 4, pp. 758-765, July-Aug. 1998.

[28] I. Petrov, M. Niemelä, P. Ponomarev and J. Pyrhönen, "Rotor Surface Ferrite Permanent Magnets in Electrical Machines: Advantages and Limitations," in *IEEE Trans. Ind. Electron.,* vol. 64, no. 7, pp. 5314-5322, July 2017.

[29] C. Desai, H. R. Mehta and P. Pillay, "Fabrication and Assembly Method for Synchronous Reluctance Machines," in *IEEE Trans. Ind. Appl.,* vol. 54, no. 5, pp. 4227-4235, Sept.-Oct. 2018.

[30] S. M. Taghavi and P. Pillay, "A Mechanically Robust Rotor With Transverse Laminations for a Wide-Speed-Range Synchronous Reluctance Traction Motor," in *IEEE Trans. Ind. Appl.*, vol. 51, no. 6, pp. 4404-4414, Nov.-Dec. 2015.

[31] H. Murakami, Y. Honda, H. Kiriyama, S. Morimoto and Y. Takeda, "The performance comparison of SPMSM, IPMSM and SynRM in use as air-conditioning compressor," in *Proc., 34th IEEE Annual conference on Industry Applications*, 1999, pp. 840-845 vol.2.

[32] A. Rassolkin, H. Heidari, A. Kallaste, T. Vaimann, J. P. Acedo and E. Romero-Cadaval, "Efficiency Map Comparison of Induction and Synchronous Reluctance Motors," in *Proc., 26th IEEE International Workshop on Electric Drives: Improvement in Efficiency of Electric Drives (IWED)*, 2019, pp. 1-4.

[33] I. Boldea, "Electric generators and motors: An overview," in *CES Transactions on Electrical Machines and Systems*, vol. 1, no. 1, pp. 3-14, March 2017.

[34] A. J. Piña and L. Xu, "Comparison of apparent power consumption in Synchronous Reluctance and Induction Motor under vector control," in *Proc., IEEE Transportation Electrification Conference and Expo (ITEC)*, Dearborn, MI, 2015, pp. 1-6.

[35] A. T. de Almeida, F. J. T. E. Ferreira and G. Baoming, "Beyond Induction Motors—Technology Trends to Move Up Efficiency," in *IEEE Trans. Ind. Appl.*, vol. 50, no. 3, pp. 2103-2114, May-June 2014.

[36] D. Jung, Y. Kwak, J. Lee and C. Jin, "Study on the Optimal Design of PMa-SynRM Loading Ratio for Achievement of Ultrapremium Efficiency," in *IEEE Trans. Magn.*, vol. 53, no. 6, pp. 1-4, June 2017, Art no. 8001904.

[37] H. Kärkkäinen, L. Aarniovuori, M. Niemelä, J. Pyrhönen and J. Kolehmainen, "Technology comparison of induction motor and synchronous reluctance motor," in *Proc*.,

43rd IEEE Annual Conference on Industrial Electronics (IECON), Oct. 2017, pp. 2207–2212

[38] Y. Da, X. Shi and M. Krishnamurthy, "A New Approach to Fault Diagnostics for Permanent Magnet Synchronous Machines Using Electromagnetic Signature Analysis," in *IEEE Trans. Power Electron.*, vol. 28, no. 8, pp. 4104-4112, Aug. 2013.

[39] T. Hamiti, T. Lubin and A. Rezzoug, "A Simple and Efficient Tool for Design Analysis of Synchronous Reluctance Motor," in *IEEE Trans. Magn.*, vol. 44, no. 12, pp. 4648-4652, Dec. 2008.

[40] C. M. Stephens, "Fault detection and management system for fault-tolerant switched reluctance motor drives," in *IEEE Trans. Ind. Appl.*, vol. 27, no. 6, pp. 1098-1102, Nov.-Dec. 1991.

[41] Dinyu Qin, Xiaogang Luo and T. A. Lipo, "Reluctance motor control for fault-tolerant capability," in *Proc., IEEE International Electric Machines and Drives Conference Record*, Milwaukee, WI, USA, 1997, pp. WA1/1.1-WA1/1.6.

[42] R. Caro, C. A. Silva, R. Pérez and J. I. Yuz, "Sensorless control of a SynRM for the whole speed range based on a nonlinear observability analysis," in *Proc., IEEE International Conference on Industrial Technology (ICIT)*, Toronto, ON, 2017, pp. 336-341.

[43] C. Li, G. Wang, G. Zhang, D. Xu and D. Xiao, "Saliency-Based Sensorless Control for SynRM Drives With Suppression of Position Estimation Error," in *IEEE Trans. Ind. Electron.*, vol. 66, no. 8, pp. 5839-5849, Aug. 2019.

[44] H. Mahmoud, G. Bacco, M. Degano, N. Bianchi and C. Gerada, "Synchronous Reluctance Motor Iron Losses: Considering Machine Nonlinearity at MTPA, FW, and MTPV

Operating Conditions," in *IEEE Trans. Energy Convers.*, vol. 33, no. 3, pp. 1402-1410, Sept. 2018.

[45] Y. Lu *et al*., "Electromagnetic Force and Vibration Analysis of Permanent-Magnet-Assisted Synchronous Reluctance Machines," in *IEEE Trans. Ind. Appl.*, vol. 54, no. 5, pp. 4246-4256, Sept.-Oct. 2018.

[46] J. Nakatsugawa, Y. Kawabata, T. Endoh, M. Kitamura and J. Kaneda, "A fundamental investigation about maximum torque control of synchronous reluctance motor," in *Proc., IEEE Conference on Power Conversion* , 2002, pp. 704-709 vol.2.

[47] Y. Wang, G. Bacco and N. Bianchi, "Geometry Analysis and Optimization of PM-Assisted Reluctance Motors," in *IEEE Trans. Ind. Appl.*, vol. 53, no. 5, pp. 4338-4347, Sept.-Oct. 2017.

[48] M. Ferrari, N. Bianchi and E. Fornasiero, "Analysis of Rotor Saturation in Synchronous Reluctance and PM-Assisted Reluctance Motors," in *IEEE Trans. Ind. Appl.*, vol. 51, no. 1, pp. 169-177, Jan.-Feb. 2015.

[49] S. Ooi, S. Morimoto, M. Sanada and Y. Inoue, "Performance Evaluation of a High-Power-Density PMASynRM With Ferrite Magnets," in *IEEE Trans. Ind. Appl.*, vol. 49, no. 3, pp. 1308-1315, May-June 2013.

[50] C. Liu *et al*., "On the Design and Construction Assessments of a Permanent-Magnet-Assisted Synchronous Reluctance Motor," in *IEEE Trans. Magn.*, vol. 53, no. 11, pp. 1-4, Nov. 2017, Art no. 2002104.

[51] S. Morimoto, M. Sanada and Y. Takeda, "Performance of PM-assisted synchronous reluctance motor for high-efficiency and wide constant-power operation," in *IEEE Trans. Ind. Appl.*, vol. 37, no. 5, pp. 1234-1240, Sept.-Oct. 2001.

[52] P. Guglielmi, B. Boazzo, E. Armando, G. Pellegrino and A. Vagati, "Permanent-Magnet Minimization in PM-Assisted Synchronous Reluctance Motors for Wide Speed Range," in *IEEE Trans. Ind. Appl.,* vol. 49, no. 1, pp. 31-41, Jan.-Feb. 2013.

[53] P. Niazi, H. A. Toliyat, D. Cheong and J. Kim, "A Low-Cost and Efficient Permanent-Magnet-Assisted Synchronous Reluctance Motor Drive," in *IEEE Trans. Ind. Appl.,* vol. 43, no. 2, pp. 542-550, March-april 2007.

[54] M. N. Ibrahim, P. Sergeant and E. M. Rashad, "Rotor design with and without permanent magnets and performance evaluation of synchronous reluctance motors," in *Proc., 19th IEEE International Conference on Electrical Machines and Systems (ICEMS),* Chiba, 2016, pp. 1-7.

[55] H. Cai, B. Guan and L. Xu, "Low-Cost Ferrite PM-Assisted Synchronous Reluctance Machine for Electric Vehicles," in *IEEE Trans. Ind. Electron.,* vol. 61, no. 10, pp. 5741-5748, Oct. 2014.

[56] B. Wang, J. Wang, B. Sen, A. Griffo, Z. Sun and E. Chong, "A Fault-Tolerant Machine Drive Based on Permanent Magnet-Assisted Synchronous Reluctance Machine," in *IEEE Trans. Ind. Appl.*, vol. 54, no. 2, pp. 1349-1359, March-April 2018.

[57] W. Kim *et al*., "Optimal PM Design of PMA-SynRM for Wide Constant-Power Operation and Torque Ripple Reduction," in *IEEE Trans. Magn.*, vol. 45, no. 10, pp. 4660-4663, Oct. 2009.

[58] B. Wang, J. Wang, A. Griffo and Y. Shi, "Investigation Into Fault-Tolerant Capability of a Triple Redundant PMA SynRM Drive," in *IEEE Trans. Power Electron.,* vol. 34, no. 2, pp. 1611-1621, Feb. 2019.

[59] D. Ngo, M. Hsieh and T. A. Huynh, "Torque Enhancement for a Novel Flux Intensifying PMa-SynRM Using Surface-Inset Permanent Magnet," in *IEEE Trans. Magn.*, pp. 1–8, 2019.

[60] R. Lohninger, H. Grabner, G. Weidenholzer, S. Silber and W. Amrhein, "Modeling, Simulation, and Design of a Permanent-Magnet-Assisted Synchronous Reluctance Machine," in *IEEE Trans. Ind. Appl.*, vol. 51, no. 1, pp. 196-203, Jan.-Feb. 2015.

[61] P. Niazi, H. A. Toliyat and A. Goodarzi, "Robust Maximum Torque per Ampere (MTPA) Control of PM-Assisted SynRM for Traction Applications," in *IEEE Trans. Veh. Technol.*, vol. 56, no. 4, pp. 1538-1545, July 2007.

[62] T. A. Huynh, M. Hsieh, K. Shih and H. Kuo, "An Investigation Into the Effect of PM Arrangements on PMa-SynRM Performance," in *IEEE Trans. Ind. Appl.*, vol. 54, no. 6, pp. 5856-5868, Nov.-Dec. 2018.

[63] N. Bianchi, E. Fornasiero and W. Soong, "Selection of PM Flux Linkage for Maximum Low-Speed Torque Rating in a PM-Assisted Synchronous Reluctance Machine," in *IEEE Trans. Ind. Appl.*, vol. 51, no. 5, pp. 3600-3608, Sept.-Oct. 2015.

[64] M. Barcaro and N. Bianchi, "Interior PM machines using Ferrite to substitute rare-earth surface PM machines," in *Proc., XXth IEEE International Conference on Electrical Machines (ICEM)*, Marseille, 2012, pp. 1339-1345.

[65] N. Bianchi, S. Bolognani, E. Carraro, M. Castiello and E. Fornasiero, "Electric Vehicle Traction Based on Synchronous Reluctance Motors," in *IEEE Trans. Ind. Appl.*, vol. 52, no. 6, pp. 4762-4769, Nov.-Dec. 2016.

[66] I. Petrov and J. Pyrhonen, "Performance of Low-Cost Permanent Magnet Material in PM Synchronous Machines," in *IEEE Trans. Ind. Electron.*, vol. 60, no. 6, pp. 2131-2138, June 2013.

[67] T. A. Huynh and M. Hsieh, "Comparative Study of PM-Assisted SynRM and IPMSM on Constant Power Speed Range for EV Applications," in *IEEE Trans. Magn.*, vol. 53, no. 11, pp. 1-6, Nov. 2017, Art no. 8211006.

[68] A. Tap, L. Xheladini, M. Yilmaz, M. Imeryuz, T. Asan and L. T. Ergene, "Comprehensive design and analysis of a PMaSynRM for washing machine applications," in *IET Electric Power Applications*, vol. 12, no. 9, pp. 1311-1319, 11 2018.

[69] R. Leuzzi, P. Cagnetta, F. Cupertino, S. Ferrari and G. Pellegrino, "Performance assessment of ferrite- and neodymiumassisted synchronous reluctance machines," in *Proc., IEEE Energy Conversion Congress and Exposition (ECCE)*, Cincinnati, OH, 2017, pp. 3958-3965.

[70] Y. Wang, D. M. Ionel, M. Jiang and S. J. Stretz, "Establishing the Relative Merits of Synchronous Reluctance and PM-Assisted Technology Through Systematic Design Optimization," in *IEEE Trans. Ind. Appl.*, vol. 52, no. 4, pp. 2971-2978, July-Aug. 2016.

[71] T. A. Huynh, M. Hsieh, K. Shih and H. Kuo, "Design and analysis of permanent-magnet assisted synchronous reluctance motor," in *Proc., 20th IEEE International Conference on Electrical Machines and Systems (ICEMS)*, Sydney, NSW, 2017, pp. 1-6.

[72] K. Hasse, “Drehzahlgelverfahren fur schnelle Umkehrantriebe mit strom-richtergespeisten Asynchron-Kurzchlusslaufermotoren,” *Reglungstechnik*, vol. 20, no. 2, pp. 60–66, 1972.

[73] F. Blaschke, “The principle of field-orientation as applied to the transvector closedloop control system for rotating-field machines,” *Siemens Rev.*, vol. 31, no. 1, pp. 217–220, 1972.

[74] M. P. Kazmierkowski, R. Krishnan, and F. Blaabjerg, *Control in Power Electronics. New York: Academic*. 2002.

[75] R. Krishnan, *Electric Motor Drives*. Englewood Cliffs, NJ: Prentice-Hall, 2001.

Appendix A

Given below are the fabricated stator and rotor lamination drawings of optimally designed SynRM and PMaSynRM-2.

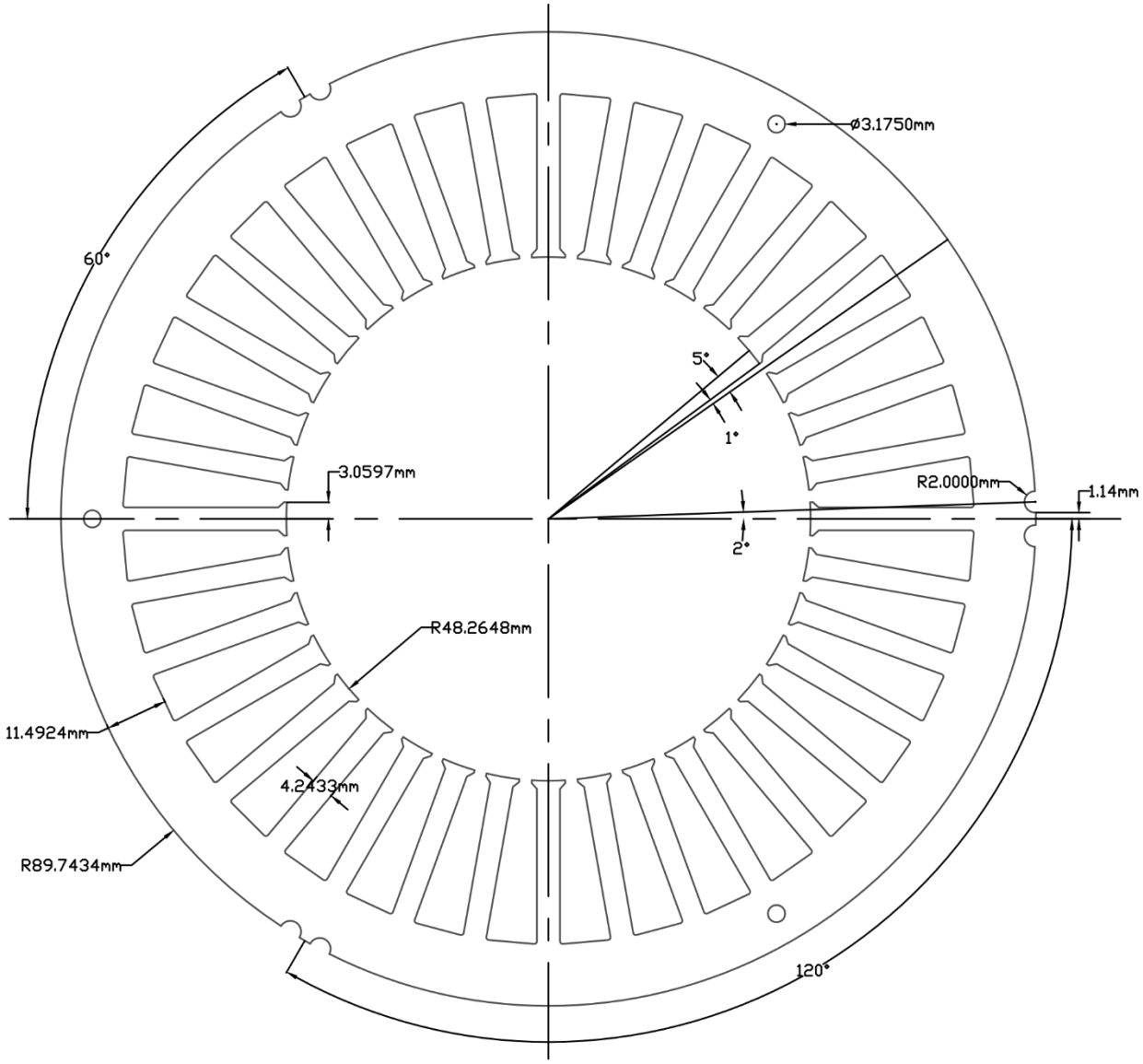

Stator Lamination with important marked dimensions for fabrication

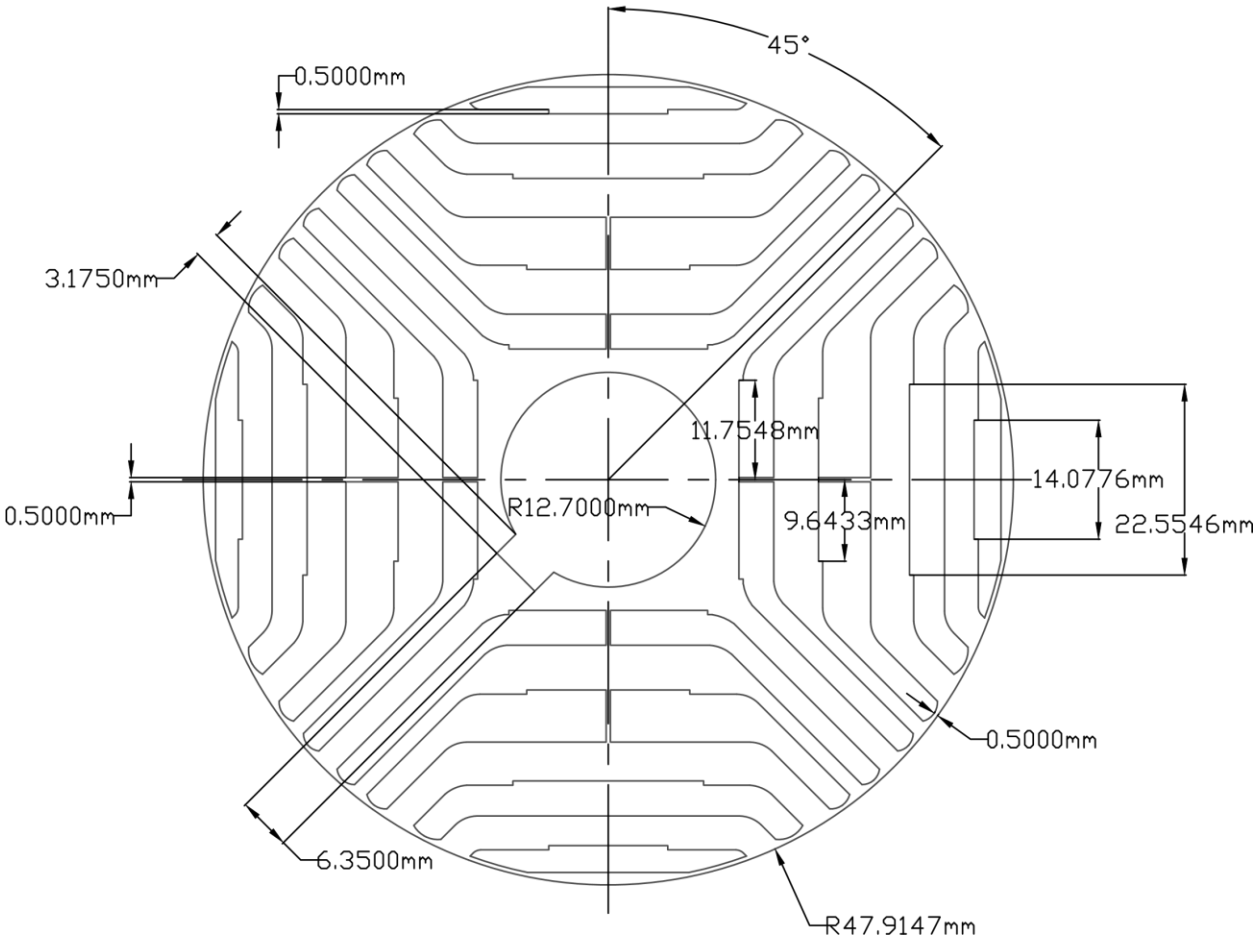

Rotor lamination with important marked dimensions for fabrication